Published by IOP Publishing for Sissa Medialab

Received: *October 22, 2024*
Accepted: *November 3, 2024*
Published: *November 22, 2024*

Performance of the CMS high-level trigger during LHC Run 2

The CMS collaboration

E-mail: cms-publication-committee-chair@cern.ch

Abstract: The CERN LHC provided proton and heavy ion collisions during its Run 2 operation period from 2015 to 2018. Proton-proton collisions reached a peak instantaneous luminosity of $2.1 \times 10^{34}\,\mathrm{cm}^{-2}\mathrm{s}^{-1}$, twice the initial design value, at $\sqrt{s} = 13\,\mathrm{TeV}$. The CMS experiment records a subset of the collisions for further processing as part of its online selection of data for physics analyses, using a two-level trigger system: the Level-1 trigger, implemented in custom-designed electronics, and the high-level trigger, a streamlined version of the offline reconstruction software running on a large computer farm. This paper presents the performance of the CMS high-level trigger system during LHC Run 2 for physics objects, such as leptons, jets, and missing transverse momentum, which meet the broad needs of the CMS physics program and the challenge of the evolving LHC and detector conditions. Sophisticated algorithms that were originally used in offline reconstruction were deployed online. Highlights include a machine-learning b tagging algorithm and a reconstruction algorithm for tau leptons that decay hadronically.

Keywords: Large detector systems for particle and astroparticle physics; Trigger concepts and systems (hardware and software)

https://doi.org/10.1088/1748-0221/19/11/P11021

2024 JINST 19 P11021

Contents

1 Introduction

The CERN LHC collides bunches of particles at a maximum rate of about 40 MHz at several experimental sites including CMS. During LHC Run 2 in 2015–2018, the maximum instantaneous luminosity $\mathcal{L}_{\text{inst}}$ reached $2.1 \times 10^{34}\,\text{cm}^{-2}\text{s}^{-1}$, twice the initial design value, at $\sqrt{s} = 13$ TeV. The mean pileup (PU), or simultaneous inelastic proton-proton (pp) collisions per bunch crossing, was about 50. To select collision events of potential interest to physics analyses, the CMS trigger system divides the processing into two levels: a first level (L1) that is implemented in custom-designed electronics, and a high-level trigger (HLT) implemented in software and executed on commodity computers. The HLT further refines the purity of the collection of physics objects that are selected at L1, with an input event rate to the HLT limited to about 100 kHz by the detector read-out electronics, and targets an average output rate of about 1 kHz during Run 2 for standard pp collision events for offline storage and prompt reconstruction. The HLT also accommodates combinations of objects, such as leptons and jets or final states in B physics, to target specific physics analyses, although the focus of this paper is on the reconstruction and object identification tools used at the HLT. Novel techniques introduced

2024 JINST 19 P11021

during Run 1, such as a high rate storage of events with a reduced data content ("data scouting") and storage of additional full events for delayed processing ("data parking"), both described in ref. [1], continued during Run 2 to further extend the physics program.

The performance of the CMS L1 and HLT trigger systems during Run 1 of the LHC, with $\sqrt{s} = 7$ and 8 TeV for pp collisions, is described in ref. [2]. The L1 trigger was subsequently upgraded during Run 2 of the LHC as part of the Phase-1 upgrades of CMS [3], and its performance is described in ref. [4]. Run 2 of the LHC delivered challenges to the Run 1 L1 and HLT algorithms, including a higher $\sqrt{s}$ of 13 TeV, higher luminosity, larger PU, and further detector aging (primarily from radiation damage). The algorithms deployed at the HLT were revised to address these challenges and were made flexible enough to adapt to various changing detector conditions that occurred during Run 2, together with the installation of detector components and electronics that were part of the CMS Phase-1 upgrades [5]. Further adaptations of the HLT for Run 3 of the LHC, such as the inclusion of graphical processing units for computation, are described in ref. [6].

This paper is organized as follows. Section 2 describes the CMS experiment and the LHC operating conditions during Run 2, and section 3 describes the architecture of the HLT, as well as a breakdown of its rate and processing time. Section 4 describes the reconstruction and performance of the physics objects in the HLT that are broadly applicable to a wide range of physics analyses, such as lepton, jet, and energy sum triggers. Finally, a summary is given in section 5.

2 Experimental conditions during Run 2

2.1 The CMS detector

The central feature of the CMS apparatus is a superconducting solenoid of 6 m internal diameter, providing a magnetic field of 3.8 T. Within the solenoid volume are a silicon pixel and strip tracker, a lead tungstate crystal electromagnetic calorimeter (ECAL), and a brass and scintillator hadron calorimeter (HCAL), each composed of a barrel and two endcap sections. Forward calorimeters extend the pseudorapidity coverage provided by the barrel and endcap detectors. Muons are detected in gas-ionization chambers embedded in the steel flux-return yoke outside the solenoid. A more detailed description of the CMS detector, together with a definition of the coordinate system used and the relevant kinematic variables, can be found in refs. [6, 7]. The silicon tracker used in 2016 measured charged particles within the range $|\eta| < 2.5$. For nonisolated particles with $1 < p_{\mathrm{T}} < 10$ GeV and $|\eta| < 1.4$, the track resolutions were typically 1.5% in p_{T} and 25–90 (45–150) μm in the transverse (longitudinal) impact parameter d_{xy} (d_z) [8]. At the start of 2017, a new pixel detector was installed [9]; the upgraded tracker measured particles up to $|\eta| = 3.0$ with typical resolutions of 1.5% in p_{T} and 20–75 μm in d_{xy} [10] for nonisolated particles of $1 < p_{\mathrm{T}} < 10$ GeV. According to simulation studies [11], similar improvements are expected in the longitudinal direction.

2.2 The LHC operations

The operational period of LHC Run 2 covered the years 2015 to 2018. The year 2015 was dominated by commissioning activities in the wake of LHC Long Shutdown 1, with a correspondingly small amount of integrated luminosity delivered to the experiments. Additionally, the electronics for the CMS L1 trigger was upgraded and installed for data taking at the beginning of 2016. Hence we will focus mainly on the 2016–2018 period.

2024 JINST 19 P11021

Traditionally, each year starts with an interleaved commissioning-production period, where the $\mathcal{L}_{\text{inst}}$ is progressively increased by the insertion of additional proton bunches in opposite directions to make two oppositely running proton beams in a single LHC fill. After the beams achieve their maximum occupancy projected for the year, the LHC conditions are optimized throughout the year to achieve the needs of the physics programs of the experiments. Within a given LHC fill, the $\mathcal{L}_{\text{inst}}$ generally decreases in tandem with the natural depletion of the beams, which allows for the activation of looser trigger algorithms that can increase the physics reach of an experiment by keeping the data bandwidth to storage effectively constant. For some Run 2 fills, the beam focusing was periodically adjusted to achieve approximately constant $\mathcal{L}_{\text{inst}}$ for an extended amount of time (luminosity leveling).

Table 1. The LHC operations parameters during Run 2. The maximum PU is for standard physics fills with more than 600 bunches, and the average PU is calculated assuming an inelastic cross section of 80 mb. The 8b4e bunch-filling configuration values are given in brackets, and they refer to an LHC configuration used in 2017 to mitigate beam losses. The $\sqrt{s_{\text{NN}}}$ is the center-of-mass energy per nucleon.

	2016	2017	2018
Proton-proton			
Max. colliding bunches	2220	2556 [1868]	2556
in CMS	2208	2544 [1866]	2544
Max. $\mathcal{L}_{\text{inst}}$ ($\times 10^{34}\,\text{cm}^{-2}\,\text{s}^{-1}$)	1.5	1.7 [2.1]	2.1
Max. PU	46.9	47.5 [78.8]	64.7
Avg. PU	27	31 [42]	37
Heavy ions			
Collisions species	pPb	XeXe, pp	PbPb
$\sqrt{s_{\text{NN}}}$(TeV)	8.16	5.44, 5.02	5.02

There are also special LHC runs that occur throughout the running period with a variety of purposes. Low-PU runs, with much less than 0.3 pp interactions per bunch crossing, are important for particular standard model (SM) measurements, such as the measurement of the W boson mass. On the other hand, high-PU runs, with fewer filled bunches, are also available for experimental performance measurements to prepare for the steady luminosity increase during Run 2, as well as for that expected for LHC Run 3 and for the High-Luminosity LHC era. Other special run setups include: reference pp collisions for the heavy ion program; luminosity studies during van der Meer scans [12], both at the initial proton injection energy and at the maximum energy; as well as special machine development runs for LHC beam studies.

The experience acquired through Run 2 led to progressively smoother LHC operations throughout the years [13, 14]. In 2016, the maximum $\mathcal{L}_{\text{inst}}$ had a rapid initial increase to the nominal value of $1.0 \times 10^{34}\,\text{cm}^{-2}\,\text{s}^{-1}$, followed by a gradual increase during the year to $\approx 1.5 \times 10^{34}\,\text{cm}^{-2}\,\text{s}^{-1}$. In 2017, this pre-shutdown performance was easily achieved by the start of the run, and adjustments made throughout the year allowed the crossing of the $2.0 \times 10^{34}\,\text{cm}^{-2}\,\text{s}^{-1}$ milestone by October. Amongst these adjustments, we highlight the deployment of the "8b4e" filling scheme (8 filled bunches followed by 4 empty buckets) accompanied by the reduction of β^* (a parameter related to

2024 JINST 19 P11021

the transverse beam size at the interaction point) from 40 to 30 cm to mitigate beam losses around the region of an LHC magnet interconnect [14, 15]. Finally, in 2018 the initial ramp-up period to routinely deliver maximum instantaneous luminosity was very quick, and collision data were acquired at a steady pace during the year. A summary of the LHC parameters for pp and heavy ion collisions for 2016–2018 is shown in table 1.

3 Online data selection

3.1 The HLT architecture

The HLT hardware consists of a large cluster of multi-core servers, the event filter farm, that runs a Linux operating system. The processing capacity of the Filter Farm was expanded gradually throughout Run 2 to cope with the evolving LHC and detector conditions. By the end of Run 2, the processing power was about 7.2×10^5 in HEPSPEC 2006 [16] units. This was distributed across 360 nodes of dual Intel Haswell E5-2680v3 processors (8640 cores), 324 nodes of dual Intel Broadwell E5-2680v4 processors (9072 cores), and 400 nodes of dual Intel Skylake Gold 6130 processors (12 800 cores).

As noted earlier, the HLT refines the purity and reduces the rate of events that are selected by L1, targeting a rate of about 1 kHz averaged over an LHC fill for standard pp collision events for offline storage and prompt reconstruction. Additional storage beyond the 1 kHz rate is allowed for data to be "parked", whereby the offline reconstruction is postponed until a later, non-data-taking period (e.g., during a long shutdown of the LHC). In 2018, the storage rate for parking was an additional 3 kHz [1]. The average raw data event size for these standard pp collision events at the average Run 2 PU (37) is about 0.65 MB after compression, with a peak size near 1 MB at the highest PU conditions. A higher rate of reduced-size events also can be acquired, a technique referred to as "data scouting," where only the high-level physics objects, such as jets or leptons, reconstructed at the HLT are stored on disk. No raw data from detector channels are stored for later offline analysis. For example, 5 kHz of scouting events with an average event size of 8 kB were also recorded in 2018 [1].

3.2 Algorithms

The data processing of the HLT is structured around the concept of an HLT "path", which is a set of algorithmic processing steps run in a predefined order that both reconstructs physics objects and makes selections on these objects based on the physics requirements. Each HLT path is implemented as a sequence of steps generally of increasing complexity, reconstruction refinement, and physics sophistication. For example, the processing of intensive track reconstruction is usually performed only after some initial reconstruction and selection based on the calorimeters and muon detectors. Each path also requires the selections in specific L1 triggers ("L1 seeds") to have been satisfied before execution would begin. The reconstruction modules and selection filters of the HLT use the same software framework used for offline reconstruction and analyses (CMSSW [17]). The framework supports multi-threaded event processing, which optimizes memory usage and is utilized for the HLT software.

The HLT paths selecting similar physics object topologies are grouped into primary data sets, which are then grouped into streams. Primary data sets define the samples used for offline processing, and their trigger content is chosen such that the overlap is minimized to avoid reconstructing offline the same event in multiple primary data sets. Streams define the outputs of the HLT processes, which are transferred from CMS to offline computing facilities during data taking. The grouping

2024 JINST 19 P11021

of primary data sets into streams further reduces the overlap across HLT outputs, allowing for a more efficient handling of these data transfers.

3.3 Menus

The HLT selects data for storage through the application of a trigger "menu", which is a collection of individual HLT paths. The trigger path definitions, physics object thresholds (e.g., the transverse energy E_T threshold and the p_T threshold), and rate allocations are set to meet the physics objectives of the experiment. For Run 2, the HLT menus typically had around 600 paths for pp data taking. This included the primary triggers for analyses, as well as triggers for calibration, efficiency measurements, control region measurements, etc. that were typically looser than the primary triggers. These latter triggers were often "prescaled", meaning that they selected only a fraction of the events that satisfied their conditions to limit their storage rate. Approximately a dozen menus were deployed each year during 2016–2018 for operations with pp collisions. Different sets of trigger menus were used for special LHC runs, including heavy ion collision runs. A representative listing of the primary triggers used in 2018 for physics analyses, along with their thresholds and corresponding rates, is given in table 2. These triggers accounted for approximately 50% of the overall menu rate used to select data that were reconstructed promptly. Note that the listed rates of each trigger are inclusive and not necessarily unique. For example objects selected by a trigger applying isolation would also be selected by a trigger not requiring isolation on the same type of objects, provided that the other conditions (e.g., energy) are met. Comprehensive details of the algorithms used and their performances are discussed in section 4.

The rest of the trigger menu not included in table 2 consists of slightly more specialized trigger paths that enhance the acceptance of events for targeted analysis areas of the CMS physics program. This includes "cross-object" triggers, such as mixed double-lepton ($e + \mu$) triggers that target, e.g., $H \to WW$, $H \to \tau\tau$, and top quark pair production in the dilepton final state, where H indicates the Higgs boson. Top quark acceptance is further enhanced in other decay topologies, such as lepton+jets or the all-hadronic channel. For the former, the E_T threshold on an electron can be reduced from that used in the inclusive single-electron trigger, with manageable rate increase, when used in coincidence with jets with a total scalar p_T sum (H_T) above a given threshold. Likewise, for the latter, the hadronic top quark decays can be selected via requirements on the number of jets, H_T, and one or more b-tagged jets. The B physics program of CMS generally targets soft dimuon final states, and thus uses additional requirements (e.g., invariant mass) in its HLT paths to keep trigger rates manageable. Since the overall list of these more specialized trigger paths numbers in the hundreds, their performances are not described here. However, the description and performance of the algorithms used for most of the individual objects forming these paths are discussed in this article.

3.4 Rates and processing time

The distribution of the CPU time spent in processing the HLT menu by reconstruction category and by instances of C++ classes within those categories is shown in figure 1. Overall, there are $O(1200)$ instances stemming from $O(200)$ algorithms that are run. The HLT configuration is based on the one used in 2018, with only minimal updates to the local reconstruction to reflect the ongoing developments foreseen for LHC Run 3. The timing is measured for an average PU of 50 during a 2018 data-taking period on a full HLT node (2× Intel Skylake Gold 6130) with hyper-threading enabled, running 16 jobs in parallel with 4 threads each. The average processing time per event is 451 ms; scaling this

2024 JINST 19 P11021

Table 2. Representative set of HLT paths based on the basic HLT physics objects used during data taking in 2018, the associated thresholds at the L1 and HLT, and the corresponding HLT output rates. The total menu rate at $\mathcal{L}_{\text{inst}} = 1.8 \times 10^{34}\,\text{cm}^{-2}\,\text{s}^{-1}$, representative near the start of an LHC fill, is 1.6 kHz.

HLT path	L1 thresholds [GeV]	HLT thresholds [GeV]	Rate [Hz]
Single muon	22	50	49
Single muon (isolated)	22	24	230
Double muon	22	37, 27	16
Double muon (isolated)	15, 7	17, 8	32
Single electron (isolated)	30	32	180
Double electron	25, 12	25, 25	16
Double electron (isolated)	22, 12	23, 12	32
Single photon	30	200	16
Single photon (isolated), barrel only ($\lvert\eta\rvert < 1.48$)	30	110	16
Double photon	25, 12	30, 18	32
Single tau	120	180	16
Double tau	32	35, 35	49
Single jet	180	500	16
Single jet with substructure	180	400	32
Multijets with b tagging	$H_{\text{T}} > 320$ jets $> 70, 55, 40, 40$	$H_{\text{T}} > 330$ jets $> 75, 60, 45, 40$	16
Total transverse momentum	360	1050	16
Missing transverse momentum	100	120	49

performance to the full event filter farm capacity means that it would be able to process an event input rate of approximately 130 kHz, above the nominal L1 rate target of 100 kHz.

Figure 2 illustrates the HLT rates attributed to each CMS physics group for the HLT menu deployed in September 2018, which selects data for prompt reconstruction. The rates were determined by running the HLT menu on a special data set where events were selected that passed the L1 trigger without any additional HLT requirements. The rates were normalized to an average $\mathcal{L}_{\text{inst}}$ of $1.8 \times 10^{34}\,\text{cm}^{-2}\,\text{s}^{-1}$. An event is attributed to a given physics group if the latter requires (i.e., owns) at least one of the HLT paths that triggered the event. For each physics group, three types of rates are evaluated.

- Total: the inclusive rate arising from all HLT paths needed by that physics group.
- Pure: the exclusive rate from all paths uniquely assigned to that physics group.
- Shared: the sum of the pure rate and the fractional rate of the HLT paths shared with other groups, where the rate is split equally among all groups for a given path.

The sum of the Shared HLT rates is 1530 Hz. However, because the selected data are recorded in separate data sets with some overlap (6.6%) for analysis and offline processing reasons, the actual storage rate is 1640 Hz with the additional duplication.

The CMS physics analysis groups focused on searches for physics beyond the SM are the B2G (searches for new physics in boosted signatures), SUSY (searches for new physics in final states with

2024 JINST 19 P11021

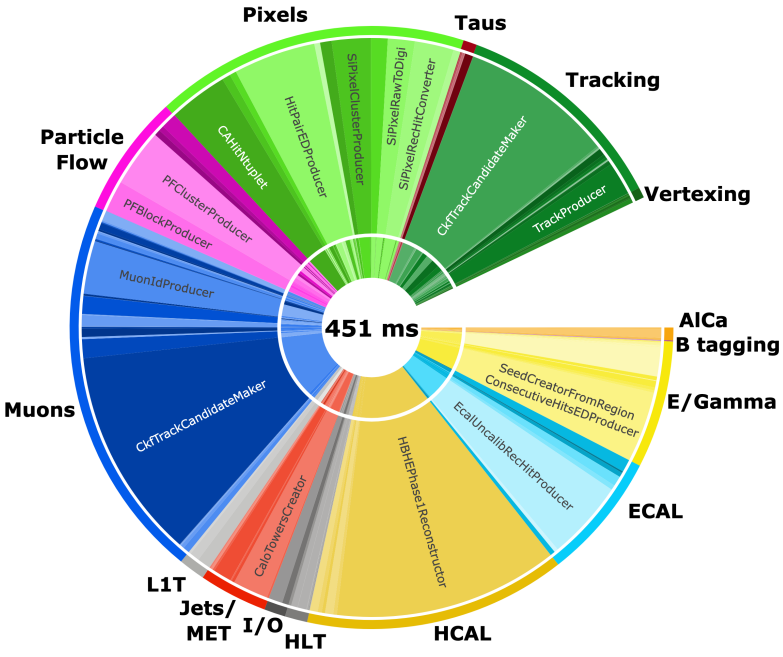

Figure 1. Pie chart distribution of the CPU time per event spent by the HLT for different parts of the event reconstruction. Reconstruction modules and filters are grouped by detector and physics object (outermost ring and similarly colored groupings). The middle ring reports the names of specific C++ classes in CMSSW used in the HLT reconstruction, and the various slices in the innermost ring refer to different instances (modules) of that given C++ class in the HLT menu. The empty slice indicates the time spent outside of the individual algorithms.

imbalanced p_{T}), and Exotica (other topologies of new physics) groups. The analysis groups focused on measurements are the Higgs boson physics, top quark physics, B physics, and other SM phenomena groups. The "Objects" category in figure 2 contains the HLT paths used by the physics object groups (Tracking, Muon, Electron-Photon, Jet-MET, Tau, b Tagging) to characterize the performance of the online and offline reconstruction. The "Calibrations" category includes all HLT paths used for subdetector alignment and calibration purposes.

The rate allocation per physics group is also expressed as a pie chart in figure 3. Very roughly one-third of the HLT rate budget is devoted to searches beyond the SM, one-third to measurements including the Higgs boson (but apart from B physics), and one-third to B physics and physics object groups.

4 The HLT reconstruction and performance

The HLT paths in the menu are based on physics objects produced from reconstruction modules that use information from the inner tracking system, calorimeters, and muon detectors. Central to many of the object reconstructions is the particle-flow (PF) algorithm [18], which aims to reconstruct all individual particles (electrons, muons, photons, and charged and neutral hadrons) in an event, combining information provided by these systems. The online PF reconstruction has a simplified version of the offline reconstruction to fulfill the timing limitation for online reconstruction. The tracking has a reduced number of iterations, down to three as discussed in section 4.1. Moreover, electron reconstruction is not

2024 JINST 19 P11021

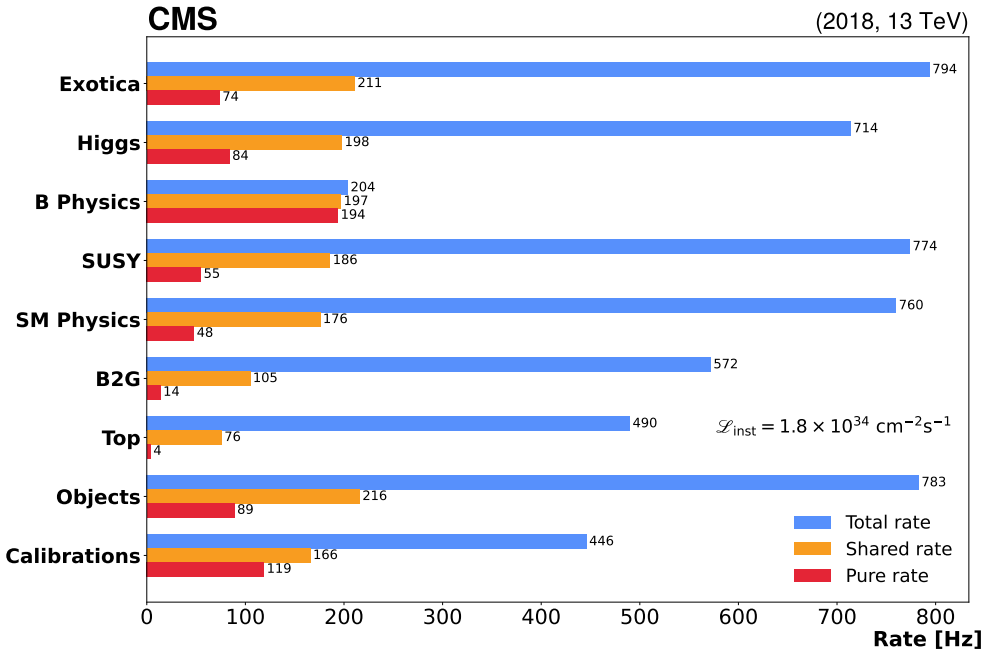

Figure 2. The HLT rate consumption by physics group in the standard physics streams for a Run 2 menu deployed in September 2018. The "Total Rate" is the inclusive rate of all triggers owned by a group, and the "Pure Rate" is the exclusive rate of all triggers unique to that group. The "Shared Rate" is the rate calculated by dividing the rate of each trigger equally among all physics groups that use it, before summing the total group rate. It includes the Pure Rate of that physics group. The topic coverage of each group is discussed in the text.

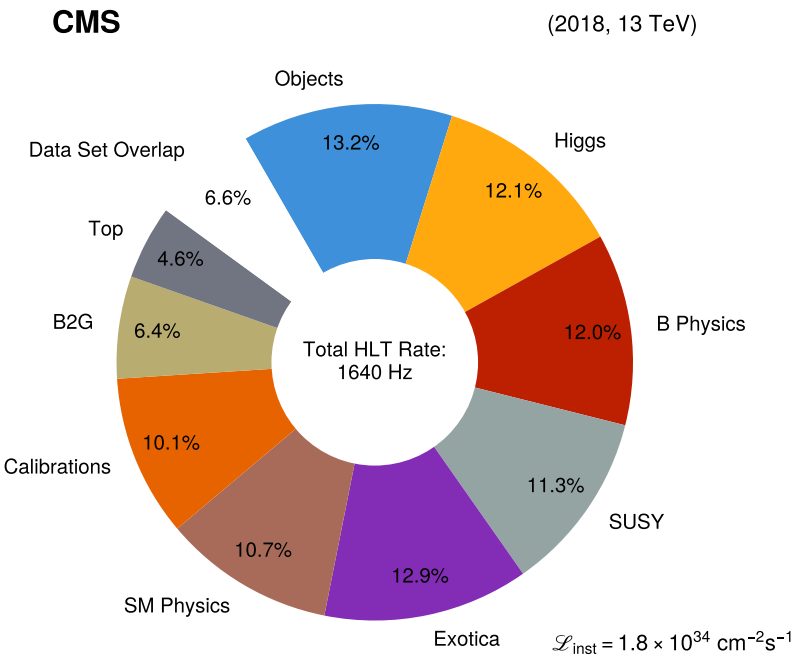

Figure 3. Share of the total HLT rate that each physics group contributes. "Data Set Overlap" refers to the events that are duplicated and saved into separate data sets for analysis and offline processing convenience, but which must be reconstructed separately offline.

2024 JINST 19 P11021

integrated into the online PF algorithm [18]. Brief descriptions of the HLT reconstruction algorithms for physics objects and highlights of their performance measured with data collected during Run 2 are described below. The measured efficiencies of the lepton (ℓ) algorithms are typically obtained using the "tag-and-probe" technique [19], which exploits resonant dilepton production (e.g., $\mathrm{Z} \to \ell\ell$ or $\mathrm{J}/\psi \to \ell\ell$) events in data. One of the lepton candidates, called the "tag," is required to satisfy a trigger requirement (e.g., a single-lepton trigger) such that the event is recorded irrespective of the other lepton, the "probe." Offline selection requirements are applied to both tag and probe to reduce the contribution of misidentified leptons. The trigger efficiency of the probe can then be measured in an unbiased way as a function of various kinematic and object quality parameters. The measured efficiencies of jets and energy sums are obtained using an unbiased data set, namely one triggered by a lepton.

4.1 Tracking

Charged particle tracks in the HLT are reconstructed from the hits in the pixel and strip tracker using a Kalman filtering technique [20], based on initial estimates of the track parameters obtained from hits in the pixel detectors ("seeds"). The seed is propagated outwards and the track parameters are updated with the information from compatible hits as they are found until no more hits are found or the tracker boundary is reached. The track is then propagated from the outermost hit inwards in search of additional compatible hits, after which a fit to the resulting hit collection determines the final track parameters. Similar to the offline track reconstruction [8], the tracking is performed iteratively, starting with tight requirements on the p_{T} and displacement with respect to the beam spot of the seed, which become looser for each subsequent iteration. Hits in the tracking detectors already used in a track are removed at the beginning of the next iteration. The general track reconstruction in the HLT consists of three iterations. The first two require the maximum of four consecutive pixel detector hits expected for one track from the detector geometry, identified using a cellular automaton algorithm [21], to seed (i.e., initiate) the tracking. These iterations first target high-p_{T} tracks before extending the coverage to low-p_{T} tracks, using the full volume of the pixel detector. The third iteration relaxes the requirement on the number of hits in the track seeds to three and is restricted to the vicinity of jet candidates identified from calorimeter information and the tracks reconstructed in the two previous iterations. Tracks are clustered into vertices using the same deterministic annealing algorithm [22] used in the offline reconstruction [8]. The vertex position is fitted using an adaptive vertex fitter [23].

This configuration of the track reconstruction was deployed in 2017, after the Phase-1 pixel detector was installed. Reflecting the lower number of detector layers, fewer pixel hits were required to form track seeds in previous years. The higher quality of track seeds available in 2017 resulted in an increase in tracking efficiency by about 10% for tracks with $p_{\mathrm{T}} > 1.2\,\mathrm{GeV}$, with larger improvements present at lower p_{T} and high $|\eta|$. At the same time, the track misidentification rate was reduced by a factor of 5–7.

During 2017, several issues with the installed Phase-1 pixel detector were identified that led to a nonnegligible fraction of inactive pixel detector modules in each event. Most notable was the failure of some direct-current DC-DC converters ($\approx$5%) used to power the detector, which resulted in an increasing fraction of inactive modules toward the end of the data-taking period [6].

During the year-end technical stop 2017–2018, the pixel detector was equipped with new converters, and the initial performance was restored. To safeguard against a possible recurrence of this problem and other possible detector failures, an additional recovery iteration was added. Track seeds consisting of just two pixel detector hits ("doublets") are created in regions of the detector where

2024 JINST 19 P11021

two inactive modules overlap as seen from the interaction point. Because of the limited CPU time available for the HLT reconstruction, this iteration is restricted to tracks with $p_{\mathrm{T}} > 1.2\,\mathrm{GeV}$.

The tracking efficiency and misidentification rate reported here are obtained from simulated top quark pair ($\mathrm{t\bar{t}}$) events with a mean PU of 50. The efficiency and rate are defined with respect to the Monte Carlo (MC) simulated objects, where the tracks of the simulated particles are matched to reconstructed tracks based on shared hits in the tracking detectors. The tracking efficiency is defined as the fraction of simulated particles from the signal interaction with $p_{\mathrm{T}} > 0.9\,\mathrm{GeV}$, $|\eta| < 2.5$, $d_{xy} < 35\,\mathrm{cm}$, and $d_z < 70\,\mathrm{cm}$ that are matched to a reconstructed track. The misidentification rate is defined as the fraction of reconstructed tracks that could not be matched to a simulated particle. To realistically model the effect of an imperfect pixel detector, a map of inactive modules representing the status of the real detector as of June 2018 is applied to the simulation. The tracking performance is implicitly included in the measured HLT object and algorithm performances that use tracking, reported in subsequent sections of this article.

The tracking efficiency as a function of p_{T}, number of PU interactions (N_{PU}), η, and ϕ is shown in figure 4. The reduction of efficiency at large track p_{T} is characteristic of the sample used for the efficiency measurement. As the inactive modules are not distributed uniformly throughout the detector, the tracking performance is expected to be asymmetric in track η and ϕ. For reference, the efficiency that would be achieved with the "design pixel detector", namely with no inactive pixel detector modules, is also shown in the figure. As the doublet-seeded iteration is not run in the case of the design detector, in some cases the tracking efficiency with the "realistic detector", which takes into account the pixel detector modules that have become inactive, can be higher than with the design detector. In the plateau region around $p_{\mathrm{T}} \approx 20\,\mathrm{GeV}$, the efficiency observed with the realistic detector conditions is about 5% lower than with the design detector. This efficiency loss compared with the design detector is more pronounced in the central part of the detector, and is concentrated in the region around $\phi = 0.6$, where a significant number of inactive modules is present. The doublet-seeded tracking iteration is able to recover a significant fraction of this efficiency loss above the p_{T} threshold of 1.2 GeV. The performance of the recovery procedure is not uniform across the η and ϕ ranges since it is invoked only if there are two overlapping inactive modules, making it dependent on the specific distribution of these modules. The tracking efficiency is robust against the presence of PU, decreasing only slightly with the number of additional interactions. The performance of the doublet-seeded recovery is also independent of PU.

The tracking misidentification rate as a function of p_{T}, N_{PU}, η, and ϕ is shown in figure 5. There is no difference between the misidentification rates with the design and realistic detector conditions. Taking into account the doublet-seeded recovery iterations, a slight increase of the misidentification rate above the p_{T} threshold of this iteration is observed. When integrated over all p_{T} values, no significant increase in the misidentification rate is observed for the doublet-seeded recovery iteration as seen in the other plots. The misidentification rate does increase with the number of additional PU interactions for either tracking scenario and for the design pixel detector.

4.2 Muons

Tracking algorithms are also deployed to identify and reconstruct muons measured in the muon detectors in combination with the pixel and strip trackers. Since the algorithms used during Run 2 are described in more detail in ref. [24], a brief summary is given here.

2024 JINST 19 P11021

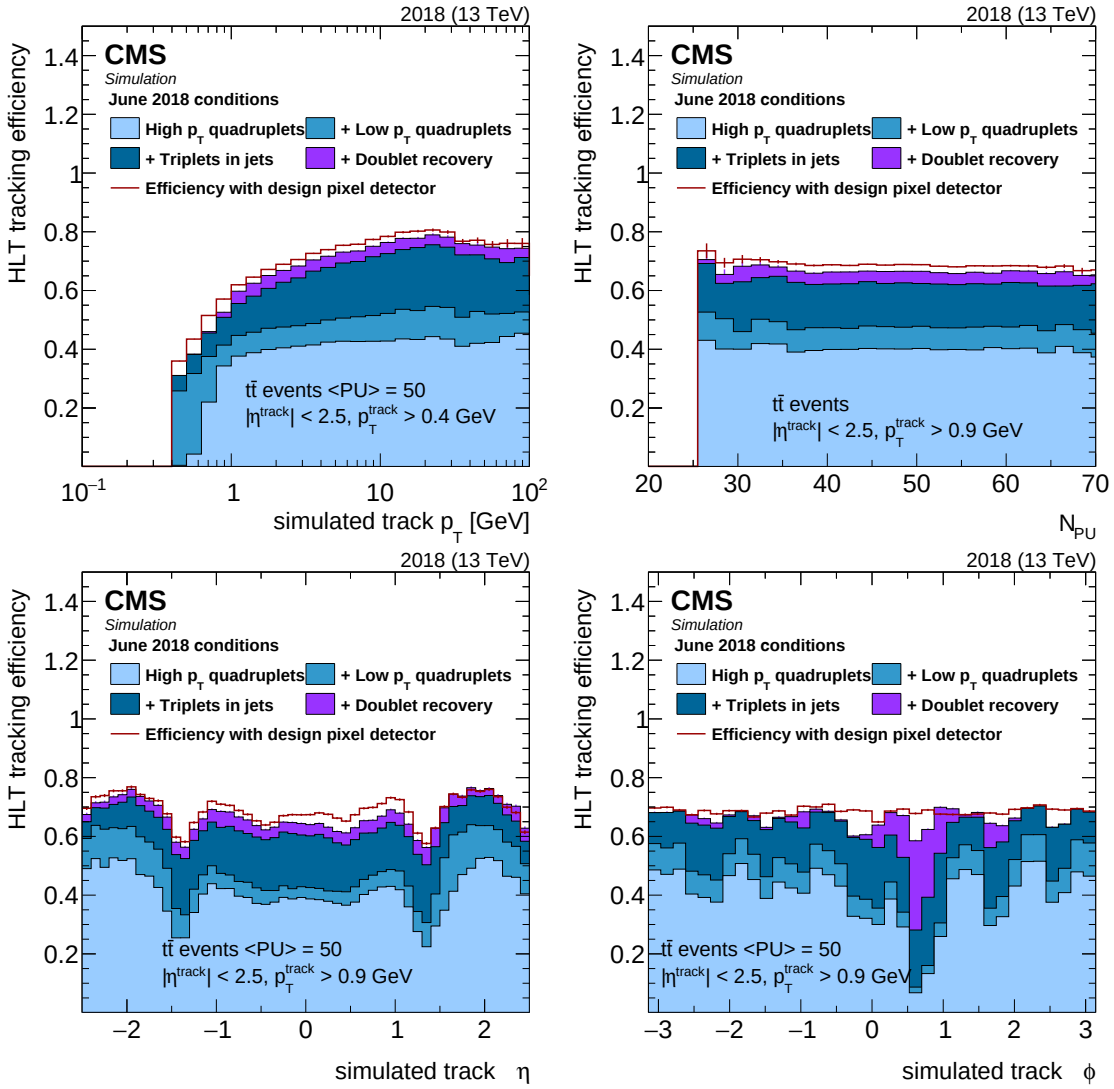

Figure 4. Tracking efficiency as a function of simulated track p_{T} (upper left), N_{PU} (upper right), η (lower left), and ϕ (lower right). The contributions to the total efficiency from the different tracking iterations are shown in different colors. The initial three iterations are shown in shades of blue, and the contribution of the doublet recovery iteration is shown in violet. The simulation includes a map of inactive modules representing the status of the real detector as of June 2018. The performance that would be achieved with no inactive pixel detector modules and no doublet recovery iteration (design pixel detector) is shown as a red line. Details of the observed features are discussed in the text.

Muon track reconstruction at the HLT takes place in two steps: first using hits only in the muon system (L2 reconstruction), followed by a combination with hits in the inner tracking system (L3 reconstruction). The L2 reconstruction is equivalent to the standalone muon reconstruction performed offline. The reconstruction at L3 is seeded by an L2 muon and follows an iterative track reconstruction similar to that described in the previous section in a region around the seed starting from the outer tracking layers and working inward ("outside-in") or from the inner tracking layers working out ("inside-out"). The latter inside-out approach also can be seeded directly by muons reconstructed by the L1 trigger ("L1 muons") using muon detector information only. The L3 track reconstruction is

2024 JINST 19 P11021

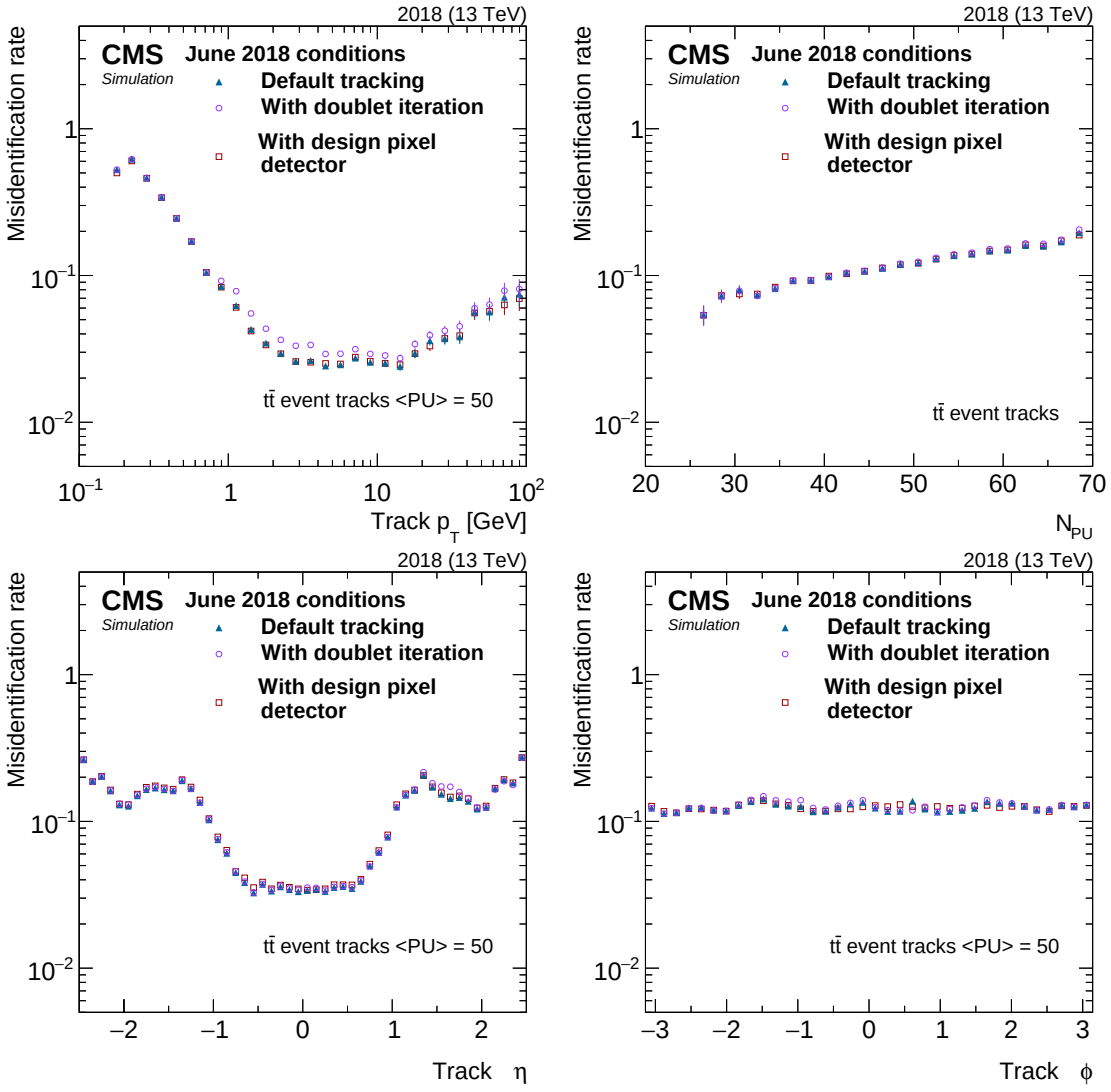

Figure 5. Tracking misidentification rate as a function of track p_{T} (upper left), N_{PU} (upper right), η (lower left), and ϕ (lower right). No selection on track kinematics is applied. The misidentification rate for the first three iterations (default tracking) is shown in dark blue triangles, whereas the misidentification rate after including the doublet recovery iteration is shown in violet circles. The simulation includes a map of inactive modules representing the status of the real detector as of June 2018. The misidentification rate that would be observed with no inactive pixel detector modules and no doublet recovery iteration (design pixel detector) is shown in dark red squares.

essentially 100% efficient with respect to L1-identified muons, and it reduces the rate by more than an order of magnitude for the same p_{T} threshold because of the improved momentum resolution of the inner tracking system. However, the L3 reconstruction consumes approximately 20% of the overall HLT CPU time per event. After the track reconstruction, identification criteria are applied as well as isolation criteria for the isolated muon category. The isolation is based on the sum of p_{T} from additional tracks associated with the primary vertex and calorimeter energy deposits clustered using an algorithm based on the PF candidates in a cone of radius $\Delta R = \sqrt{(\Delta\phi)^2 + (\Delta\eta)^2} = 0.3$ around the muon. The estimated contribution from PU to the energy deposits in the calorimeter is subtracted.

2024 JINST 19 P11021

The combined L1+HLT muon trigger efficiency of an isolated single-muon trigger with $p_T >$ 24 GeV with respect to offline-reconstructed muons is presented in figure 6 as a function of the data-taking date, which shows the effect of the evolution of the muon reconstruction algorithm during Run 2, as well as the detector and machine conditions. The maximum efficiency of about 90% is primarily set by the L1 trigger. Offline-reconstructed muons with $p_T > 26$ GeV are used. In 2016, two different approaches were used to reconstruct L3 muons. The first one (the "cascade" algorithm) starts from L2 muons as seeds and consists of three different methods to reconstruct L3 muons. Each method uses the outside-in or inside-out approach with different ways to find tracks in the inner tracker. The fastest method in calculation time is used first, and then it proceeds to the next methods only if an L3 muon is not found in the previous method. The other approach (the "tracker muon" algorithm) starts from L1 muons as seeds, which are used to define an inner tracker region to perform the track reconstruction. Reconstructed inner tracks matched to segments in the muon stations are then tagged as muons. By combining with the L3 muons from the cascade algorithm, it improves the overall performance, especially when L2 muons are not properly reconstructed. The performance was stable with an overall efficiency of about 90% during the whole of 2016 operations, showing robustness in early 2016 during a period of degradation of the inner strip tracking detectors before their operational parameters were retuned to reduce their susceptibility to highly ionizing particles.

In 2017, a new algorithm for the L3 muon reconstruction (the "iterative" algorithm) was implemented. It combines the advantages of both the cascade and tracker muon algorithms and replaced them. It starts with the outside-in step seeded by L2 and continues to find more L3 muons by two inside-out steps seeded by L2 or L1 muons. In early 2017, the performance of the initial version of the iterative algorithm was not as good as that of the previous algorithm, since a few technical weak points in the algorithm were not identified during validation with simulated events. The performance was consistently improved by implementing several patches during the data taking until the middle of 2017. However, the efficiency decreased later, mainly as a result of pixel detector module losses mentioned in the previous section and higher PU, as indicated in figure 6. The efficiency did rise nevertheless toward the end of 2017 and early 2018 because of a slight reduction in the amount of PU. To improve the robustness of the algorithm, significant changes were introduced in 2018. To recover the efficiency, all L1 muons were used in the L1-seeded step by removing the p_T requirement, and an iterative tracking step was added in the inside-out steps using the pixel doublet as seeds. In parallel, to improve the purity and rate, identification criteria were imposed on L3 muons at the last step of the algorithm. These improvements were implemented in May 2018 as denoted in the figure, restoring the efficiency to be similar to the 2016 level, up to the end of the Run 2 operation.

Figure 7 (left column) shows the efficiency of the isolated single-muon trigger with $p_T > 24$ GeV as a function of muon p_T, η, and the number of reconstructed primary vertices (N_{vtx}) for three years of data taking: 2016, 2017, and 2018. The right column of figure 7 shows the corresponding efficiency distributions for the nonisolated single-muon trigger with $p_T > 50$ GeV. The panel below each figure shows the ratio of the efficiency measured for data to that of simulation.

Figure 8 shows the efficiency of the same isolated single-muon trigger as in figure 7, plotted as a function of the η and ϕ of the muons. Different muon detector technologies and different reconstruction algorithms in both the L1 and HLT were used depending on the geometric region, but the overall efficiency is generally stable across Run 2, except for a few specific regions related to issues in the muon detector.

2024 JINST 19 P11021

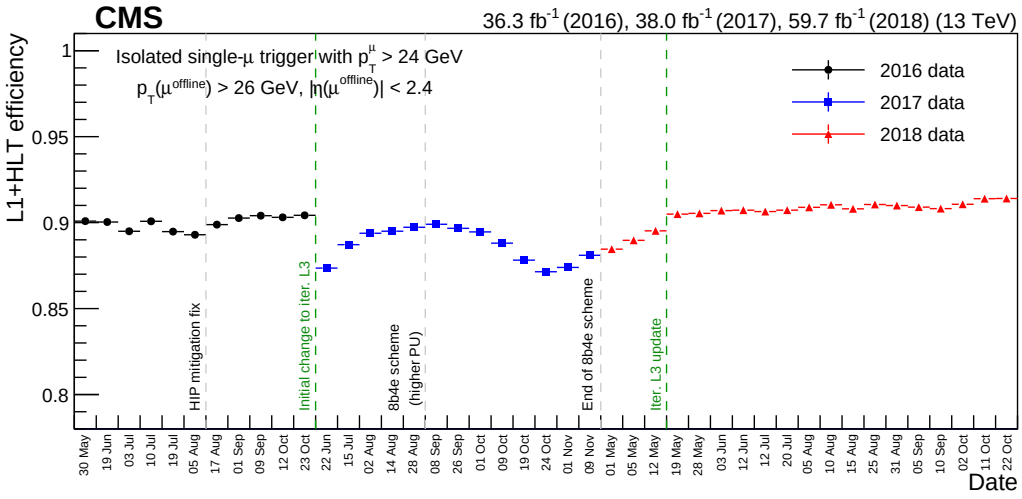

Figure 6. Evolution of the isolated single-muon trigger efficiency with $p_T > 24$ GeV as a function of data-taking dates during the Run 2 period from 2016 to 2018. Each point is the efficiency measured using the data with an integrated luminosity of about 3 fb^{-1}. Dashed lines show the changes in the LHC or CMS conditions that could have an impact on the trigger performance, such as the fix for the degradation of the inner tracker as a result of heavily ionizing particles ("HIP mitigation fix") or the change in the filling scheme for pp collisions at the LHC ("8b4e scheme") that led to higher PU in CMS until the end of 2017. The change of the reconstruction algorithm for L3 muons are presented as green dotted lines, including the replacement of cascade or tracker muon algorithm to the iterative algorithm ("Change to iter. L3") and the update of the iterative algorithm to overcome the limitations observed in 2017 ("Iter. L3 update").

The minimum p_T thresholds used for double-muon triggers are lower than those of single isolated muon triggers. As table 2 shows, the lower-p_T threshold of the isolated double-muon trigger used in the Run 2 trigger menu is 8 GeV. The efficiency of this lower-p_T "leg" is reported in ref. [24]. It exhibits a sharp turn-on in the efficiency vs. p_T at the threshold, with a plateau efficiency of ≈95% that is stable across the years 2016–2018 to within about 1%.

4.3 Electrons and photons

The electron and photon candidates at L1 are based on trigger towers defined by arrays of 5×5 ECAL crystals along with the HCAL tower directly behind them in the barrel, and in the endcaps are formed from groups of 5–25 crystals depending on their η-ϕ position [4]. The trigger tower with the largest E_T is clustered together with its adjacent E_T towers using a procedure that also trims the energy deposits to only include contiguous towers to match the electron or photon signature in the calorimeter. To form an L1 candidate, energy clusters must satisfy additional identification criteria and, optionally, isolation requirements. The HLT electron and photon identification begins with a regional reconstruction of the energy deposited in the ECAL crystals around the L1 candidates. In Run 2, the signals in the ECAL crystals are reconstructed by fitting the signal pulse with multiple template functions, to mitigate out-of-time PU. The signal amplitudes are then corrected by per-crystal correction factors and per-channel calibration techniques, which, to deal with the increasing ECAL crystal opacity from radiation damage, require frequent updates to maintain performance. Clusters of ECAL deposits within a certain geometric area around the seed cluster, called "superclusters," are then built, using the same reconstruction algorithm as used offline [25]. However, the energy

2024 JINST 19 P11021

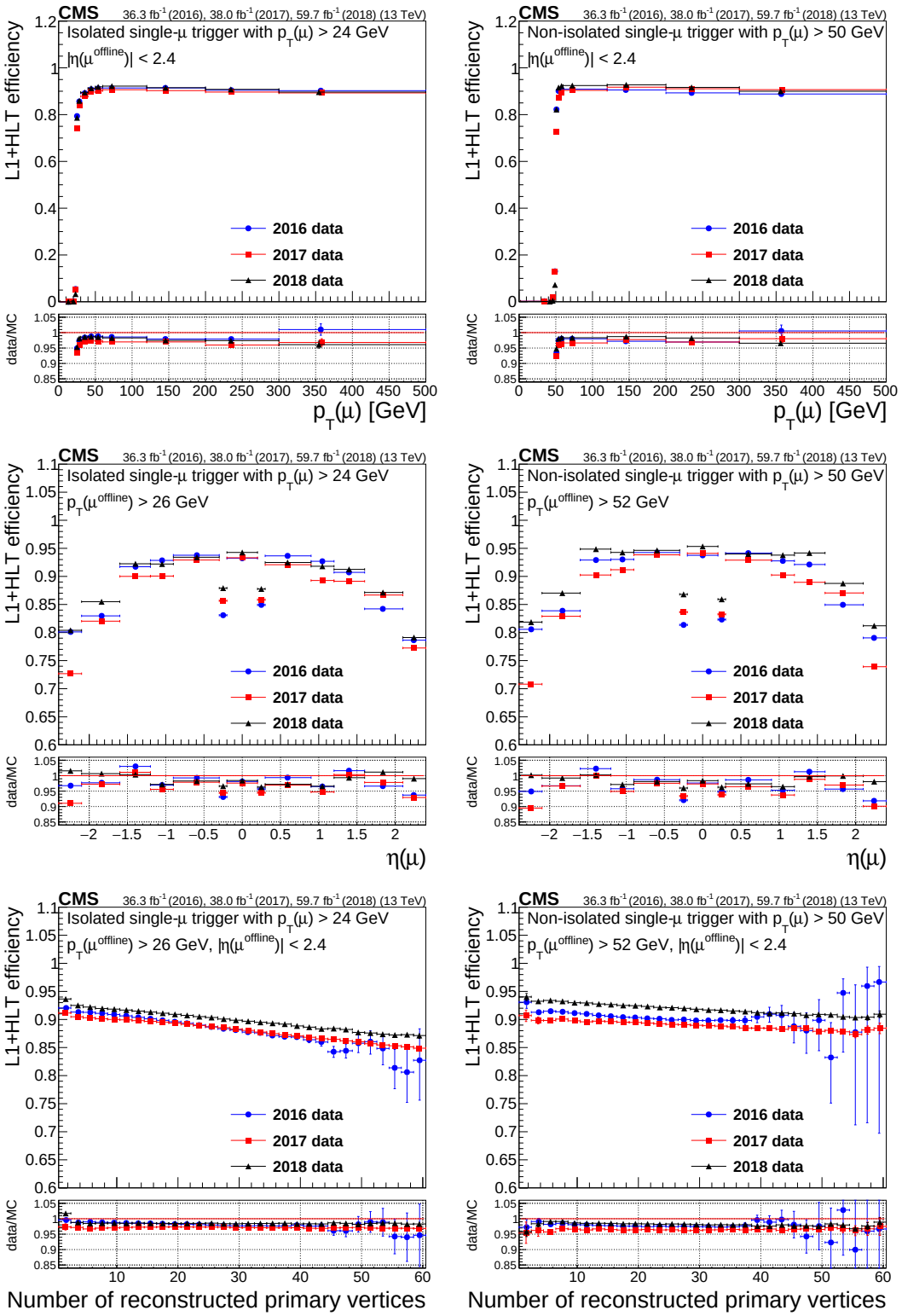

Figure 7. Trigger efficiencies for the isolated single-muon trigger with $p_{\mathrm{T}} > 24\,\mathrm{GeV}$ (left column) and the nonisolated single-muon trigger with $p_{\mathrm{T}} > 50\,\mathrm{GeV}$ (right column), as functions of muon p_{T} (upper row), η (middle row), and N_{vtx} (lower row). The lower panel of each plot shows the ratio of data to MC simulation The vertical bars on the markers represent statistical uncertainties.

2024 JINST 19 P11021

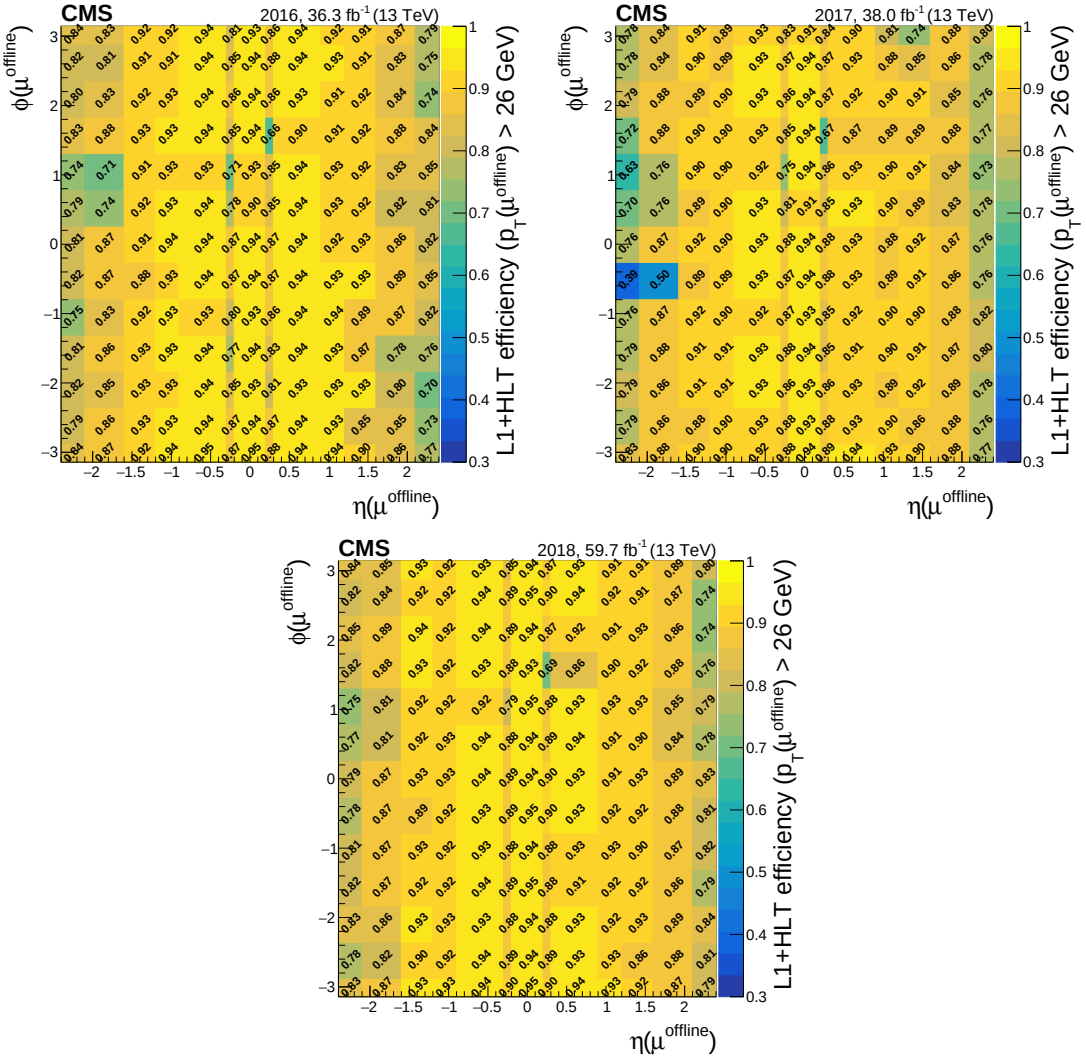

Figure 8. Efficiency of the isolated single-muon trigger with $p_{\mathrm{T}} > 24\,\mathrm{GeV}$ as a function of the η and ϕ of the muons in 2016 (upper left), 2017 (upper right), and 2018 (lower).

correction applied to HLT superclusters is simpler than the one used offline in that it employs ECAL information only. This correction is needed to take into account possible energy losses of the electrons and photons travelling through the detector material. After requesting a minimal threshold on the energy, requirements are applied based on properties of the energy deposits in the ECAL and HCAL subdetectors, according to the compactness and shape of electromagnetic showers. In the case of electrons, the ECAL supercluster is associated with a reconstructed track with a direction compatible with the cluster location. The first step is a match with pixel detector hits. Since 2017, the pixel matching algorithm requires three pixel detector hits rather than two, to maximize early background rejection, while a hit doublet is accepted only if the trajectory passes through a maximum of three active modules. Once the supercluster is associated with the pixel detector seeds, the electron track is reconstructed using a dedicated tracking algorithm, based on the Gaussian sum filter [26]. However, not all electron HLT paths run this algorithm: in some cases, sufficient rate reduction is already achieved from pixel detector matching alone.

2024 JINST 19 P11021

Single- and double-electron triggers are the first selection step of most analyses using electrons. In the following, their performance is reported, using the full 2016, 2017, and 2018 data sets, corresponding to an integrated luminosity of 136 fb^{-1} [27–29]. The performance of photon triggers, which are very similar to those of electron triggers apart from the absence of the requirement on the presence of matching tracks, is not reported here. This is because photon triggers are typically designed for specific analyses and are not used as extensively.

Table 3. Tag-and-probe selections used for the single- and double-electron trigger efficiency determination.

Tag selection	Probe selection
$p_{\text{T}} > 30$ (35) GeV in 2016 (2017–2018)	$p_{\text{T}} > 5$ GeV
$\lvert\eta\rvert < 2.1$ (except $1.44 < \lvert\eta\rvert < 1.57$)	$\lvert\eta\rvert < 2.5$
Tight isolation and shower shape requirements	No extra identification criteria
Passing the single-electron HLT path	
with $p_{\text{T}} > 27$ (32) GeV in 2016 (2017–2018)	

The tag-and-probe selections [30] used to measure the efficiencies are listed in table 3. Probes are then required to pass the HLT path under study. The analyzed triggers are the following, being those used by most of the physics analyses involving electrons:

- Single-electron trigger with tight identification and isolation requirements: electron $p_{\text{T}} > 27$ (32) GeV in 2016 (2017–2018).
- Double-electron trigger with loose identification and isolation requirements: highest-(lowest-)p_{T} electron $p_{\text{T}} > 23$ (12) GeV.

The identification requirements are based on the shower shapes in ECAL and HCAL, and the isolation requirements on energy and momentum sums in a cone around the electron. Figures 9–13 show the L1+HLT efficiency of these two electron triggers with respect to an offline-reconstructed electron as a function of the electron p_{T} and N_{vtx}, for different η regions of the supercluster. The offline-reconstructed electron efficiency is typically above 95% for electrons with $p_{\text{T}} > 20$ GeV [31]. The lower panel of each plot shows the ratio of the efficiency for data to MC simulation. The data/MC discrepancy in the turn-on at low p_{T}, seen for all years and η values, mainly comes from the small differences that exist between the online and offline ECAL response corrections [31]. Small inefficiencies that arose during 2017 from L1 energy clusters misassigned to the previous bunch crossing at high p_{T} [4] primarily affect higher $\lvert\eta\rvert$ than reported here.

The single-electron trigger performance reported in figures 9 and 10 is affected by a change in the strict identification and isolation selections required in this HLT path, which together are known as the tight working point, whose target is a signal efficiency of about 80%. These criteria were retuned in 2017, and some requirements in the endcap were loosened. Consequently, the single-electron trigger efficiency is higher for 2017 and 2018 with respect to 2016, in particular at high η values. The different shape as a function of p_{T} in 2016 with respect to 2017 and 2018 arises mainly from the different energy threshold, namely, 27 instead of 32 GeV. In 2017, the CMS pixel detector was upgraded by introducing extra layers in the barrel and forward regions, and a commissioning period at the beginning of the year led to a slightly reduced efficiency. As a consequence of the upgraded detector, the algorithm used to reconstruct electrons matching ECAL superclusters to pixel

2024 JINST 19 P11021

detector tracks was revised, causing a significant rate reduction for a minimal performance loss. However, problems with the pixel detector DC-DC converters (discussed in section 4.1) led to a gradual efficiency reduction towards the end of the year. Moreover, the majority of the high PU data in 2017 also came toward the end of that year. Thus, for these reasons, the single-electron trigger performance in 2017 is slightly worse than in 2018.

The efficiency of the double-electron trigger, shown in figures 11–13, is in general higher in the turn-on region in 2016 compared with 2017 and 2018. This is because the E_{T} thresholds of the lowest unprescaled L1 seed requiring two electrons, which seeds this path, increased across the years. The effect is especially evident at low p_{T}. Moreover, the 2017 trigger performance is slightly worse than the other years because of the issues related to the pixel detector and PU described in the previous paragraph. More details are reported in ref. [31].

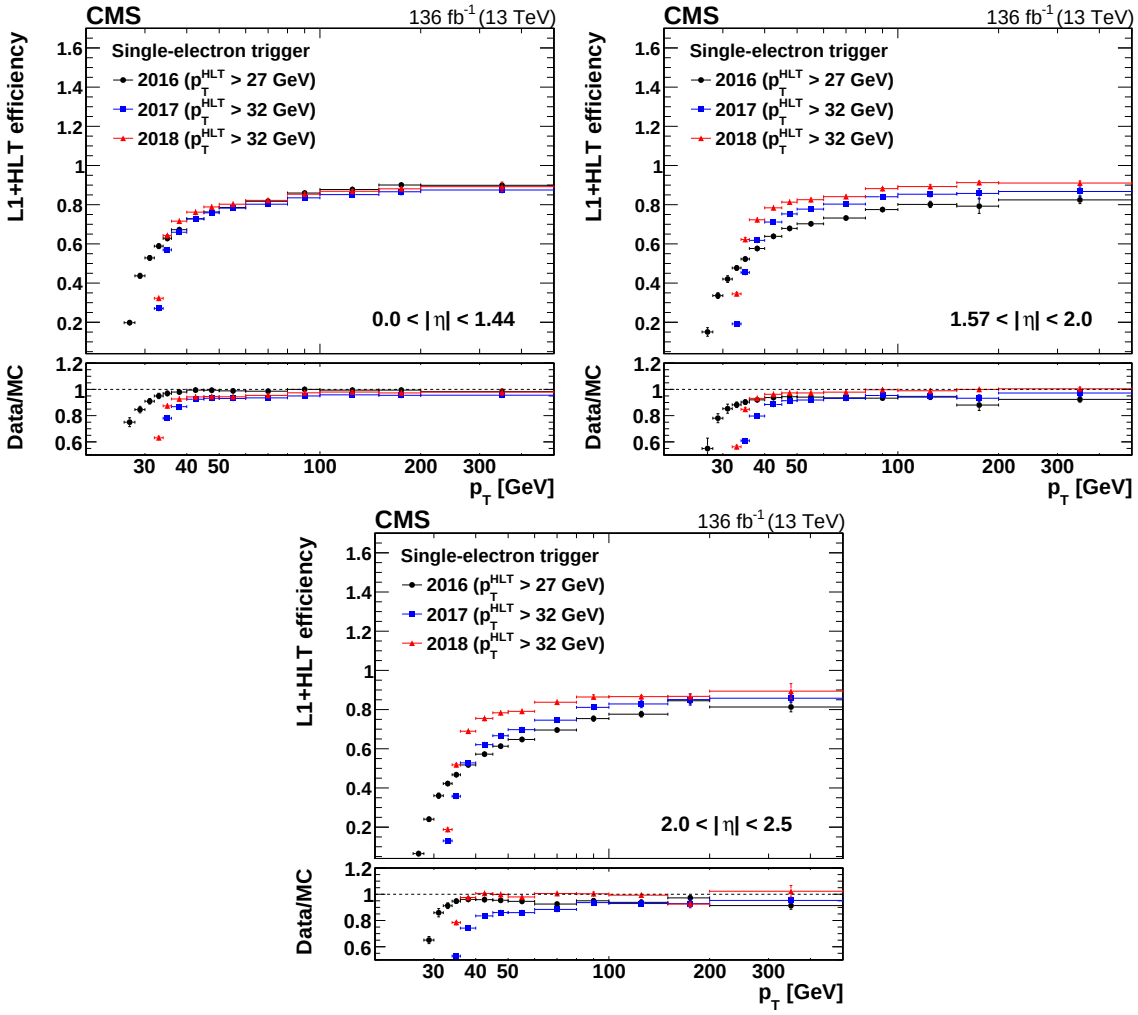

Figure 9. The L1+HLT efficiency of the single-electron HLT path with $p_{\mathrm{T}} > 27$ (32) GeV in 2016 (2017 and 2018) with respect to an offline-reconstructed electron as a function of the electron p_{T}, obtained for $0 < |\eta| < 1.44$ (upper left), $1.57 < |\eta| < 2.0$ (upper right), and $2.0 < |\eta| < 2.5$ (lower). The lower panel of each plot shows the ratio of data to MC simulation. The vertical bars on the markers represent combined statistical and systematic uncertainties.

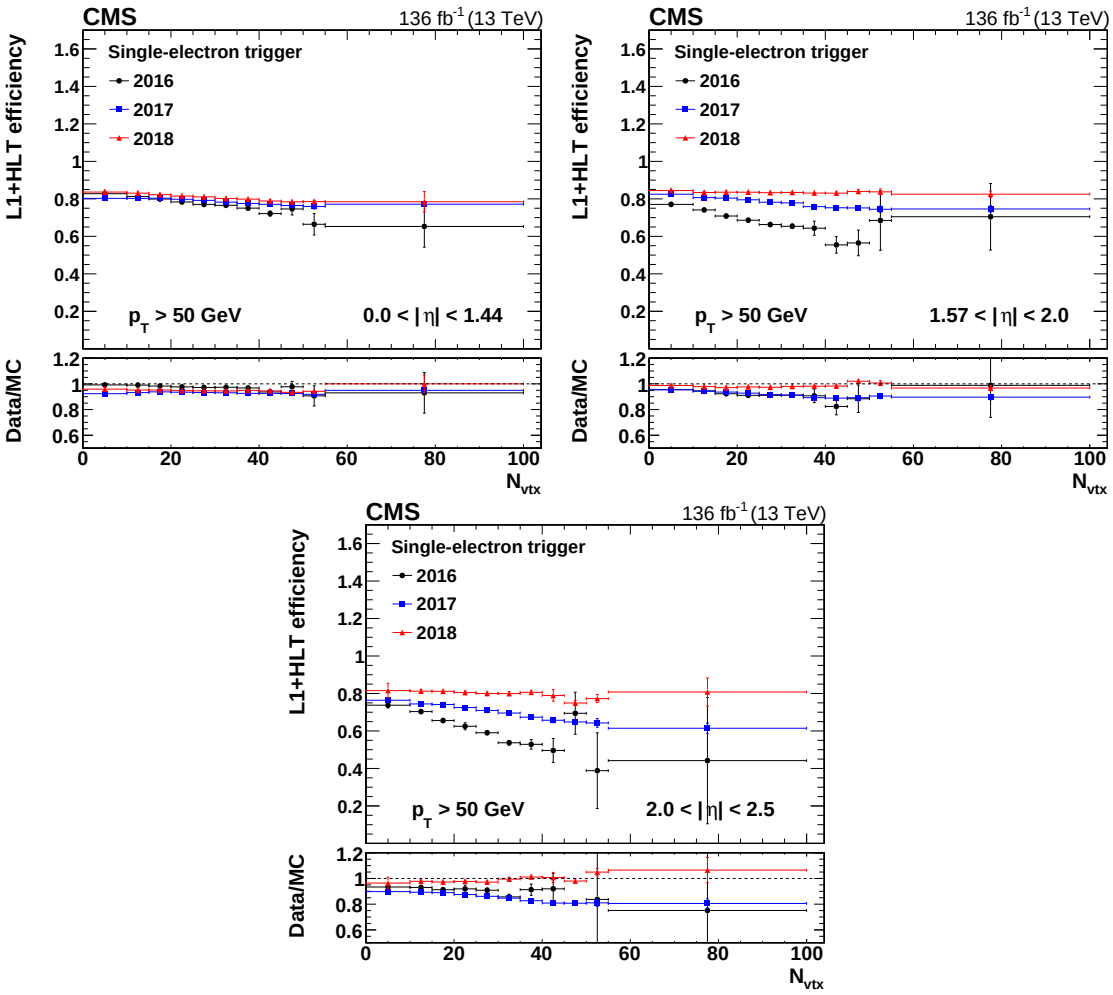

Figure 10. The L1+HLT efficiency of the single-electron HLT path with $p_{\mathrm{T}} > 27$ (32) GeV in 2016 (2017 and 2018) with respect to an offline-reconstructed electron as a function of N_{vtx}, obtained for $0 < |\eta| < 1.44$ (upper left), $1.57 < |\eta| < 2.0$ (upper right), and $2.0 < |\eta| < 2.5$ (lower). The electron p_{T} is required to be above 50 GeV. The lower panel of each plot shows the ratio of data to MC simulation. The vertical bars on the markers represent combined statistical and systematic uncertainties.

4.4 Jets

Jets are reconstructed at the HLT using the anti-k_{T} clustering algorithm [32] with a nominal distance parameter of 0.4, and 0.8 for wide jets used in Lorentz-boosted topologies and multijet triggers. The inputs for the jet algorithm can be either calorimeter towers or reconstructed objects from the PF algorithm. Most HLT jet paths use the PF inputs ("PF-jets"), whereas calorimeter jets ("Calo-jets") are used as a first step to identify jet signatures and initiate the PF reconstruction. To account for detector and collision conditions, several corrections are applied to the estimated PF hadron energies, average PU energy, and jet energy scale. The performance of the jet triggers is measured in terms of their efficiency to select events that have an offline-reconstructed jet. For this purpose, an unbiased set of pp collision events collected with an isolated single-muon trigger with a $p_{\mathrm{T}} > 27$ GeV requirement is used. The events are required to have exactly one loosely identified offline muon with $p_{\mathrm{T}} > 10$ GeV within $|\eta| < 2.4$, which has a relative isolation value less than 0.4 in a ΔR cone of radius 0.4 to match

2024 JINST 19 P11021

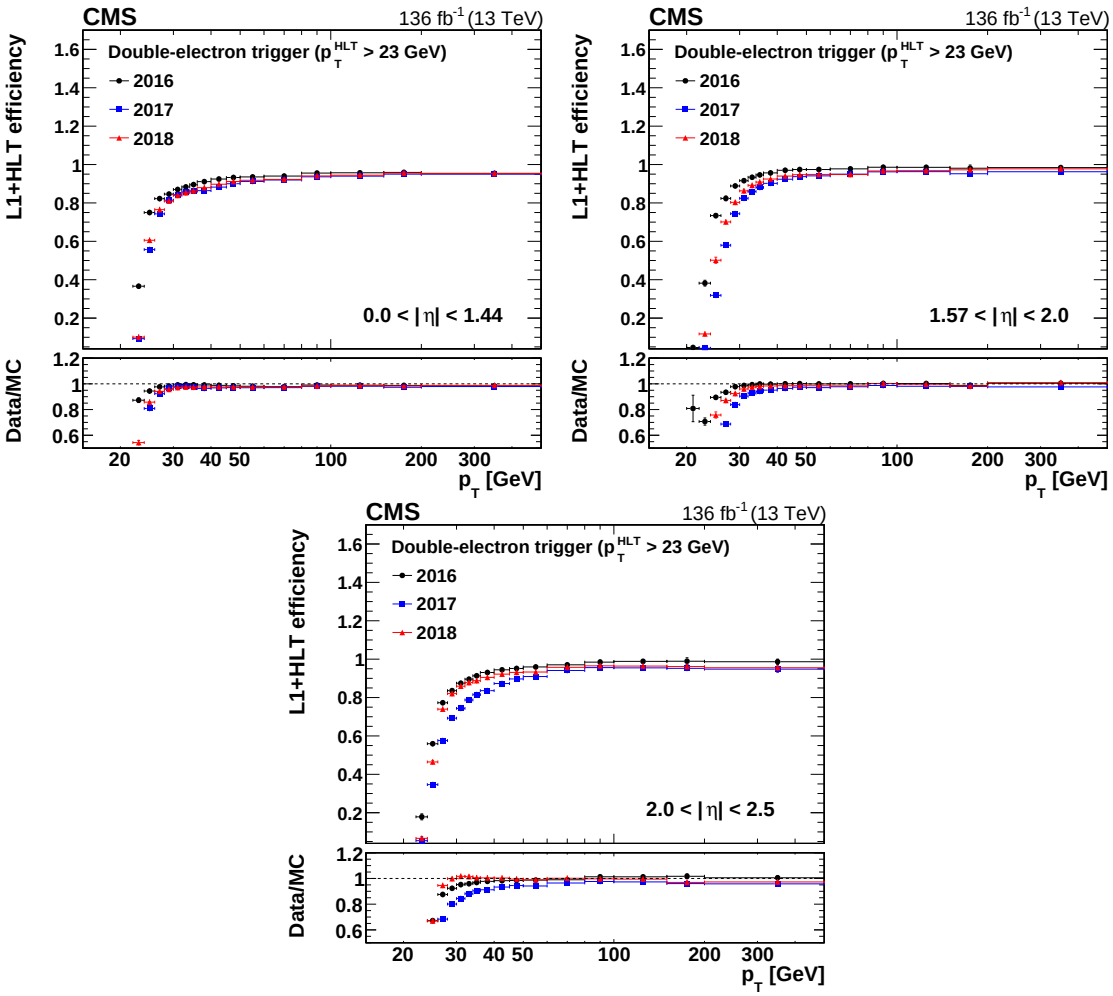

Figure 11. The L1+HLT efficiency of the $p_T > 23$ GeV leg of the double-electron trigger with respect to an offline-reconstructed electron as a function of the electron p_T, obtained for $0 < |\eta| < 1.44$ (upper left), $1.57 < |\eta| < 2.0$ (upper right), and $2.0 < |\eta| < 2.5$ (lower). The lower panel of each plot shows the ratio of data to MC simulation. The vertical bars on the markers represent combined statistical and systematic uncertainties.

the trigger criteria. Any events with additional loosely identified electrons having $p_T > 10$ GeV within $|\eta| < 2.5$ are rejected to ensure that the chosen data have high purity of hadronic jets in the event. The offline-reconstructed PF jets used in the measurement are clustered using the anti-k_T algorithm with radius 0.4; have $p_T > 18$ GeV within $|\eta| < 2.4$; and pass selection criteria based on the charged-hadron fraction, number of constituents, etc. that are able to reject a good fraction of leptons misidentified as jets. Events are selected requiring at least one such offline jet that is well separated from the offline muon by a ΔR of at least 0.4, so that the muon lies outside the reconstructed jet radius.

The efficiency is defined as the ratio of the number of events that have an HLT PF jet that passes the trigger threshold and matches the highest-p_T offline PF jet within $\Delta R < 0.2$, to the total number of events with a reconstructed offline jet. The efficiency for the lowest threshold unprescaled single PF jet trigger as a function of the offline PF jet p_T is shown separately for each data-taking year in figure 14. Results are shown for the total integrated luminosities collected in each year during 2016, 2017, and 2018. For a trigger threshold of 500 GeV, the efficiency reaches 100% at about 600 GeV in the offline

2024 JINST 19 P11021

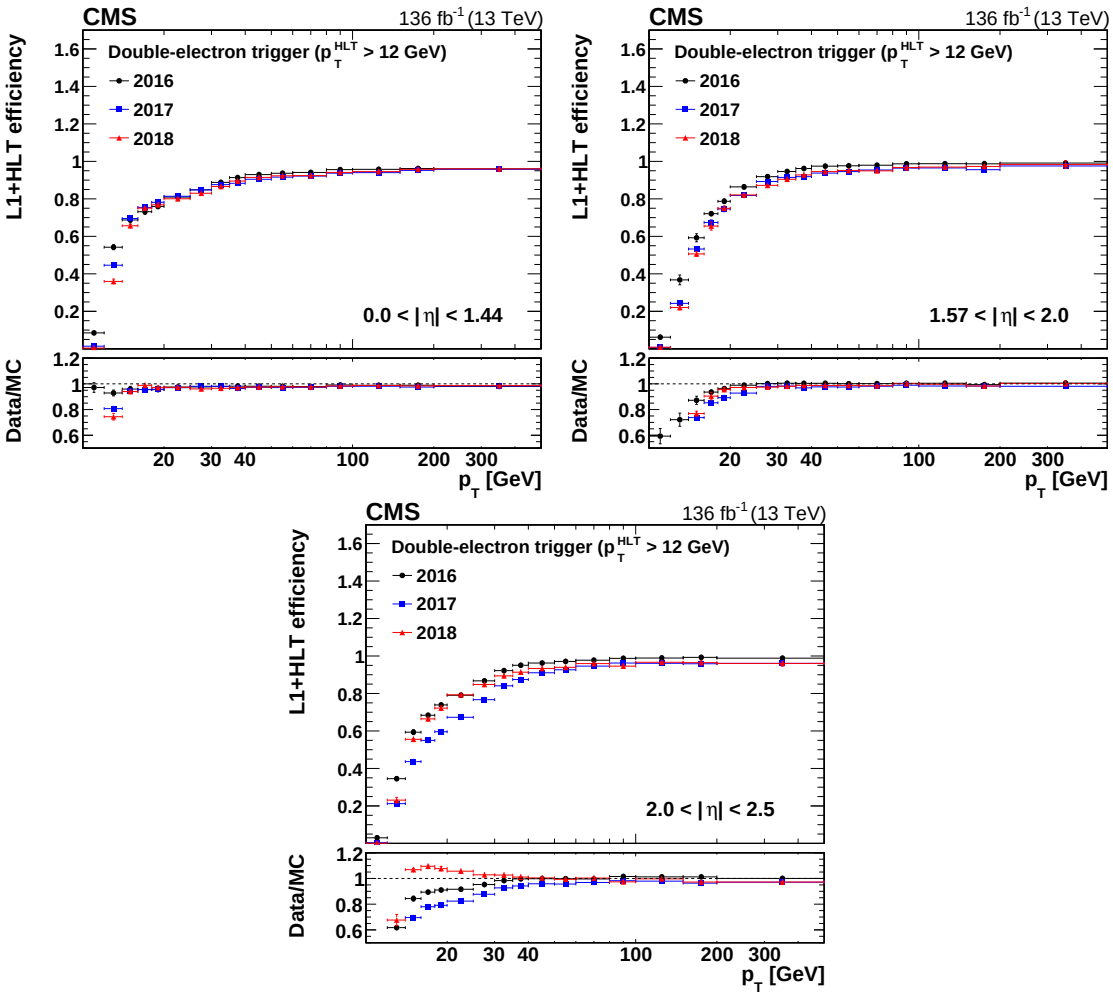

Figure 12. The L1+HLT efficiency of the $p_T > 12$ GeV leg of the double-electron trigger with respect to an offline-reconstructed electron as a function of the electron p_T, obtained for $0 < |\eta| < 1.44$ (upper left), $1.57 < |\eta| < 2.0$ (upper right), and $2.0 < |\eta| < 2.5$ (lower). The lower panel of each plot shows the ratio of data to MC simulation. The vertical bars on the markers represent combined statistical and systematic uncertainties.

reconstructed jet p_T for all three years. The jet trigger efficiency, measured as a function of the offline reconstructed jet p_T, is affected by the calibration of the offline-reconstructed jets. The offline jet energy corrections were recalculated multiple times during Run 2, whereas only one set of online calibrations were used. Hence, depending on the energy scale and resolution of the offline-reconstructed jets, the turn-on of the efficiency curve can be shifted and become slightly faster or slower.

4.5 Scalar energy sums

The global H_T energy sum is based on the scalar sum of jet p_T, and is sensitive to multijet signatures. The same set of unbiased events triggered by an isolated muon, described in the previous section, is used to measure the efficiency of H_T triggers. The event preselection requirements based on leptons are also the same. To suppress the effects from PU, the H_T reconstructed at the HLT is calculated using HLT PF jets having $p_T > 30$ GeV within $|\eta| < 2.4$. The same p_T and η requirements are also applied to

2024 JINST 19 P11021

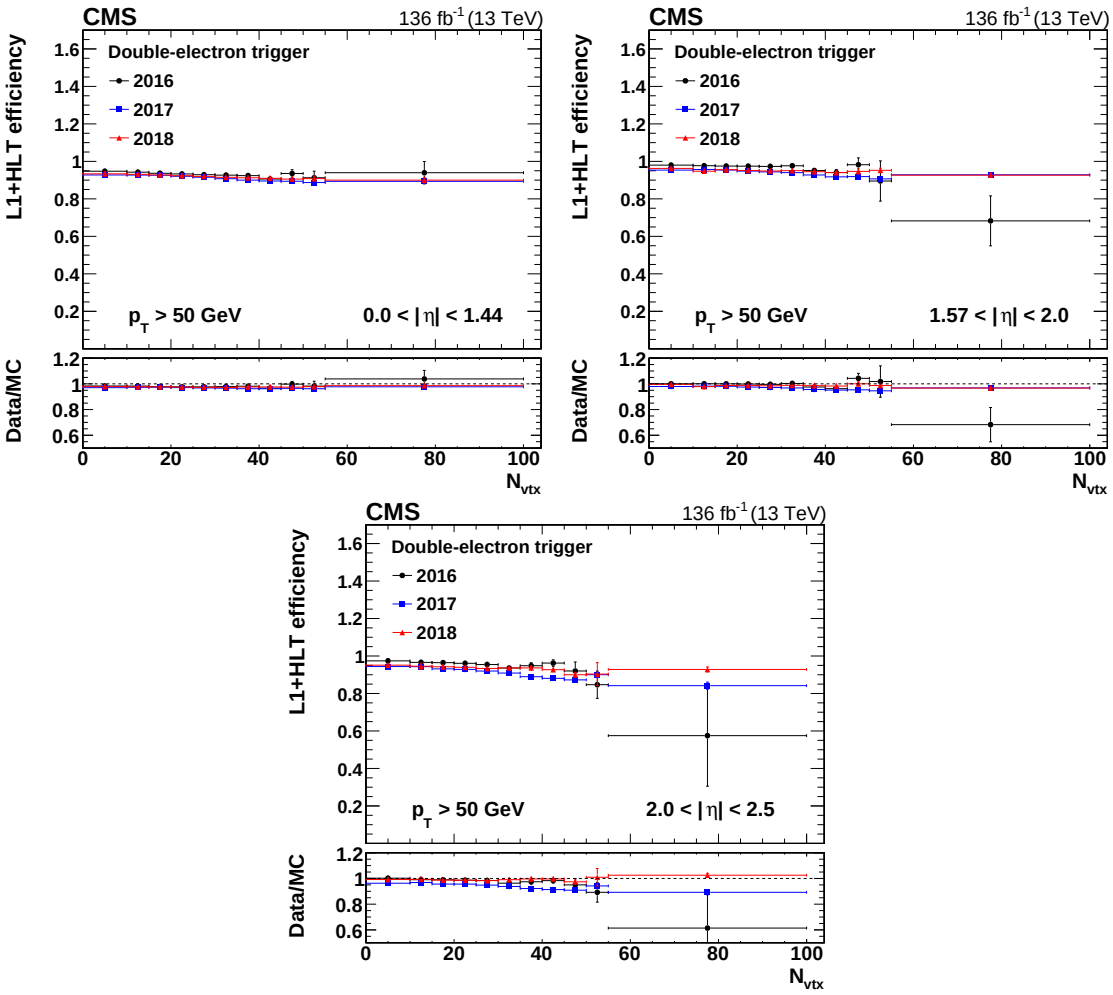

Figure 13. The L1+HLT efficiency of either leg of the double-electron trigger with respect to an offline-reconstructed electron as a function of N_{vtx}, obtained for $0 < |\eta| < 1.44$ (upper left), $1.57 < |\eta| < 2.0$ (upper right), and $2.0 < |\eta| < 2.5$ (lower). The electron p_{T} is required to be above 50 GeV. The lower panel of each plot shows the ratio of data to MC simulation. The vertical bars on the markers represent combined statistical and systematic uncertainties.

the offline-reconstructed PF jets to calculate the offline H_{T}, in addition to passing the jet identification criteria. The offline jets are required to be separated from the offline muon by a ΔR of at least 0.4.

The trigger efficiency is defined as the ratio of the number of events where the H_{T} at the HLT passes the applied threshold to the total number of events selected by the offline H_{T} algorithm with the same threshold. The performance of the unprescaled H_{T} triggers with the lowest thresholds, as a function of the offline H_{T}, is shown separately in figure 15 for the total integrated luminosities collected during 2016, 2017, and 2018. During 2016, a lower threshold of 900 GeV was applied online and was increased in subsequent years to maintain a similar total trigger rate as the $\mathcal{L}_{\text{inst}}$ increased. This is because H_{T} is highly sensitive to PU events, causing a nonlinear increase in the trigger rate.

For an online threshold of 1050 GeV, the efficiency reaches 100% at about 1300 GeV in the offline-calculated H_{T}. The H_{T} trigger efficiency for 2016 was lower because of an effect in the L1 trigger seed firmware implementation that limited the plateau to < 100%.

2024 JINST 19 P11021

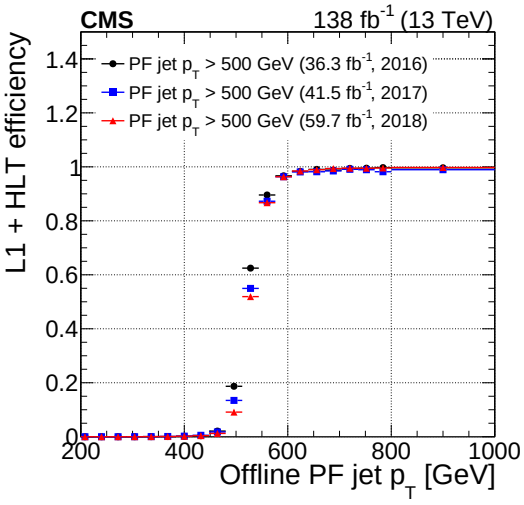

Figure 14. The L1+HLT efficiency of the unprescaled single PF jet trigger having an online p_{T} threshold of 500 GeV, measured with respect to the offline reconstructed PF jet p_{T}, for the data collected using an unbiased single-muon trigger during 2016, 2017, and 2018. The slight variation in turn-on curve is caused by differences in offline jet energy scale calibrations. The vertical bars on the markers represent statistical uncertainties.

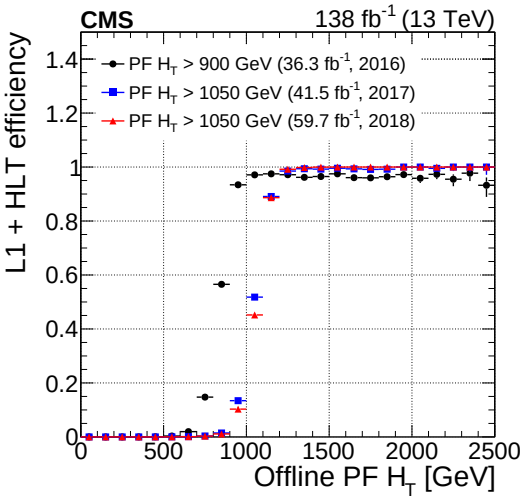

Figure 15. The L1+HLT efficiency of the unprescaled H_{T} triggers with the lowest thresholds, measured with respect to the offline-reconstructed H_{T}, for the data collected during 2016, 2017, and 2018. The inefficiency for 2016 is caused by an effect in the L1 trigger seed firmware implementation. The vertical bars on the markers represent statistical uncertainties.

4.6 Missing transverse momentum

At the HLT, the missing transverse momentum is defined as the negative vector sum of the p_{T} of all the PF candidates in an event, and its magnitude is denoted as $p_{\mathrm{T}}^{\mathrm{miss}}$. It is crucial to account for the instrumental effects of noise and beam-induced backgrounds to keep the rates of these triggers within reasonable limits. Additional filtering algorithms are applied during reconstruction to achieve lower rates for $p_{\mathrm{T}}^{\mathrm{miss}}$ triggers. Calorimeter deposits consistent with noise signature or beam halo are removed from the energy sum computation at the HLT.

The performance of the $p_{\mathrm{T}}^{\mathrm{miss}}$ triggers is measured with respect to the offline-reconstructed $p_{\mathrm{T}}^{\mathrm{miss}}$ also based on PF candidates and including jet energy corrections, referred to as corrected $p_{\mathrm{T}}^{\mathrm{miss}}$. An unbiased sample of events, triggered by a single isolated electron of $p_{\mathrm{T}} > 32\,\mathrm{GeV}$, is used for this measurement. To match the online requirement, the events must contain exactly one well-identified and isolated offline electron, having $p_{\mathrm{T}} > 35\,\mathrm{GeV}$ within $|\eta| < 2.5$ and passing the electron identification criteria based on track quality and electromagnetic shower shape variables. Events with any additional loosely identified electrons or with muons with $p_{\mathrm{T}} > 10\,\mathrm{GeV}$ are excluded.

The trigger efficiency is defined as the ratio of the number of events that satisfy a given online $p_{\mathrm{T}}^{\mathrm{miss}}$ threshold requirement to the total number of events selected by the offline $p_{\mathrm{T}}^{\mathrm{miss}}$ algorithm with the same threshold. The performance of the unprescaled triggers with the lowest thresholds using the total integrated luminosities collected during 2016, 2017, and 2018, is shown in figure 16. Since $p_{\mathrm{T}}^{\mathrm{miss}}$ triggers are also susceptible to PU effects similar to H_{T} triggers, the thresholds are different in the three years because of variations in the $\mathcal{L}_{\mathrm{inst}}$. For a trigger of threshold of 170 GeV, the efficiency reaches 100% for an offline $p_{\mathrm{T}}^{\mathrm{miss}}$ of about 350 GeV in 2016, with a similar performance seen in later years for slightly shifted thresholds.

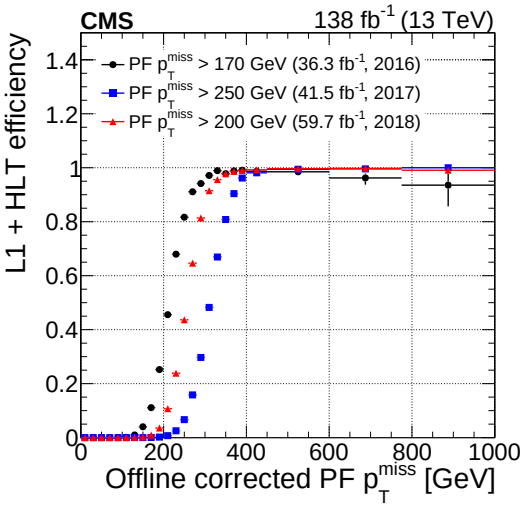

Figure 16. The L1+HLT efficiencies of the unprescaled $p_{\mathrm{T}}^{\mathrm{miss}}$ triggers with the lowest thresholds, measured with respect to the offline-reconstructed corrected $p_{\mathrm{T}}^{\mathrm{miss}}$, for the data collected during 2016, 2017, and 2018. The vertical bars on the markers represent statistical uncertainties.

At the HLT, online jet energy corrections can also be propagated to the calculation of the $p_{\mathrm{T}}^{\mathrm{miss}}$ similar to that performed offline. Figure 17 (left) compares the performance of the nominal and corrected $p_{\mathrm{T}}^{\mathrm{miss}}$ at the HLT for the 2018 data-taking year. The trigger with corrected $p_{\mathrm{T}}^{\mathrm{miss}}$ has a slightly faster turn-on compared with that of the nominal $p_{\mathrm{T}}^{\mathrm{miss}}$ trigger having the same threshold. However, the rate of the corrected $p_{\mathrm{T}}^{\mathrm{miss}}$ trigger is also observed to increase by about 20% compared with that of the nominal $p_{\mathrm{T}}^{\mathrm{miss}}$ trigger. Figure 17 (right) shows the performance of different unprescaled thresholds on online $p_{\mathrm{T}}^{\mathrm{miss}}$ against offline-corrected $p_{\mathrm{T}}^{\mathrm{miss}}$, again using 2018 data. The turn-on curves are observed to behave consistently with increasing thresholds.

The event selection efficiencies as a function of N_{vtx} are shown in figure 18 for different data-taking years. The offline thresholds are chosen at the fixed L1+HLT efficiency values of 80 and 95% for each year, as determined from figure 16. The thresholds applied online are 170, 250, and 220 GeV

2024 JINST 19 P11021

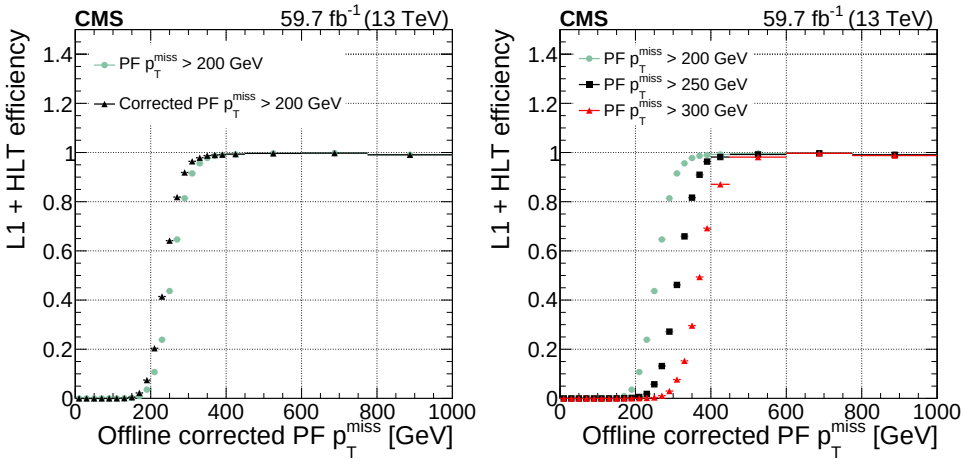

Figure 17. Left: comparison of the L1+HLT efficiencies of the corrected vs. nominal $p_{\mathrm{T}}^{\mathrm{miss}}$ triggers of the same threshold, for the data collected during 2018. Right: nominal $p_{\mathrm{T}}^{\mathrm{miss}}$ trigger L1+HLT efficiencies using different thresholds.

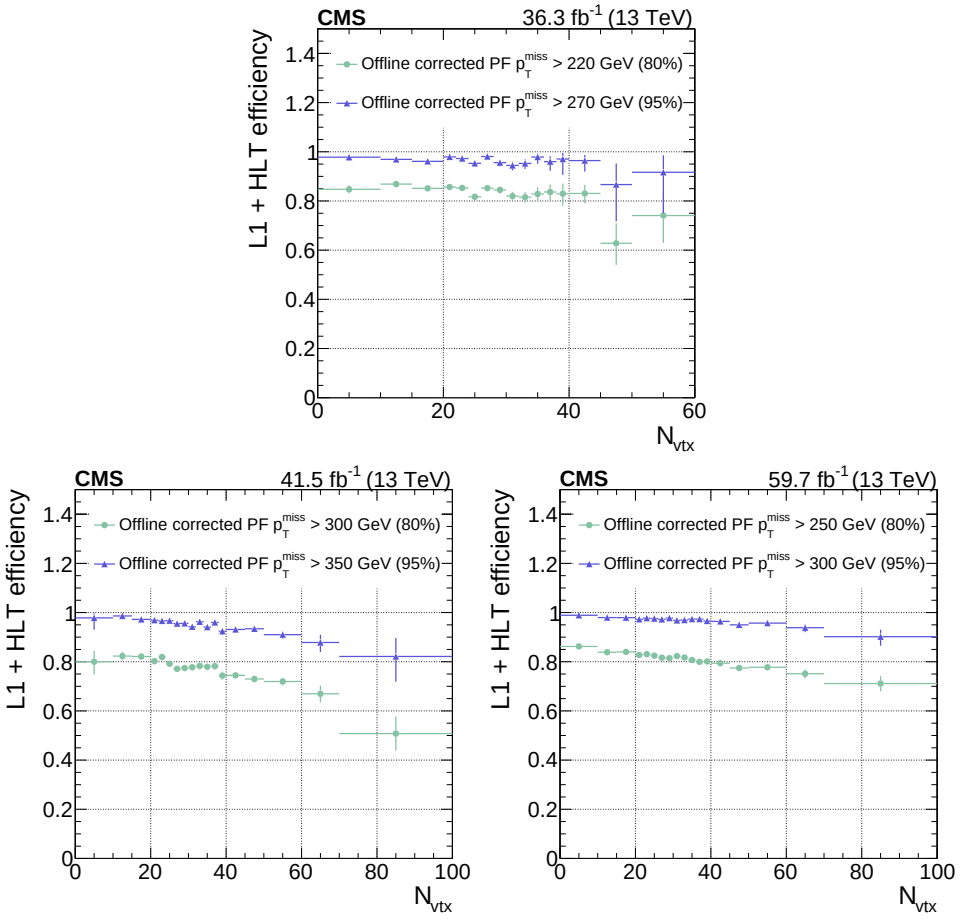

Figure 18. Event selection efficiencies as a function of N_{vtx} for fixed L1+HLT efficiency values of 80 and 95% of the unprescaled $p_{\mathrm{T}}^{\mathrm{miss}}$ triggers with the lowest $p_{\mathrm{T}}^{\mathrm{miss}}$ thresholds in 2016 (upper), 2017 (lower left), and 2018 (lower right). The PU is considerably lower in 2016, which allowed to lower thresholds for all triggers involving jets and $p_{\mathrm{T}}^{\mathrm{miss}}$. The vertical bars on the markers represent statistical uncertainties.

2024 JINST 19 P11021

in 2016, 2017, and 2018, respectively. The efficiencies decrease in events with a larger N_{vtx}, which is expected since particle tracks from only a limited number of vertices are reconstructed at the HLT and $p_{\text{T}}^{\text{miss}}$ is underestimated.

An alternative $p_{\text{T}}^{\text{miss}}$ trigger is based on a calculation that uses all the reconstructed PF objects except for muons, leading to the "μ-subtracted" trigger paths. Therefore, in this approach, events with high-p_{T} muons are also assigned large online $p_{\text{T}}^{\text{miss}}$, whereas for events with no reconstructed muons, the two calculations coincide. An unprescaled trigger path that selects μ-subtracted $p_{\text{T}}^{\text{miss}}$ and missing H_{T} (similarly without muons) both >120 GeV was available during the majority of Run 2. The main uses for this path are searches for new physics in final states with only jets and $p_{\text{T}}^{\text{miss}}$, which require the lowest $p_{\text{T}}^{\text{miss}}$ thresholds possible. Figure 19 shows the performance of this path with respect to the offline μ-subtracted $p_{\text{T}}^{\text{miss}}$, during 2016, 2017, and 2018. A trigger efficiency above 95% is reached for μ-subtracted $p_{\text{T}}^{\text{miss}} > 250$ GeV.

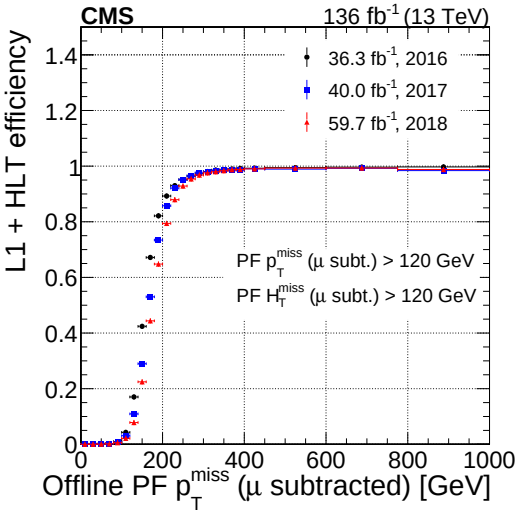

Figure 19. The L1+HLT efficiency of the μ-subtracted $p_{\text{T}}^{\text{miss}}$ trigger with a threshold of 120 GeV on both $p_{\text{T}}^{\text{miss}}$ and missing H_{T} measured with respect to the offline reconstructed μ-subtracted $p_{\text{T}}^{\text{miss}}$, shown separately for data collected during 2016, 2017, and 2018. The vertical bars on the markers represent statistical uncertainties.

4.7 b quark jets

The identification of b quark jets at the trigger level is essential to collect events that do not pass standard lepton, jet, or $p_{\text{T}}^{\text{miss}}$ triggers, and to increase the purity of the recorded sample for analyses requiring b quark jets in the final state. The L1 trigger uses information from the calorimeters and muon detectors to reconstruct objects, such as charged leptons and jets. Sophisticated identification of b quark jets similar to the one performed offline is not possible at that stage as it relies on the reconstructed tracks from charged particles available only at the HLT. In this section, we describe b quark jet identification at the HLT.

Because of latency constraints at the HLT, it is not feasible to reconstruct the tracks and primary vertex with the algorithms used for offline reconstruction. The time needed for track finding can be significantly reduced if the position of the primary vertex is known. Although the position in the transverse plane is defined with a precision of 20 μm, its position along the beam line is not known. However, it is possible to obtain a rough estimate of the primary vertex position along

2024 JINST 19 P11021

the beam line by projecting the position of the silicon pixel tracker hits compatible with the jets onto the z direction. A pixel tracker hit in the barrel (endcap) is compatible with a jet when the difference in ϕ between the hit and the jet is less than 0.21 (0.14). The region along the beam line with the highest number of projected pixel detector hits is most likely to correspond to the position of the primary vertex.

This fast primary vertex finding algorithm is sensitive to pixel detector hits from PU interactions. Therefore, a number of selection requirements based on the shape of the charge deposition clusters associated with the pixel detector hits are applied to select those that most likely correspond to a particle with a large p_T. In addition, only pixel detector hits compatible with up to four highest-p_T jets with $p_T > 30\,\text{GeV}$ and $|\eta| < 2.4$ are used. Finally, each pixel detector hit is assigned a weight reflecting the probability that it corresponds to a track in one of the considered jets. The weight is obtained by using information related to the shape of the charge deposition cluster, the ϕ between the jet and the cluster, and the jet p_T. Since the spread of projected hits from the primary vertex is proportional to the distance from the beam line, a larger weight is assigned to pixel detector hits closer to the beam line.

Since b tagging relies on the precise measurement of the displaced tracks with respect to the primary vertex, it is crucial to use tracks that use the information of both the pixel and the silicon strip tracker to improve the spatial and momentum resolutions. To reduce the HLT algorithm processing time, these tracks are reconstructed only when originating near the primary vertex and if they are close to the direction of the highest-p_T jets, sorted according to decreasing jet p_T. Up to eight jets with $p_T > 30\,\text{GeV}$ and $|\eta| < 2.4$ are considered in an event. In the first step, the trajectories of charged particles are reconstructed from the pixel detector hits. To reduce the reconstruction time, tracks are only reconstructed when they have $d_{xy} < 15\,\text{mm}$, $d_z < 2\,\text{mm}$, and are compatible in angle with the direction of one of the jets. The tracks are reconstructed using the information from the pixel and strip detectors. An iterative procedure is applied that is similar to the offline track reconstruction except for the number of iterations and the seeds used for track finding in each iteration.

The reconstructed tracks and the primary vertex are then used to reconstruct secondary vertices with the inclusive vertex finder reconstruction algorithm [33, 34]. These vertices and tracks are then used as input for the b tagging algorithms.

Usually a loose b tagging selection based on Calo-jets is used as an intermediate filter to select the events for which the full PF-jet reconstruction will be executed and from which the final PF-jet b tagging selection is applied. However, Calo-jet b tagging was sufficient for some physics triggers.

4.7.1 Description of the algorithm

During the 2016 data-taking period, CSVv2 was the recommended algorithm for b tagging at the HLT. The tagger and its performance are described in ref. [34]. After 2016, CMS developed a new tagger dedicated to identification of b quark jets reconstructed with the anti-k_T jet clustering algorithm with a distance parameter equal to 0.4 (AK4-jets). This new algorithm, DeepCSV [34], relies on a multiclassifier neural network structure made of four fully connected layers with 100 neurons each. The input variables list comprises PF jet properties, tracks, and vertex related variables. The DeepCSV output values range from zero to one and are interpreted as the probability for a given jet to originate from the hadronization of a b quark, a c quark, or a gluon or light quark. The DeepCSV tagger was deployed at the HLT at the start of the 2017 data-taking period, and it was the recommended

2024 JINST 19 P11021

online b tagging algorithm until the end of Run 2 in 2018. The training of the DeepCSV algorithm has been carried out using the input variable collections obtained from MC simulated events after the trigger selection and the full CMS event reconstruction.

An important figure of merit for b tagging algorithms is the b quark jet identification efficiency versus the gluon or light-quark jet misidentification rate evaluated in simulated events in the form of receiver operating characteristic curves (ROC curves); this provides a direct comparison of the performance of different taggers. The flavor of offline-reconstructed jets in simulation is identified using the so-called "ghost-matching" technique [32]. In this method, only the directional information of the four-momentum of the generator-level (ghost) hadron is used to prevent any modification to the four-momentum of the reconstructed jet. Jets containing at least one b hadron are assigned b quark jets. Similarly, labels are defined for jets originating from c hadrons and from gluons g or light-flavor (u, d, s) quarks (light jets). Preference is given to jets with b hadrons over c hadrons. Online jets are matched to offline jets if their direction agrees within a cone of $\Delta R < 0.4$, and their flavor is assigned using the offline jet.

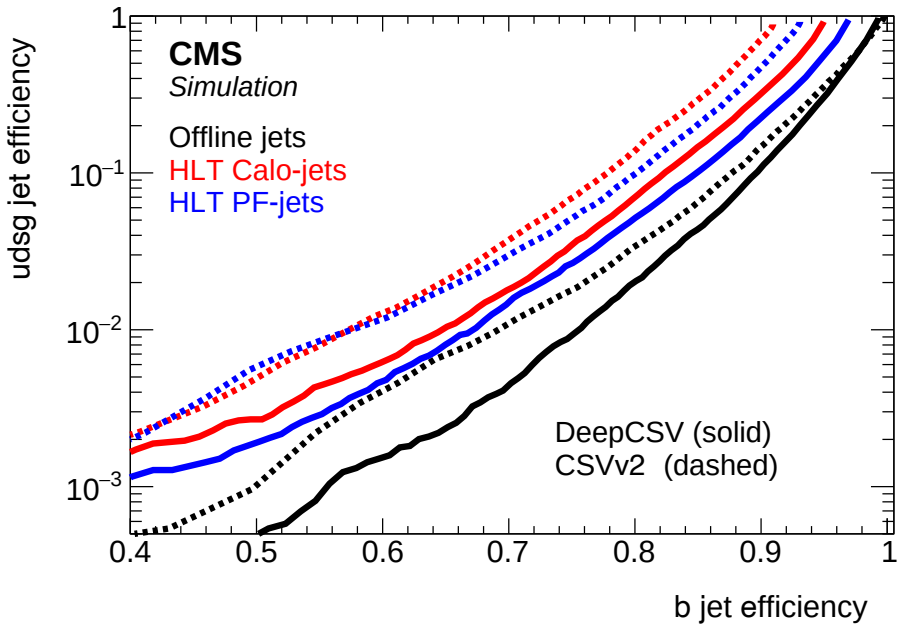

Figure 20. Performance of the online (red and blue) and offline (black) b quark jet identification algorithms demonstrated as the probability for a light jet to be misidentified as a b quark jet as a function of the efficiency to correctly identify a b quark jet. The performance of the CSVv2 (dashed) and DeepCSV (solid) algorithms are shown. The curves are obtained for online and offline jets with $p_T > 30$ GeV and $|\eta| < 2.4$ in simulated $t\bar{t}$ events. The plot is obtained using the 2017 detector conditions.

In figure 20, the ROC curves obtained for the two b tagging algorithms, DeepCSV and CSVv2, are compared using two different sets of HLT input variables for the jet algorithm: full event PF reconstruction (in blue) and reconstruction based on information in regions around jets from the CMS calorimeters (in red); the offline performance is shown for reference in black. The conclusion of this study is that DeepCSV outperforms CSVv2, with an improvement of the b quark jet tagging efficiency for a fixed gluon or light-quark misidentification rate of 5–15%.

2024 JINST 19 P11021

4.7.2 Performance measurement in data and simulation

The performance is evaluated using pp collision data collected at $\sqrt{s} = 13\,\text{TeV}$ in 2017 and 2018 during LHC Run 2, corresponding to an integrated luminosity of about 30 and 48 fb^{-1}, respectively. The performance is assessed for events consistent with the $\bar{\text{t}}\text{t}$ process. Events are selected at the HLT using a combination of trigger paths that require the presence of at least one muon and one electron. For the offline analysis, events are selected that contain one isolated electron with $p_{\text{T}} > 30\,\text{GeV}$ and one isolated muon with $p_{\text{T}} > 20\,\text{GeV}$. In addition, at least two jets with $p_{\text{T}} > 30\,\text{GeV}$ are required. This event selection is enriched with $\bar{\text{t}}\text{t}$ events and ensures an unbiased selection of b quark jets with only a small contribution of tW events.

Efficiencies are measured by selecting events that contain at least one offline-reconstructed jet passing a working point that corresponds to a light jet mistag rate of 1%. Figure 21 shows the online PF-jet DeepCSV and CSVv2 discriminator score. The left (right) plot was obtained using 2017 (2018) data. As described earlier, the output scores range from 0 to 1, and a negative value is assigned if the tracking preselection has failed and the discriminator was not evaluated. For both tagging algorithms, the data agree well with the MC simulation predictions. The distribution for true b quark jets peaks at unity, while a peak at low values in the b tag score is observed for light jets. For DeepCSV, the separation between signal and background is observed to be much larger.

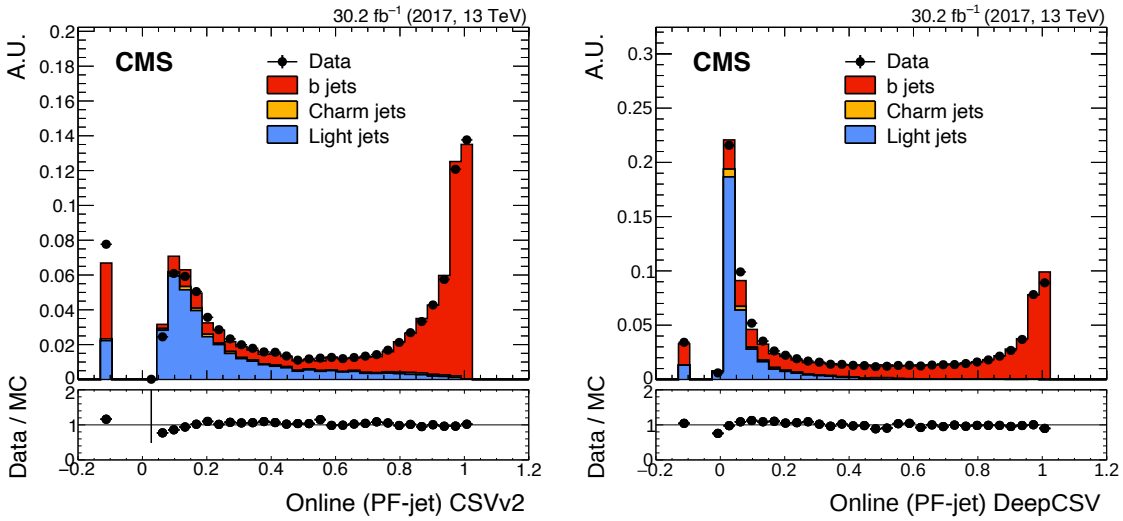

Figure 21. Left: online (PF-Jets) CSVv2 discriminator distribution, normalized to unity for both data and the summed simulation. Different colors show the contributions from simulation of different jet flavors. The plot is obtained using the 2017 detector conditions. A negative value indicates that the tracking preselection has failed and the discriminator is not evaluated. Right: same, but for the DeepCSV discriminator. The plot is obtained using 2017 data and MC simulation using the DeepCSV algorithm as it was run in 2018. The lower panel of each plot shows the ratio of data to MC simulation. The vertical bars on the markers represent statistical uncertainties.

The efficiencies at the HLT are displayed in figure 22. The efficiency is defined as the fraction of jets selected by the HLT with respect to the number of jets selected by the offline DeepCSV algorithm, with representative working points as indicated in the plots. The study is performed using data and simulated samples for the conditions of 2017. The performances of Calo- and PF-jets are shown

2024 JINST 19 P11021

individually. Good agreement between data and simulation is observed. The rise of the efficiency using DeepCSV both online and offline is much steeper because of the larger correlation between the scores. In these plots, the choice of a looser working point, and thus higher efficiency, for Calo-jet b tagging compared to PF-jet b tagging reflects how these algorithms are applied in physics triggers.

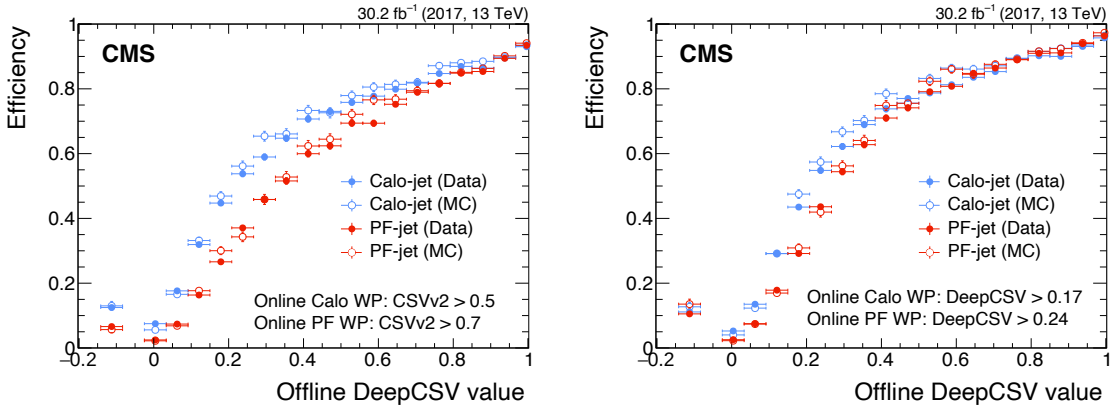

Figure 22. Efficiency to pass the online CSVv2 (left) and DeepCSV (right) working points as a function of the corresponding offline DeepCSV value. Data collected in 2017 are shown in closed circles; the result of the simulation is shown in open circles. The turn-on with respect to the online Calo-jets is shown in blue. The turn-on with respect to the online PF-jets is shown in red. The right plot is obtained using 2017 data and MC simulation using the DeepCSV algorithm as it was run in 2018. A negative value indicates that the tracking preselection has failed and the discriminator is not evaluated. The vertical bars on the markers represent statistical uncertainties.

For trigger paths using b quark jet tagging, the online efficiency with respect to the offline performance is usually an important figure of merit. This quantity can be evaluated for a fixed offline b tagging efficiency corresponding to a light-jet efficiency of 0.1, 1, or 10%, namely, the tight, medium, and loose working points, respectively. The relative CSVv2 and DeepCSV efficiency is shown in figure 23. The efficiencies, as obtained from data and simulation, are in good agreement. Using these curves, the online selection is tuned to reach a fixed efficiency given a fixed offline selection. The CSVv2 efficiency is smaller than that of DeepCSV at high score values because the offline DeepCSV discrimination is much better and the jets selected online are all also selected by the offline algorithm.

4.8 Tau leptons

Tau leptons have a relatively short lifetime and decay before reaching the beampipe. In 64.8% of cases, they decay hadronically into one or three charged hadrons and mostly accompanied by neutral pions. Neutral pions decay promptly into two photons, which may convert into e^+e^- pairs while traversing the material of the tracker. As a result of the large magnetic field of the CMS solenoid, the e^+e^- pairs are separated in the (ϕ, η) plane. Thus, neutral pions are reconstructed from photons and electrons. The aim of the HLT tau reconstruction is to reconstruct hadronic decays of tau leptons (τ_h).

4.8.1 Reconstruction of τ_h trigger paths

The reconstruction of tau leptons at the HLT is performed in different steps depending on the associated particle. A flow chart of the reconstruction steps is summarized in figure 24. The τ_h triggers used in the Run 2 data-taking period and the corresponding L1 and HLT conditions are listed in table 4.

2024 JINST 19 P11021

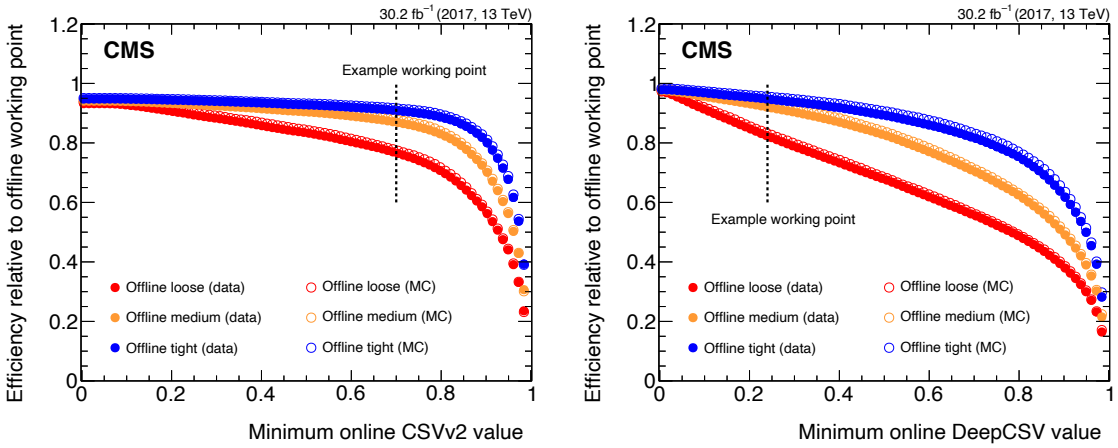

Figure 23. Efficiency of jets b tagged offline to pass the online CSVv2 (left) and DeepCSV (right) b tagging requirement, as a function of the online requirement. Three offline selections are shown: Loose (red), Medium (orange), and Tight (blue). Data are shown in closed circles; the result of the simulation is shown in open circles. The right plot is obtained using 2017 data and MC simulation but using the DeepCSV algorithm as it was run in 2018.

Double-tau ($\tau_h\tau_h$) trigger paths. A double-tau trigger path is formed when a tau lepton is associated with another tau lepton that also decays hadronically. In these double-tau triggers, the reconstruction is performed in three steps. The first step is called L2, where reconstruction starts with the L1 trigger τ_h candidates. The energy depositions in the calorimeter towers around the seeded L1 τ_h candidates within a cone of radius 0.8 are clustered, and L2 τ_h candidates are reconstructed by using the anti-k_T algorithm [32] with $\Delta R = 0.2$. In 2016 and 2017, the L2 candidates were reconstructed for all L1 τ_h candidates, including those with very low p_T that did not contribute to any of the relevant seeds in the L1 menu. In 2018, the reconstruction of the L2 candidates was updated to be performed around only those L1 τ_h candidates that satisfy the p_T and isolation criteria of the L1 seeds that contributed to the event selection at L1.

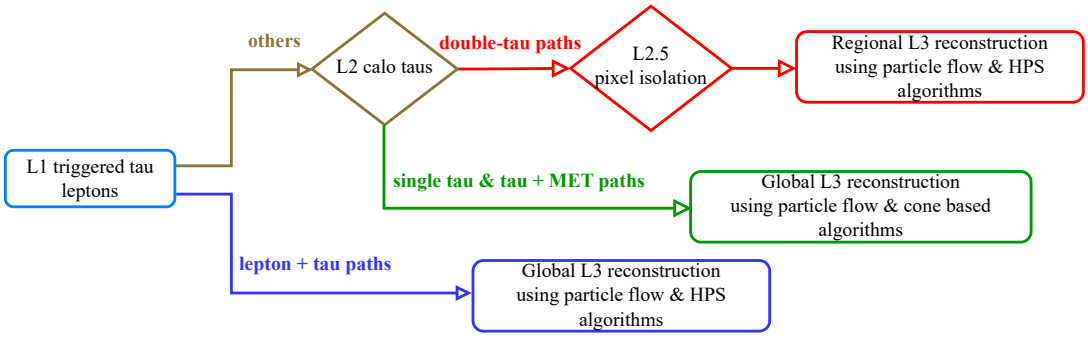

Figure 24. Flow chart for τ_h-candidate reconstruction at the HLT.

In the second step, known as L2.5, charged-particle isolation based on the information in the pixel detector is implemented. Reconstructed L2 τ_h jets with $p_T > 20$ GeV and $|\eta| < 2.5$ are selected, and pixel detector tracks are reconstructed around the direction of the selected L2 τ_h candidates in a region of $\Delta\eta \times \Delta\phi = 0.5 \times 0.5$ from the hits in the pixel detector. The reconstructed tracks are

2024 JINST 19 P11021

clustered, and vertices having at least two tracks with $p_T > 1$ GeV are formed by using the divisive vertex finder [8]. If no vertices are found, a τ_h candidate is considered perfectly isolated and the reconstruction continues with the next step. If more than one vertex is reconstructed, the one with the highest $\sum p_T^2$ of its constituent tracks is chosen as the primary vertex of the hard-scattering event. Tracks that have at least three hits and have a trajectory in a cone of $0.15 < \Delta R < 0.4$ centered around the L2 τ_h candidates and originating from the primary vertex are considered for the isolation requirement. These tracks are required to have $d_{xy} < 0.2$ cm. An L2 τ_h candidate is considered to be isolated if the scalar sum of the p_T of the associated pixel detector tracks is less than 4.5 GeV.

The final step is referred to as the L3 reconstruction, where the full tracking information is included through the use of the online PF reconstruction. Instead of reconstructing all tracks, the reconstruction is performed regionally around the L2 τ_h candidates with $p_T > 20$ GeV and $|\eta| < 2.5$. The L3 reconstruction was performed using a cone-based algorithm until mid-2018, after which it was upgraded to the hadron-plus-strips (HPS) algorithm that had already been in use for the offline reconstruction of tau leptons [35]. The HPS algorithm allows for the exclusive reconstruction of specific hadronic decay modes, which is not possible with a cone-based algorithm. Both algorithms start with PF jets reconstructed by the anti-k_T algorithm with a distance parameter of 0.4, and a maximum of one tau lepton is reconstructed for each PF jet at the end of the algorithm. The HPS-based algorithm, described later, will be the main focus here, since the cone-based algorithm has already been described in ref. [35].

The $\tau_h\tau_h$ triggers used in the Run 2 data-taking period require a pair of isolated L1 τ_h candidates with variable p_T thresholds, as listed in table 4. The τ_h candidates are required to have $p_T > 35$ GeV at the HLT and to pass the medium working point of the combined isolation, described below. The isolation is relaxed by 5%/GeV for $p_T^{\tau_h} > 100$ GeV (i.e., the threshold on the p_T sum is increased by 5% for each GeV in $p_T^{\tau_h}$ above 100 GeV). The τ_h candidates must be separated by $\Delta R > 0.5$.

Lepton+τ_h trigger paths. So-called cross triggers select events with at least one tau lepton and another object, such as an electron or muon. For these triggers, the reconstruction is performed in fewer steps than for double-tau trigger paths. These triggers require the existence of an L1 trigger seeded by a muon or an electron together with a τ_h lepton. Additionally, they perform the reconstruction and selection of a muon or electron before the τ_h reconstruction starts, which reduces the number of events for which the τ_h reconstruction is run. Because of that, the L3 reconstruction is run directly without the L2 and L2.5 prefilters and thus over the entire CMS detector acceptance. The L3 reconstruction is performed using the HPS algorithm.

The lepton+τ_h triggers require a muon or an electromagnetic object passing the L1 p_T thresholds given in table 4. A τ_h candidate is also required to pass a given HLT p_T threshold and loose charged isolation. In some cases, several L1 triggers with different p_T thresholds are used to keep the L1 rate constant by dynamically selecting the unprescaled L1 seed based on $\mathcal{L}_{inst}$. The isolation is relaxed by 5%/GeV for $p_T^{\tau_h} > 110$ GeV. Finally, the lepton and τ_h candidate must be separated from each other by requiring $\Delta R > 0.3$.

The $\tau_h + p_T^{miss}$ and single-τ_h trigger paths. Tau leptons can also be reconstructed in association with p_T^{miss}, which is also called a cross trigger. The reconstruction in such triggers occurs in two steps. These triggers require the existence of an L1 trigger seeded by p_T^{miss} together with a τ_h lepton, as with the lepton+τ_h triggers. The reconstruction and selection of p_T^{miss} before the τ_h reconstruction is started reduces the rate of events for which the τ_h reconstruction is run. Hence, the L3 reconstruction

2024 JINST 19 P11021

can be run without the L2.5 prefilter and globally over the entire coverage of the CMS detector. In the case of single-τ_h triggers, because of the high p_T requirement, global L3 reconstruction is also affordable. In both $\tau_h + p_T^{miss}$ and single-τ_h triggers, however, the L2 filters are used to reduce the CPU processing time. In contrast to the $\mu\tau_h$, $e\tau_h$, and $\tau_h\tau_h$ triggers, the $\tau_h + p_T^{miss}$ and single-τ_h triggers reconstruct the tau leptons using the cone-based algorithm as described in ref. [35].

Table 4. List of τ_h triggers used in 2016, 2017, and 2018 data-taking periods including both the L1 and HLT conditions. The $e\tau_h$ triggers evolved in 2016 data taking, with the labels (1), (2), and (3) indicating use for the first 7.4 fb^{-1}, the next 10.2 fb^{-1}, and the last 18.3 fb^{-1} of data, respectively.

Year	Trigger	HLT condition	L1 condition
2016			
	$\mu\tau_h$	$p_T^{\mu} > 19$ GeV (isolated) $p_T^{\tau_h} > 20$ GeV (unseeded)	$p_T^{\mu} > 18$ GeV
	$e\tau_h$	$p_T^{e} > 24$ GeV, $p_T^{\tau_h} > 20$ GeV (unseeded) (1)	$p_T^{e} > 22$ GeV
		$p_T^{e} > 24$ GeV, $p_T^{\tau_h} > 20$ GeV (seeded & nonisolated) (2)	$p_T^{e} > 22$ GeV, $p_T^{\tau_h} > 20$ GeV
		$p_T^{e} > 24$ GeV, $p_T^{\tau_h} > 30$ GeV (seeded & isolated) (3)	$p_T^{e} > 22$ GeV, $p_T^{\tau_h} > 26$ GeV
	$\tau_h\tau_h$	$p_T^{\tau_h} > 35$ GeV (seeded & isolated)	$p_T^{\tau_h} > 28$–36 GeV
	$\tau_h + p_T^{miss}$	$p_T^{miss} > 90$ GeV, $p_T^{\tau_h} > 50$ GeV, $p_T^{h^{\pm}} > 30$ GeV (unseeded)	$p_T^{miss} > 80$–100 GeV
	Single τ_h	$p_T^{\tau_h} > 140$ GeV, $p_T^{h^{\pm}} > 50$ GeV (seeded)	$p_T^{\tau_h} > 120$ GeV
2017 & 2018			
	$\mu\tau_h$	$p_T^{\mu} > 20$ GeV (isolated), $p_T^{\tau_h} > 27$ GeV (seeded & nonisolated)	$p_T^{\mu} > 18$ GeV, $p_T^{\tau_h} > 24/26$ GeV
	$e\tau_h$	$p_T^{e} > 24$ GeV , $p_T^{\tau_h} > 30$ GeV (seeded & isolated)	$p_T^{e} > 22/24$ GeV, $p_T^{\tau_h} > 26/27$ GeV
	$\tau_h\tau_h$	$p_T^{\tau_h} > 35$ GeV (seeded & isolated)	$p_T^{\tau_h} > 32$–36 GeV
	$\tau_h + p_T^{miss}$	$p_T^{miss} > 100$ GeV, $p_T^{\tau_h} > 50$ GeV, $p_T^{h^{\pm}} > 30$ GeV (seeded)	$p_T^{miss} > 80$–110 GeV, $p_T^{\tau_h} > 40$ GeV
	Single τ_h	$p_T^{\tau_h} > 180$ GeV, $p_T^{h^{\pm}} > 50$ GeV (seeded)	$p_T^{\tau_h} > 120$–130 GeV

The $\tau_h + p_T^{miss}$ triggers are seeded by an L1 cross trigger as listed in table 4. The $\tau_h + p_T^{miss}$ triggers require high p_T^{miss} and a tau lepton with $p_T^{\tau_h} > 50$ GeV passing the medium working point of the charged isolation by rejecting the tracks with low p_T. The isolation is relaxed by 5%/GeV for $p_T^{\tau_h} > 120$ GeV. The high p_T single-τ_h trigger is seeded by a single L1 tau lepton. Tau leptons are reconstructed by using charged particle $h^{\pm}$ tracks with $p_T^{h^{\pm}} > 30\,(50)$ GeV for the $\tau_h + p_T^{miss}$ (single-τ_h) trigger, and they are required to have large p_T and to pass the medium working point of the combined isolation (discussed in the next section). The isolation is relaxed for $p_T^{\tau_h} > 300$ GeV by 2%/GeV and is removed completely when $p_T^{\tau_h} > 500$ GeV.

Hadron-plus-strips algorithm. In the first step of the HPS algorithm, photons and electrons that exist in PF jets are clustered into a "strip" around the highest-p_T photon or electron with a $\Delta\eta \times \Delta\phi$ area of 0.05×0.2, and the strip is assigned the π^0 mass. To overcome any inefficiency stemming from the misreconstruction of charged hadrons, PF neutral hadrons in the signal cone are

2024 JINST 19 P11021

considered as a part of charged hadrons in addition to PF charged hadrons. The signal cone that is used to reconstruct τ_h candidates is defined as a function of the p_T of the hadronic system by $R_{sig} = 3.0\,\text{GeV}/p_T$, with the limits of the cone size to be in the range of $0.05 < R_{sig} < 0.10$. We reconstruct τ_h candidates in the following decay topology classes on the number of charged and neutral hadrons: $(n_{h^\pm}, n_{\pi^0})$ = (1,0), (1,1), (1,2), (2,0), (2,1), (3,0), and (3,1). The classes with two charged hadrons have been added to catch decays to three charged hadrons where one track was not properly reconstructed. A vertex is associated to each tau candidate, selected to be the one closest in d_z, to the track of the highest-p_T charged-hadron candidate. A tau lepton is then selected by applying further requirements that include the compatibility of the final states to given decay modes. For this purpose, the reconstructed decay modes are required to be within a mass window corresponding to either a $\rho(770)$ or $a_1(1260)$. The mass windows are optimized for the online implementation of the HPS algorithm to reconstruct the online tau leptons efficiently. The offline values of the mass windows are reported in ref. [35].

After this step, there are further cleaning steps applied. Soft tau lepton candidates with two charged hadrons with $p_T < 5\,\text{GeV}$ are rejected in order to reduce the rate of tau leptons with one charged hadron migrating to the decay mode with two charged hadrons. Of the remaining candidates, the tau leptons with the largest p_T and largest strip multiplicity are preferred by the HLT paths. The single-tau candidate with the lowest combined isolation, associating its neutral components with the candidate, within the isolation cone size of $\Delta R = 0.5$, is selected. The combined isolation is calculated as:

$$I^{L3}_{\tau_h} = \sum p_T^{\text{charged}} + \sum p_T^{\gamma}, \tag{4.1}$$

where $\sum p_T^{\text{charged}}$ and $\sum p_T^{\gamma}$ are the scalar sums of the p_T of charged hadrons and of photons, respectively, that do not belong to the τ_h candidate. The value of the combined isolation is relaxed in the HPS-based tau lepton reconstruction compared with the one used in cone-based algorithm to achieve similar efficiency, leading to the requirement that the isolation be smaller than 3.9, 3.7, and 3.2 GeV for loose, medium, and tight working points, respectively. Those values are further relaxed as a function of p_T to increase the reconstruction efficiency of genuine τ_h candidates at high p_T. This is only possible because of the reduction in the number of misidentified τ_h candidates as a function of p_T, which helps to control the trigger rates [35].

4.8.2 Performance measurement in data and simulation

The efficiencies of the τ_h legs of the $e\tau_h$, $\mu\tau_h$, and $\tau_h\tau_h$ triggers are estimated by using the tag-and-probe method in $Z/\gamma^* \to \tau\tau \to \mu\tau_h$ events, since the τ_h purity is higher in $\mu\tau_h$ events than in $e\tau_h$ and $\tau_h\tau_h$ events. Monitoring triggers based on $\mu\tau_h$ with the same isolation, identification, and p_T thresholds as in the $e\tau_h$ or $\tau_h\tau_h$ triggers are used to measure the efficiency of τ_h leg in $e\tau_h$ and $\tau_h\tau_h$ triggers. The trigger efficiency is calculated from the ratio of the number of events that pass the baseline offline tag-and-probe selection, explained below, as well as the given HLT path to the number of events that pass only the tag-and-probe selection. The offline τ_h candidates are matched to the online τ_h candidates for the numerator selection. The measured efficiencies always depend on the offline selection.

Events passing an isolated single-muon L1 trigger with $p_T > 27\,\text{GeV}$ and $|\eta| < 2.1$ are selected. Exactly one offline muon passing loose identification criteria is required to suppress the contamination from $Z \to \mu\mu$ events. An offline muon candidate is considered matched with an online object if

2024 JINST 19 P11021

$\Delta R < 0.5$. From this sample, a hadronically decaying tau candidate with $p_T > 20\,\text{GeV}$ and $|\eta| < 2.1$ is selected as the probe. The tau candidate is required to pass the medium working point of the tau combined isolation to reject the events with misidentified tau leptons reconstructed from the background from SM events composed uniquely of jets produced through the strong interaction, referred to as quantum chromodynamics multijet events, with 70% efficiency. To suppress the misidentified muons and electrons, dedicated discriminators are used. The τ_h lepton is required to be separated from the tagged μ. The selected μ and τ_h candidates are required to have opposite sign charges in both data and simulation samples. The reconstructed offline tau leptons are matched with tau leptons, electrons, or muons at the MC generator level to suppress misidentified τ_h particles from jets in simulated events. In data, the contribution from such events is subtracted using events containing a muon and an hadronic tau lepton carrying the same charge. To increase the purity of the $Z \to \tau\tau \to \mu\tau_h$ events, offline selections on the transverse mass, $m_T(\mu, p_T^{miss}) < 30\,\text{GeV}$, and visible mass, $40 < m_{vis}(\mu\tau_h) < 80\,\text{GeV}$ are applied. Furthermore, events with electrons and b-tagged jets are vetoed.

The trigger efficiencies are measured for the full 2016, 2017, and 2018 data sets, corresponding to an integrated luminosity of $137.1\,\text{fb}^{-1}$, and in Drell-Yan simulated samples ($Z/\gamma^* \to \ell\ell$, where $\ell = e, \mu, \tau$). The combined L1+HLT efficiency of the τ_h triggers is presented unless stated otherwise. Therefore, generally, the results include the impact of L1 trigger selection efficiency and the specific L1 seeding efficiencies. Figure 25 compares the p_T resolution of the two different algorithms used to reconstruct hadronically decaying tau leptons from the same data set recorded from the first $17.7\,\text{fb}^{-1}$ taken in 2018. The figure shows that the HPS-based tau reconstruction has a better p_T resolution compared with the cone-based one. This reduces the fraction of misidentified τ_h candidates from low-p_T jets exceeding the nominal p_T threshold, allowing lower p_T thresholds for the same rate. The efficiency per leg of these two algorithms is presented in figure 26 for the $\tau_h\tau_h$ triggers, where one can see that the HPS algorithm has slightly higher efficiency in the turn-on region with p_T and has a significant improvement in the region of high PU.

The implementation of the HPS τ_h reconstruction reduced the HLT rate of τ_h by 10% per τ_h leg. It is measured as 4.6 and 39 Hz for an average PU of approximately 50 for $\mu\tau_h$ and $\tau_h\tau_h$ triggers, respectively, while it was correspondingly 5.2 and 50 Hz for the cone-based algorithm. The approximate processing time of a $\tau_h\tau_h$ trigger is around 50 ms, whereas it is around 10 ms for lepton+τ_h triggers for an average PU of approximately 50.

Figure 27 presents the trigger performance per leg of the $\tau_h\tau_h$ triggers in 2016, 2017, and 2018. It shows that the 2016 data have a higher efficiency compared with 2017 and 2018 data, which is a consequence of the lower L1 p_T thresholds and the lower PU, as presented in the right plot of the figure. The HPS-based reconstruction algorithm deployed in the middle of 2018 data-taking results in good efficiency in general, compared with the cone-based reconstruction algorithm that was used before. Since there were no other significant differences in terms of p_T thresholds, isolation, or L1 seeds between 2017 and 2018, one would expect to see similar performance in 2017 and 2018. However, the figure shows that the efficiency for 2017 data is lower than that in 2018 data. This was caused by the inactive pixel detector modules observed in the beginning of 2017 data taking as well as the DC-DC converter issue (described in section 4.1) encountered at the end of the 2017 data taking. The inefficiency coming from the inactive pixel detector modules was recovered with the extra recovery iterations in the tracking, but the DC-DC problem reduced the overall efficiency. In 2018, the DC-DC pixel detector issue was mitigated, and this improved the tau trigger efficiency.

2024 JINST 19 P11021

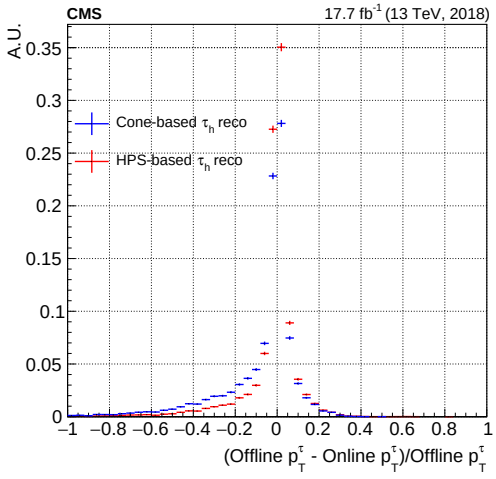

Figure 25. The p_{T} resolution for the $\mu\tau_{\mathrm{h}}$ trigger for cone-based and HPS-based τ_{h} reconstruction, calculated by using the first 17.7 fb^{-1} of 2018 data taken with the cone-based tau reconstruction, where the trigger paths with HPS-based algorithm were included for the purpose of testing. The vertical bars on the markers represent statistical uncertainties.

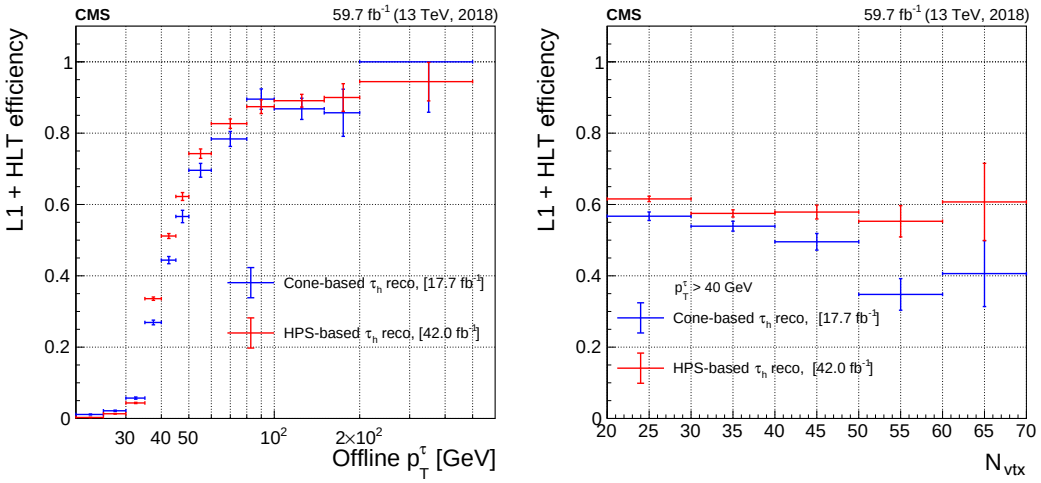

Figure 26. Combined L1 and HLT efficiency per leg of the $\tau_{\mathrm{h}}\tau_{\mathrm{h}}$ triggers with cone-based and HPS-based τ_{h} reconstruction, using the first 17.7 fb^{-1} and the next 42.0 fb^{-1} of data in 2018. The figure shows the efficiency as a function of offline p_{T}^{τ} (left) and N_{vtx} (right). The vertical bars on the markers represent statistical uncertainties.

5 Summary

The performance of the high-level trigger of CMS has been presented as it evolved over the course of LHC Run 2 in 2016–2018. The algorithms of the high-level trigger were adapted to meet the challenges of the increase of the LHC luminosity and pileup to twice their initial design values as well as two to three times the previous Run 1 values. Imperfect detector effects that arose also were mitigated to minimize inefficiencies. The trigger menu continuously evolved to meet the needs of the experiment across a wide range of physics areas under these conditions and within the CPU capacity of the online computer farm. The overall single isolated lepton trigger efficiency was maintained at

2024 JINST 19 P11021

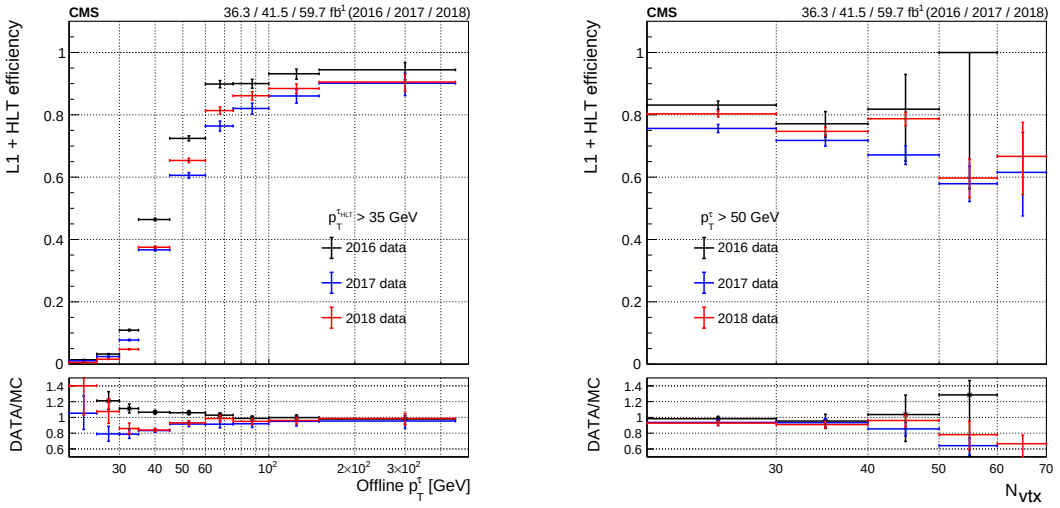

Figure 27. Combined L1 and HLT efficiency per leg of the $\tau_h\tau_h$ triggers for 2016, 2017, and 2018 data taking. The figure shows the trigger efficiency as a function of the offline p_T^τ for a 35 GeV threshold (left) and as a function of N_{vtx} (right), for which an offline requirement of $p_T^\tau > 50$ GeV is applied. The lower panels show the ratio of data to MC simulation for each year. The vertical bars on the markers represent statistical uncertainties.

the level of 90% for muons and 80% for electrons with p_T thresholds of 24 and 32 GeV, respectively. Triggers based on jets and on energy sums such as p_T^{miss} also were available. Jets also could be tagged as arising from a b quark jet with a performance of the identification algorithm approaching that achieved offline and using machine learning for the best discrimination. Hadronically decaying tau leptons were also reconstructed in the trigger and were typically used in combination with other leptons, with minimum p_T thresholds from 20 to 35 GeV on the hadronic tau decay depending on the flavor of the other lepton and the data-taking year.

Acknowledgments

We congratulate our colleagues in the CERN accelerator departments for the excellent performance of the LHC and thank the technical and administrative staffs at CERN and at other CMS institutes for their contributions to the success of the CMS effort. In addition, we gratefully acknowledge the computing centers and personnel of the Worldwide LHC Computing Grid and other centers for delivering so effectively the computing infrastructure essential to our analyses. Finally, we acknowledge the enduring support for the construction and operation of the LHC, the CMS detector, and the supporting computing infrastructure provided by the following funding agencies: SC (Armenia), BMBWF and FWF (Austria); FNRS and FWO (Belgium); CNPq, CAPES, FAPERJ, FAPERGS, and FAPESP (Brazil); MES and BNSF (Bulgaria); CERN; CAS, MoST, and NSFC (China); MINCIENCIAS (Colombia); MSES and CSF (Croatia); RIF (Cyprus); SENESCYT (Ecuador); ERC PRG, RVTT3 and MoER TK202 (Estonia); Academy of Finland, MEC, and HIP (Finland); CEA and CNRS/IN2P3 (France); SRNSF (Georgia); BMBF, DFG, and HGF (Germany); GSRI (Greece); NKFIH (Hungary); DAE and DST (India); IPM (Iran); SFI (Ireland); INFN (Italy); MSIP and NRF (Republic of Korea); MES (Latvia); LMTLT (Lithuania); MOE and UM (Malaysia); BUAP, CINVESTAV, CONACYT, LNS, SEP, and

UASLP-FAI (Mexico); MOS (Montenegro); MBIE (New Zealand); PAEC (Pakistan); MES and NSC (Poland); FCT (Portugal); MESTD (Serbia); MCIN/AEI and PCTI (Spain); MOSTR (Sri Lanka); Swiss Funding Agencies (Switzerland); MST (Taipei); MHESI and NSTDA (Thailand); TUBITAK and TENMAK (Turkey); NASU (Ukraine); STFC (United Kingdom); DOE and NSF (U.S.A.).

Individuals have received support from the Marie-Curie program and the European Research Council and Horizon 2020 Grant, contract Nos. 675440, 724704, 752730, 758316, 765710, 824093, 101115353, 101002207, and COST Action CA16108 (European Union); the Leventis Foundation; the Alfred P. Sloan Foundation; the Alexander von Humboldt Foundation; the Science Committee, project no. 22rl-037 (Armenia); the Belgian Federal Science Policy Office; the Fonds pour la Formation à la Recherche dans l'Industrie et dans l'Agriculture (FRIA-Belgium); the F.R.S.-FNRS and FWO (Belgium) under the "Excellence of Science — EOS" — be.h project n. 30820817; the Beijing Municipal Science & Technology Commission, No. Z191100007219010 and Fundamental Research Funds for the Central Universities (China); the Ministry of Education, Youth and Sports (MEYS) of the Czech Republic; the Shota Rustaveli National Science Foundation, grant FR-22-985 (Georgia); the Deutsche Forschungsgemeinschaft (DFG), among others, under Germany's Excellence Strategy — EXC 2121 "Quantum Universe" — 390833306, and under project number 400140256 - GRK2497; the Hellenic Foundation for Research and Innovation (HFRI), Project Number 2288 (Greece); the Hungarian Academy of Sciences, the New National Excellence Program - ÚNKP, the NKFIH research grants K 131991, K 133046, K 138136, K 143460, K 143477, K 146913, K 146914, K 147048, 2020-2.2.1-ED-2021-00181, and TKP2021-NKTA-64 (Hungary); the Council of Science and Industrial Research, India; ICSC — National Research Center for High Performance Computing, Big Data and Quantum Computing and FAIR — Future Artificial Intelligence Research, funded by the NextGenerationEU program (Italy); the Latvian Council of Science; the Ministry of Education and Science, project no. 2022/WK/14, and the National Science Center, contracts Opus 2021/41/B/ST2/01369 and 2021/43/B/ST2/01552 (Poland); the Fundação para a Ciência e a Tecnologia, grant CEECIND/01334/2018 (Portugal); the National Priorities Research Program by Qatar National Research Fund; MCIN/AEI/10.13039/501100011033, ERDF "a way of making Europe", and the Programa Estatal de Fomento de la Investigación Científica y Técnica de Excelencia María de Maeztu, grant MDM-2017-0765 and Programa Severo Ochoa del Principado de Asturias (Spain); the Chulalongkorn Academic into Its 2nd Century Project Advancement Project, and the National Science, Research and Innovation Fund via the Program Management Unit for Human Resources & Institutional Development, Research and Innovation, grant B39G670016 (Thailand); the Kavli Foundation; the Nvidia Corporation; the SuperMicro Corporation; the Welch Foundation, contract C-1845; and the Weston Havens Foundation (U.S.A.).

References

[1] CMS collaboration, *Enriching the Physics Program of the CMS Experiment via Data Scouting and Data Parking*, submitted to *Phys. Rept.* [arXiv:2403.16134].

[2] CMS collaboration, *The CMS trigger system*, 2017 *JINST* **12** P01020 [arXiv:1609.02366].

[3] CMS collaboration, *CMS Technical Design Report for the Level-1 Trigger Upgrade*, CERN-LHCC-2013-011 (2013).

[4] CMS collaboration, *Performance of the CMS Level-1 trigger in proton-proton collisions at* $\sqrt{s} = 13$ *TeV*, 2020 *JINST* **15** P10017 [arXiv:2006.10165].

2024 JINST 19 P11021

[5] CMS collaboration, *Technical proposal for the upgrade of the CMS detector through 2020*, CERN-LHCC-2011-006 (2011).

[6] CMS collaboration, *Development of the CMS detector for the CERN LHC Run 3*, 2024 *JINST* **19** P05064 [arXiv:2309.05466].

[7] CMS collaboration, *The CMS Experiment at the CERN LHC*, 2008 *JINST* **3** S08004.

[8] CMS collaboration, *Description and performance of track and primary-vertex reconstruction with the CMS tracker*, 2014 *JINST* **9** P10009 [arXiv:1405.6569].

[9] CMS Tracker Group collaboration, *The CMS Phase-1 Pixel Detector Upgrade*, 2021 *JINST* **16** P02027 [arXiv:2012.14304].

[10] CMS collaboration, *Track impact parameter resolution for the full pseudo rapidity coverage in the 2017 dataset with the CMS Phase-1 Pixel detector*, CMS-DP-2020-049 (2020).

[11] CMS collaboration, *2017 tracking performance plots*, CMS-DP-2017-015 (2017).

[12] P. Grafström and W. Kozanecki, *Luminosity determination at proton colliders*, *Prog. Part. Nucl. Phys.* **81** (2015) 97.

[13] R. Bruce et al., *Review of LHC Run 2 Machine Configurations*, in the proceedings of the *9th LHC Operations Evian Workshop*, Evian Les Bains, France, January 30–February 1 (2019), p. 187.

[14] J. Wenninger, *Operation and Configuration of the LHC in Run 2*, CERN-ACC-NOTE-2019-0007 (2019).

[15] D. Mirarchi et al., *Special Losses during LHC Run 2*, in the proceedings of the *9th LHC Operations Evian Workshop*, Evian Les Bains, France, January 30– February 1 (2019), p. 213.

[16] HEPiX Benchmarking Working Group, https://w3.hepix.org/benchmarking.html.

[17] C.D. Jones et al., *Using the CMS Threaded Framework In A Production Environment*, *J. Phys. Conf. Ser.* **664** (2015) 072026.

[18] CMS collaboration, *Particle-flow reconstruction and global event description with the CMS detector*, 2017 *JINST* **12** P10003 [arXiv:1706.04965].

[19] CMS collaboration, *Measurement of the Inclusive W and Z Production Cross Sections in pp Collisions at* $\sqrt{s} = 7$ *TeV*, *JHEP* **10** (2011) 132 [arXiv:1107.4789].

[20] R. Fruhwirth, *Application of Kalman filtering to track and vertex fitting*, *Nucl. Instrum. Meth. A* **262** (1987) 444.

[21] F. Pantaleo, *New Track Seeding Techniques for the CMS Experiment*, Ph.D. thesis, Hamburg University, Hamburg, Germany (2017) [CMS-TS-2017-028, CERN-THESIS-2017-242].

[22] K. Rose, *Deterministic annealing for clustering, compression, classification, regression, and related optimization problems*, *IEEE Proc.* **86** (1998) 2210.

[23] R. Frühwirth, W. Waltenberger and P. Vanlaer, *Adaptive vertex fitting*, *J. Phys. G* **34** (2007) N343.

[24] CMS collaboration, *Performance of the CMS muon trigger system in proton-proton collisions at* $\sqrt{s} = 13$ *TeV*, 2021 *JINST* **16** P07001 [arXiv:2102.04790].

[25] CMS collaboration, *Performance of Electron Reconstruction and Selection with the CMS Detector in Proton-Proton Collisions at* $\sqrt{s} = 8$ *TeV*, 2015 *JINST* **10** P06005 [arXiv:1502.02701].

[26] W. Adam, R. Frühwirth, A. Strandlie and T. Todorov, *Reconstruction of electrons with the Gaussian sum filter in the CMS tracker at LHC*, *eConf C* **0303241** (2003) TULT009 [physics/0306087].

[27] CMS collaboration, *Precision luminosity measurement in proton-proton collisions at* $\sqrt{s} = 13$ *TeV in 2015 and 2016 at CMS*, *Eur. Phys. J. C* **81** (2021) 800 [arXiv:2104.01927].

2024 JINST 19 P11021

[28] CMS collaboration, *CMS luminosity measurement for the 2017 data-taking period at* $\sqrt{s} = 13$ *TeV*, CMS-PAS-LUM-17-004, CERN, Geneva (2018).

[29] CMS collaboration, *CMS luminosity measurement for the 2018 data-taking period at* $\sqrt{s} = 13$ *TeV*, CMS-PAS-LUM-18-002, CERN, Geneva (2019).

[30] CMS collaboration, *Measurements of Inclusive W and Z Cross Sections in pp Collisions at* $\sqrt{s} = 7$ *TeV*, *JHEP* **01** (2011) 080 [arXiv:1012.2466].

[31] CMS collaboration, *Electron and photon reconstruction and identification with the CMS experiment at the CERN LHC*, 2021 *JINST* **16** P05014 [arXiv:2012.06888].

[32] M. Cacciari, G.P. Salam and G. Soyez, *The anti-*k_t *jet clustering algorithm*, *JHEP* **04** (2008) 063 [arXiv:0802.1189].

[33] CMS collaboration, *Measurement of* $B\bar{B}$ *Angular Correlations based on Secondary Vertex Reconstruction at* $\sqrt{s} = 7$ *TeV*, *JHEP* **03** (2011) 136 [arXiv:1102.3194].

[34] CMS collaboration, *Identification of heavy-flavour jets with the CMS detector in pp collisions at* 13 *TeV*, 2018 *JINST* **13** P05011 [arXiv:1712.07158].

[35] CMS collaboration, *Performance of reconstruction and identification of* τ *leptons decaying to hadrons and* ν_τ *in pp collisions at* $\sqrt{s} = 13$ *TeV*, 2018 *JINST* **13** P10005 [arXiv:1809.02816].

2024 JINST 19 P11021

The CMS collaboration

Yerevan Physics Institute, Yerevan, Armenia

A. Hayrapetyan, A. Tumasyan[1]

Institut für Hochenergiephysik, Vienna, Austria

W. Adam, J.W. Andrejkovic, L. Benato, T. Bergauer, S. Chatterjee, K. Damanakis, M. Dragicevic, P.S. Hussain, M. Jeitler[2], N. Krammer, A. Li, D. Liko, I. Mikulec, J. Schieck[2], R. Schöfbeck[2], D. Schwarz, M. Sonawane, W. Waltenberger, C.-E. Wulz[2]

Universiteit Antwerpen, Antwerpen, Belgium

T. Janssen, T. Van Laer, P. Van Mechelen

Vrije Universiteit Brussel, Brussel, Belgium

N. Breugelmans, J. D'Hondt, S. Dansana, A. De Moor, M. Delcourt, F. Heyen, S. Lowette, I. Makarenko, D. Müller, S. Tavernier, M. Tytgat[3], G.P. Van Onsem, S. Van Putte, D. Vannerom

Université Libre de Bruxelles, Bruxelles, Belgium

D. Beghin, B. Bilin, H. Brun, B. Clerbaux, A.K. Das, I. De Bruyn, G. De Lentdecker, H. Evard, L. Favart, P. Gianneios, J. Jaramillo, A. Khalilzadeh, F.A. Khan, K. Lee, A. Malara, S. Paredes, M.A. Shahzad, L. Thomas, M. Vanden Bemden, C. Vander Velde, P. Vanlaer

Ghent University, Ghent, Belgium

T. Cornelis, M. De Coen, D. Dobur, G. Gokbulut, Y. Hong, J. Knolle, L. Lambrecht, D. Marckx, K. Mota Amarilo, K. Skovpen, N. Van Den Bossche, J. van der Linden, L. Wezenbeek

Université Catholique de Louvain, Louvain-la-Neuve, Belgium

A. Benecke, A. Bethani, G. Bruno, C. Caputo, J. De Favereau De Jeneret, C. Delaere, I.S. Donertas, A. Giammanco, A.O. Guzel, Sa. Jain, V. Lemaitre, J. Lidrych, P. Mastrapasqua, T.T. Tran, S. Turkcapar

Centro Brasileiro de Pesquisas Fisicas, Rio de Janeiro, Brazil

G.A. Alves, E. Coelho, G. Correia Silva, C. Hensel, T. Menezes De Oliveira, C. Mora Herrera[4], P. Rebello Teles, M. Soeiro, E.J. Tonelli Manganote[5], A. Vilela Pereira[4]

Universidade do Estado do Rio de Janeiro, Rio de Janeiro, Brazil

W.L. Aldá Júnior, M. Barroso Ferreira Filho, H. Brandao Malbouisson, W. Carvalho, J. Chinellato[6], E.M. Da Costa, G.G. Da Silveira[7], D. De Jesus Damiao, S. Fonseca De Souza, R. Gomes De Souza, T. Laux Kuhn[7], M. Macedo, J. Martins, L. Mundim, H. Nogima, J.P. Pinheiro, A. Santoro, A. Sznajder, M. Thiel

Universidade Estadual Paulista, Universidade Federal do ABC, São Paulo, Brazil

C.A. Bernardes[7], L. Calligaris, T.R. Fernandez Perez Tomei, E.M. Gregores, I. Maietto Silverio, P.G. Mercadante, S.F. Novaes, B. Orzari, Sandra S. Padula

2024 JINST 19 P11021

Institute for Nuclear Research and Nuclear Energy, Bulgarian Academy of Sciences, Sofia, Bulgaria
A. Aleksandrov, G. Antchev, R. Hadjiiska, P. Iaydjiev, M. Misheva, M. Shopova, G. Sultanov

University of Sofia, Sofia, Bulgaria
A. Dimitrov, L. Litov, B. Pavlov, P. Petkov, A. Petrov, E. Shumka

Instituto De Alta Investigación, Universidad de Tarapacá, Casilla 7 D, Arica, Chile
S. Keshri, D. Laroze, S. Thakur

Beihang University, Beijing, China
T. Cheng, T. Javaid, L. Yuan

Department of Physics, Tsinghua University, Beijing, China
Z. Hu, Z. Liang, J. Liu

Institute of High Energy Physics, Beijing, China
G.M. Chen[8], H.S. Chen[8], M. Chen[8], F. Iemmi, C.H. Jiang, A. Kapoor[9], H. Liao, Z.-A. Liu[10], R. Sharma[11], J.N. Song[10], J. Tao, C. Wang[8], J. Wang, Z. Wang[8], H. Zhang, J. Zhao

State Key Laboratory of Nuclear Physics and Technology, Peking University, Beijing, China
A. Agapitos, Y. Ban, S. Deng, B. Guo, C. Jiang, A. Levin, C. Li, Q. Li, Y. Mao, S. Qian, S.J. Qian, X. Qin, X. Sun, D. Wang, H. Yang, L. Zhang, Y. Zhao, C. Zhou

Guangdong Provincial Key Laboratory of Nuclear Science and Guangdong-Hong Kong Joint Laboratory of Quantum Matter, South China Normal University, Guangzhou, China
S. Yang

Sun Yat-Sen University, Guangzhou, China
Z. You

University of Science and Technology of China, Hefei, China
K. Jaffel, N. Lu

Nanjing Normal University, Nanjing, China
G. Bauer[12], B. Li[13], K. Yi[14], J. Zhang

Institute of Modern Physics and Key Laboratory of Nuclear Physics and Ion-beam Application (MOE) - Fudan University, Shanghai, China
Y. Li

Zhejiang University, Hangzhou, Zhejiang, China
Z. Lin, C. Lu, M. Xiao

Universidad de Los Andes, Bogota, Colombia
C. Avila, D.A. Barbosa Trujillo, A. Cabrera, C. Florez, J. Fraga, J.A. Reyes Vega

2024 JINST 19 P11021

Universidad de Antioquia, Medellin, Colombia
F. Ramirez, C. Rendón, M. Rodriguez, A.A. Ruales Barbosa, J.D. Ruiz Alvarez

University of Split, Faculty of Electrical Engineering, Mechanical Engineering and Naval Architecture, Split, Croatia
D. Giljanovic, N. Godinovic, D. Lelas, A. Sculac

University of Split, Faculty of Science, Split, Croatia
M. Kovac, A. Petkovic, T. Sculac

Institute Rudjer Boskovic, Zagreb, Croatia
P. Bargassa, V. Brigljevic, B.K. Chitroda, D. Ferencek, K. Jakovcic, A. Starodumov[15], T. Susa

University of Cyprus, Nicosia, Cyprus
A. Attikis, K. Christoforou, A. Hadjiagapiou, C. Leonidou, J. Mousa, C. Nicolaou, L. Paizanos, F. Ptochos, P.A. Razis, H. Rykaczewski, H. Saka, A. Stepennov

Charles University, Prague, Czech Republic
M. Finger, M. Finger Jr., A. Kveton

Escuela Politecnica Nacional, Quito, Ecuador
E. Ayala

Universidad San Francisco de Quito, Quito, Ecuador
E. Carrera Jarrin

Academy of Scientific Research and Technology of the Arab Republic of Egypt, Egyptian Network of High Energy Physics, Cairo, Egypt
Y. Assran[16,17], B. El-mahdy, S. Elgammal[17]

Center for High Energy Physics (CHEP-FU), Fayoum University, El-Fayoum, Egypt
M. Abdullah Al-Mashad, Y. Mohammed

National Institute of Chemical Physics and Biophysics, Tallinn, Estonia
K. Ehataht, M. Kadastik, T. Lange, S. Nandan, C. Nielsen, J. Pata, M. Raidal, L. Tani, C. Veelken

Department of Physics, University of Helsinki, Helsinki, Finland
H. Kirschenmann, K. Osterberg, M. Voutilainen

Helsinki Institute of Physics, Helsinki, Finland
S. Bharthuar, N. Bin Norjoharuddeen, E. Brücken, F. Garcia, P. Inkaew, K.T.S. Kallonen, T. Lampén, K. Lassila-Perini, S. Lehti, T. Lindén, M. Myllymäki, M.m. Rantanen, H. Siikonen, J. Tuominiemi

Lappeenranta-Lahti University of Technology, Lappeenranta, Finland
P. Luukka, H. Petrow

2024 JINST 19 P11021

IRFU, CEA, Université Paris-Saclay, Gif-sur-Yvette, France
M. Besancon, F. Couderc, M. Dejardin, D. Denegri, J.L. Faure, F. Ferri, S. Ganjour, P. Gras, G. Hamel de Monchenault, M. Kumar, V. Lohezic, J. Malcles, F. Orlandi, L. Portales, A. Rosowsky, M.Ö. Sahin, A. Savoy-Navarro[18], P. Simkina, M. Titov, M. Tornago

Laboratoire Leprince-Ringuet, CNRS/IN2P3, Ecole Polytechnique, Institut Polytechnique de Paris, Palaiseau, France
F. Beaudette, G. Boldrini, P. Busson, A. Cappati, C. Charlot, M. Chiusi, T.D. Cuisset, F. Damas, O. Davignon, A. De Wit, I.T. Ehle, B.A. Fontana Santos Alves, S. Ghosh, A. Gilbert, R. Granier de Cassagnac, A. Hakimi, B. Harikrishnan, L. Kalipoliti, G. Liu, M. Nguyen, C. Ochando, R. Salerno, J.B. Sauvan, Y. Sirois, L. Urda Gómez, E. Vernazza, A. Zabi, A. Zghiche

Université de Strasbourg, CNRS, IPHC UMR 7178, Strasbourg, France
J.-L. Agram[19], J. Andrea, D. Apparu, D. Bloch, J.-M. Brom, E.C. Chabert, C. Collard, S. Falke, U. Goerlach, R. Haeberle, A.-C. Le Bihan, M. Meena, O. Poncet, G. Saha, M.A. Sessini, P. Van Hove, P. Vaucelle

Centre de Calcul de l'Institut National de Physique Nucleaire et de Physique des Particules, CNRS/IN2P3, Villeurbanne, France
A. Di Florio

Institut de Physique des 2 Infinis de Lyon (IP2I), Villeurbanne, France
D. Amram, S. Beauceron, B. Blancon, G. Boudoul, N. Chanon, D. Contardo, P. Depasse, C. Dozen[20], H. El Mamouni, J. Fay, S. Gascon, M. Gouzevitch, C. Greenberg, G. Grenier, B. Ille, E. Jourd'huy, I.B. Laktineh, M. Lethuillier, L. Mirabito, S. Perries, A. Purohit, M. Vander Donckt, P. Verdier, J. Xiao

Georgian Technical University, Tbilisi, Georgia
I. Bagaturia[21], I. Lomidze, Z. Tsamalaidze[15]

RWTH Aachen University, I. Physikalisches Institut, Aachen, Germany
V. Botta, S. Consuegra Rodríguez, L. Feld, K. Klein, M. Lipinski, D. Meuser, A. Pauls, D. Pérez Adán, N. Röwert, M. Teroerde

RWTH Aachen University, III. Physikalisches Institut A, Aachen, Germany
S. Diekmann, A. Dodonova, N. Eich, D. Eliseev, F. Engelke, J. Erdmann, M. Erdmann, P. Fackeldey, B. Fischer, T. Hebbeker, K. Hoepfner, F. Ivone, A. Jung, M.y. Lee, L. Mastrolorenzo, F. Mausolf, M. Merschmeyer, A. Meyer, S. Mukherjee, D. Noll, F. Nowotny, A. Pozdnyakov, Y. Rath, W. Redjeb, F. Rehm, H. Reithler, V. Sarkisovi, A. Schmidt, C. Seth, A. Sharma, J.L. Spah, A. Stein, F. Torres Da Silva De Araujo[22], S. Wiedenbeck, S. Zaleski

RWTH Aachen University, III. Physikalisches Institut B, Aachen, Germany
C. Dziwok, G. Flügge, T. Kress, A. Nowack, O. Pooth, A. Stahl, T. Ziemons, A. Zotz

2024 JINST 19 P11021

Deutsches Elektronen-Synchrotron, Hamburg, Germany

H. Aarup Petersen, M. Aldaya Martin, J. Alimena, S. Amoroso, Y. An, J. Bach, S. Baxter, M. Bayatmakou, H. Becerril Gonzalez, O. Behnke, A. Belvedere, F. Blekman[23], K. Borras[24], A. Campbell, A. Cardini, C. Cheng, F. Colombina, G. Eckerlin, D. Eckstein, L.I. Estevez Banos, E. Gallo[23], A. Geiser, V. Guglielmi, M. Guthoff, A. Hinzmann, L. Jeppe, B. Kaech, M. Kasemann, C. Kleinwort, R. Kogler, M. Komm, D. Krücker, W. Lange, D. Leyva Pernia, K. Lipka[25], W. Lohmann[26], F. Lorkowski, R. Mankel, I.-A. Melzer-Pellmann, M. Mendizabal Morentin, A.B. Meyer, G. Milella, K. Moral Figueroa, A. Mussgiller, L.P. Nair, J. Niedziela, A. Nürnberg, Y. Otarid, J. Park, E. Ranken, A. Raspereza, D. Rastorguev, J. Rübenach, L. Rygaard, A. Saggio, M. Scham[27,24], S. Schnake[24], P. Schütze, C. Schwanenberger[23], D. Selivanova, K. Sharko, M. Shchedrolosiev, D. Stafford, F. Vazzoler, A. Ventura Barroso, R. Walsh, D. Wang, Q. Wang, K. Wichmann, L. Wiens[24], C. Wissing, Y. Yang, A. Zimermmane Castro Santos

University of Hamburg, Hamburg, Germany

A. Albrecht, S. Albrecht, M. Antonello, S. Bein, S. Bollweg, M. Bonanomi, P. Connor, K. El Morabit, Y. Fischer, E. Garutti, A. Grohsjean, J. Haller, D. Hundhausen, H.R. Jabusch, G. Kasieczka, P. Keicher, R. Klanner, W. Korcari, T. Kramer, C.c. Kuo, V. Kutzner, F. Labe, J. Lange, A. Lobanov, C. Matthies, L. Moureaux, M. Mrowietz, A. Nigamova, Y. Nissan, A. Paasch, K.J. Pena Rodriguez, T. Quadfasel, B. Raciti, M. Rieger, D. Savoiu, J. Schindler, P. Schleper, M. Schröder, J. Schwandt, M. Sommerhalder, H. Stadie, G. Steinbrück, A. Tews, B. Wiederspan, M. Wolf

Karlsruher Institut fuer Technologie, Karlsruhe, Germany

S. Brommer, E. Butz, T. Chwalek, A. Dierlamm, A. Droll, U. Elicabuk, N. Faltermann, M. Giffels, A. Gottmann, F. Hartmann[28], R. Hofsaess, M. Horzela, U. Husemann, J. Kieseler, M. Klute, R. Koppenhöfer, O. Lavoryk, J.M. Lawhorn, M. Link, A. Lintuluoto, S. Maier, S. Mitra, M. Mormile, Th. Müller, M. Neukum, M. Oh, E. Pfeffer, M. Presilla, G. Quast, K. Rabbertz, B. Regnery, N. Shadskiy, I. Shvetsov, H.J. Simonis, L. Sowa, L. Stockmeier, K. Tauqeer, M. Toms, N. Trevisani, R.F. Von Cube, M. Wassmer, S. Wieland, F. Wittig, R. Wolf, X. Zuo

Institute of Nuclear and Particle Physics (INPP), NCSR Demokritos, Aghia Paraskevi, Greece

G. Anagnostou, G. Daskalakis, A. Kyriakis, A. Papadopoulos[28], A. Stakia

National and Kapodistrian University of Athens, Athens, Greece

P. Kontaxakis, G. Melachroinos, Z. Painesis, I. Papavergou, I. Paraskevas, N. Saoulidou, K. Theofilatos, E. Tziaferi, K. Vellidis, I. Zisopoulos

National Technical University of Athens, Athens, Greece

G. Bakas, T. Chatzistavrou, G. Karapostoli, K. Kousouris, I. Papakrivopoulos, E. Siamarkou, G. Tsipolitis, A. Zacharopoulou

University of Ioánnina, Ioánnina, Greece

I. Bestintzanos, I. Evangelou, C. Foudas, C. Kamtsikis, P. Katsoulis, P. Kokkas, P.G. Kosmoglou Kioseoglou, N. Manthos, I. Papadopoulos, J. Strologas

2024 JINST 19 P11021

HUN-REN Wigner Research Centre for Physics, Budapest, Hungary
C. Hajdu, D. Horvath[29,30], K. Márton, A.J. Rádl[31], F. Sikler, V. Veszpremi

MTA-ELTE Lendület CMS Particle and Nuclear Physics Group, Eötvös Loránd University, Budapest, Hungary
M. Csanád, K. Farkas, A. Fehérkuti[32], M.M.A. Gadallah[33], Á. Kadlecsik, P. Major, G. Pásztor, G.I. Veres

Faculty of Informatics, University of Debrecen, Debrecen, Hungary
L. Olah, G. Zilizi

HUN-REN ATOMKI - Institute of Nuclear Research, Debrecen, Hungary
G. Bencze, S. Czellar, J. Molnar, Z. Szillasi

Karoly Robert Campus, MATE Institute of Technology, Gyongyos, Hungary
T. Csorgo[32], F. Nemes[32], T. Novak

Panjab University, Chandigarh, India
S. Bansal, S.B. Beri, V. Bhatnagar, G. Chaudhary, S. Chauhan, N. Dhingra[34], A. Kaur, A. Kaur, H. Kaur, M. Kaur, S. Kumar, T. Sheokand, J.B. Singh, A. Singla

University of Delhi, Delhi, India
A. Ahmed, A. Bhardwaj, A. Chhetri, B.C. Choudhary, A. Kumar, A. Kumar, M. Naimuddin, K. Ranjan, M.K. Saini, S. Saumya

Saha Institute of Nuclear Physics, HBNI, Kolkata, India
S. Baradia, S. Barman[35], S. Bhattacharya, S. Das Gupta, S. Dey, S. Dutta, S. Dutta, S. Sarkar

Indian Institute of Technology Madras, Madras, India
M.M. Ameen, P.K. Behera, S.C. Behera, S. Chatterjee, G. Dash, P. Jana, P. Kalbhor, S. Kamble, J.R. Komaragiri[36], D. Kumar[36], T. Mishra, B. Parida[37], P.R. Pujahari, N.R. Saha, A. Sharma, A.K. Sikdar, R.K. Singh, P. Verma, S. Verma, A. Vijay

Tata Institute of Fundamental Research-A, Mumbai, India
S. Dugad, G.B. Mohanty, M. Shelake, P. Suryadevara

Tata Institute of Fundamental Research-B, Mumbai, India
A. Bala, S. Banerjee, R.M. Chatterjee, M. Guchait, Sh. Jain, A. Jaiswal, S. Kumar, G. Majumder, K. Mazumdar, S. Parolia, N. Sahoo, A. Thachayath

National Institute of Science Education and Research, An OCC of Homi Bhabha National Institute, Bhubaneswar, Odisha, India
S. Bahinipati[38], C. Kar, B. Mahakud, D. Maity[39], P. Mal, V.K. Muraleedharan Nair Bindhu[39], K. Naskar[39], A. Nayak[39], S. Nayak, K. Pal, P. Sadangi, N. Sur, S.K. Swain, S. Varghese[39], D. Vats[39]

2024 JINST 19 P11021

Indian Institute of Science Education and Research (IISER), Pune, India
S. Acharya[40], A. Alpana, S. Dube, B. Gomber[40], P. Hazarika, B. Kansal, A. Laha, A. Rastogi, B. Sahu[40], S. Sharma, K.Y. Vaish

Isfahan University of Technology, Isfahan, Iran
H. Bakhshiansohi[41], A. Jafari[42], M. Zeinali[43]

Institute for Research in Fundamental Sciences (IPM), Tehran, Iran
S. Bashiri, S. Chenarani[44], S.M. Etesami, Y. Hosseini, M. Khakzad, E. Khazaie, M. Mohammadi Najafabadi, B. Safarzadeh[45], S. Tizchang[46]

University College Dublin, Dublin, Ireland
M. Felcini, M. Grunewald

INFN Sezione di Bari[a], Università di Bari[b], Politecnico di Bari[c], Bari, Italy
M. Abbrescia[a,b], A. Colaleo[a,b], D. Creanza[a,c], B. D'Anzi[a,b], N. De Filippis[a,c], M. De Palma[a,b], W. Elmetenawee[a,b,47], N. Ferrara[a,b], L. Fiore[a], G. Iaselli[a,c], L. Longo[a], M. Louka[a,b], G. Maggi[a,c], M. Maggi[a], I. Margjeka[a], V. Mastrapasqua[a,b], S. My[a,b], S. Nuzzo[a,b], A. Pellecchia[a,b], A. Pompili[a,b], G. Pugliese[a,c], R. Radogna[a,b], D. Ramos[a], A. Ranieri[a], L. Silvestris[a], F.M. Simone[a,c], Ü. Sözbilir[a], A. Stamerra[a,b], D. Troiano[a,b], R. Venditti[a,b], P. Verwilligen[a], A. Zaza[a,b]

INFN Sezione di Bologna[a], Università di Bologna[b], Bologna, Italy
G. Abbiendi[a], C. Battilana[a,b], D. Bonacorsi[a,b], P. Capiluppi[a,b], A. Castro[†,a,b], F.R. Cavallo[a], M. Cuffiani[a,b], G.M. Dallavalle[a], T. Diotalevi[a,b], F. Fabbri[a], A. Fanfani[a,b], D. Fasanella[a], P. Giacomelli[a], L. Giommi[a,b], C. Grandi[a], L. Guiducci[a,b], S. Lo Meo[a,48], M. Lorusso[a,b], L. Lunerti[a], S. Marcellini[a], G. Masetti[a], F.L. Navarria[a,b], G. Paggi[a,b], A. Perrotta[a], F. Primavera[a,b], A.M. Rossi[a,b], S. Rossi Tisbeni[a,b], T. Rovelli[a,b], G.P. Siroli[a,b]

INFN Sezione di Catania[a], Università di Catania[b], Catania, Italy
S. Costa[a,b,49], A. Di Mattia[a], A. Lapertosa[a], R. Potenza[a,b], A. Tricomi[a,b,49], C. Tuve[a,b]

INFN Sezione di Firenze[a], Università di Firenze[b], Firenze, Italy
P. Assiouras[a], G. Barbagli[a], G. Bardelli[a,b], B. Camaiani[a,b], A. Cassese[a], R. Ceccarelli[a], V. Ciulli[a,b], C. Civinini[a], R. D'Alessandro[a,b], E. Focardi[a,b], T. Kello[a], G. Latino[a,b], P. Lenzi[a,b], M. Lizzo[a], M. Meschini[a], S. Paoletti[a], A. Papanastassiou[a,b], G. Sguazzoni[a], L. Viliani[a]

INFN Laboratori Nazionali di Frascati, Frascati, Italy
L. Benussi, S. Bianco, S. Meola[50], D. Piccolo

INFN Sezione di Genova[a], Università di Genova[b], Genova, Italy
M. Alves Gallo Pereira[a], F. Ferro[a], E. Robutti[a], S. Tosi[a,b]

INFN Sezione di Milano-Bicocca[a], Università di Milano-Bicocca[b], Milano, Italy
A. Benaglia[a], F. Brivio[a], F. Cetorelli[a,b], F. De Guio[a,b], M.E. Dinardo[a,b], P. Dini[a], S. Gennai[a], R. Gerosa[a,b], A. Ghezzi[a,b], P. Govoni[a,b], L. Guzzi[a], M.T. Lucchini[a,b], M. Malberti[a],

2024 JINST 19 P11021

S. Malvezzi[a], A. Massironi[a], D. Menasce[a], L. Moroni[a], M. Paganoni[a,b], S. Palluotto[a,b], D. Pedrini[a], A. Perego[a,b], B.S. Pinolini[a], G. Pizzati[a,b], S. Ragazzi[a,b], T. Tabarelli de Fatis[a,b]

INFN Sezione di Napoli[a], Università di Napoli 'Federico II'[b], Napoli, Italy; Università della Basilicata[c], Potenza, Italy; Scuola Superiore Meridionale (SSM)[d], Napoli, Italy

S. Buontempo[a], A. Cagnotta[a,b], F. Carnevali[a,b], N. Cavallo[a,c], F. Fabozzi[a,c], A.O.M. Iorio[a,b], L. Lista[a,b,51], P. Paolucci[a,28], B. Rossi[a]

INFN Sezione di Padova[a], Università di Padova[b], Padova, Italy; Università di Trento[c], Trento, Italy

R. Ardino[a], P. Azzi[a], N. Bacchetta[a,52], M. Biasotto[a,53], D. Bisello[a,b], P. Bortignon[a], G. Bortolato[a,b], A. Bragagnolo[a,b], A.C.M. Bulla[a], R. Carlin[a,b], P. Checchia[a], L. Ciano[a], T. Dorigo[a], F. Gasparini[a,b], U. Gasparini[a,b], S. Giorgetti[a], E. Lusiani[a], M. Margoni[a,b], M. Migliorini[a,b], M. Passaseo[a], J. Pazzini[a,b], P. Ronchese[a,b], R. Rossin[a,b], F. Simonetto[a,b], M. Tosi[a,b], A. Triossi[a,b], S. Ventura[a], M. Zanetti[a,b], P. Zotto[a,b], A. Zucchetta[a,b]

INFN Sezione di Pavia[a], Università di Pavia[b], Pavia, Italy

A. Braghieri[a], S. Calzaferri[a], D. Fiorina[a], P. Montagna[a,b], V. Re[a], C. Riccardi[a,b], P. Salvini[a], I. Vai[a,b], P. Vitulo[a,b]

INFN Sezione di Perugia[a], Università di Perugia[b], Perugia, Italy

S. Ajmal[a,b], M.E. Ascioti[a,b], G.M. Bilei[a], C. Carrivale[a,b], D. Ciangottini[a,b], L. Fanò[a,b], M. Magherini[a,b], V. Mariani[a,b], M. Menichelli[a], F. Moscatelli[a,54], A. Rossi[a,b], A. Santocchia[a,b], D. Spiga[a], T. Tedeschi[a,b]

INFN Sezione di Pisa[a], Università di Pisa[b], Scuola Normale Superiore di Pisa[c], Pisa, Italy; Università di Siena[d], Siena, Italy

C. Aimè[a], C.A. Alexe[a,c], P. Asenov[a,b], P. Azzurri[a], G. Bagliesi[a], R. Bhattacharya[a], L. Bianchini[a,b], T. Boccali[a], E. Bossini[a], D. Bruschini[a,c], R. Castaldi[a], M.A. Ciocci[a,b], M. Cipriani[a,b], V. D'Amante[a,d], R. Dell'Orso[a], S. Donato[a], A. Giassi[a], F. Ligabue[a,c], A.C. Marini[a], L. Martini[a,b], D. Matos Figueiredo[a], A. Messineo[a,b], S. Mishra[a], M. Musich[a,b], F. Palla[a], A. Rizzi[a,b], G. Rolandi[a,c], S. Roy Chowdhury[a], T. Sarkar[a], A. Scribano[a], P. Spagnolo[a], R. Tenchini[a], G. Tonelli[a,b], N. Turini[a,d], F. Vaselli[a,c], A. Venturi[a], P.G. Verdini[a]

INFN Sezione di Roma[a], Sapienza Università di Roma[b], Roma, Italy

C. Baldenegro Barrera[a,b], P. Barria[a], C. Basile[a,b], F. Cavallari[a], L. Cunqueiro Mendez[a,b], D. Del Re[a,b], E. Di Marco[a,b], M. Diemoz[a], F. Errico[a,b], R. Gargiulo[a,b], E. Longo[a,b], L. Martikainen[a,b], J. Mijuskovic[a,b], G. Organtini[a,b], F. Pandolfi[a], R. Paramatti[a,b], C. Quaranta[a,b], S. Rahatlou[a,b], C. Rovelli[a], F. Santanastasio[a,b], L. Soffi[a], V. Vladimirov[a,b]

INFN Sezione di Torino[a], Università di Torino[b], Torino, Italy; Università del Piemonte Orientale[c], Novara, Italy

N. Amapane[a,b], R. Arcidiacono[a,c], S. Argiro[a,b], M. Arneodo[a,c], N. Bartosik[a], R. Bellan[a,b], A. Bellora[a,b], C. Biino[a], C. Borca[a,b], N. Cartiglia[a], M. Costa[a,b], R. Covarelli[a,b],

2024 JINST 19 P11021

N. Demaria[a], L. Finco[a], M. Grippo[a,b], B. Kiani[a,b], F. Legger[a], F. Luongo[a,b], C. Mariotti[a], L. Markovic[a,b], S. Maselli[a], A. Mecca[a,b], L. Menzio[a,b], P. Meridiani[a], E. Migliore[a,b], M. Monteno[a], R. Mulargia[a], M.M. Obertino[a,b], G. Ortona[a], L. Pacher[a,b], N. Pastrone[a], M. Pelliccioni[a], M. Ruspa[a,c], F. Siviero[a,b], V. Sola[a,b], A. Solano[a,b], A. Staiano[a], C. Tarricone[a,b], D. Trocino[a], G. Umoret[a,b], R. White[a,b]

INFN Sezione di Trieste[a], Università di Trieste[b], Trieste, Italy

J. Babbar[a,b], S. Belforte[a], V. Candelise[a,b], M. Casarsa[a], F. Cossutti[a], K. De Leo[a], G. Della Ricca[a,b]

Kyungpook National University, Daegu, Korea

S. Dogra, J. Hong, B. Kim, J. Kim, D. Lee, H. Lee, S.W. Lee, C.S. Moon, Y.D. Oh, M.S. Ryu, S. Sekmen, B. Tae, Y.C. Yang

Department of Mathematics and Physics - GWNU, Gangneung, Korea

M.S. Kim

Chonnam National University, Institute for Universe and Elementary Particles, Kwangju, Korea

G. Bak, P. Gwak, H. Kim, D.H. Moon

Hanyang University, Seoul, Korea

E. Asilar, J. Choi, D. Kim, T.J. Kim, J.A. Merlin, Y. Ryou

Korea University, Seoul, Korea

S. Choi, S. Han, B. Hong, K. Lee, K.S. Lee, S. Lee, J. Yoo

Kyung Hee University, Department of Physics, Seoul, Korea

J. Goh, S. Yang

Sejong University, Seoul, Korea

H. S. Kim, Y. Kim, S. Lee

Seoul National University, Seoul, Korea

J. Almond, J.H. Bhyun, J. Choi, J. Choi, W. Jun, J. Kim, Y.W. Kim, S. Ko, H. Kwon, H. Lee, J. Lee, J. Lee, B.H. Oh, S.B. Oh, H. Seo, U.K. Yang, I. Yoon

University of Seoul, Seoul, Korea

W. Jang, D.Y. Kang, Y. Kang, S. Kim, B. Ko, J.S.H. Lee, Y. Lee, I.C. Park, Y. Roh, I.J. Watson

Yonsei University, Department of Physics, Seoul, Korea

S. Ha, K. Hwang, H.D. Yoo

Sungkyunkwan University, Suwon, Korea

M. Choi, M.R. Kim, H. Lee, Y. Lee, I. Yu

College of Engineering and Technology, American University of the Middle East (AUM), Dasman, Kuwait

T. Beyrouthy, Y. Gharbia

2024 JINST 19 P11021

Kuwait University - College of Science - Department of Physics, Safat, Kuwait
F. Alazemi

Riga Technical University, Riga, Latvia
K. Dreimanis, A. Gaile, C. Munoz Diaz, D. Osite, G. Pikurs, A. Potrebko, M. Seidel, D. Sidiropoulos Kontos

University of Latvia (LU), Riga, Latvia
N.R. Strautnieks

Vilnius University, Vilnius, Lithuania
M. Ambrozas, A. Juodagalvis, A. Rinkevicius, G. Tamulaitis

National Centre for Particle Physics, Universiti Malaya, Kuala Lumpur, Malaysia
I. Yusuff[55], Z. Zolkapli

Universidad de Sonora (UNISON), Hermosillo, Mexico
J.F. Benitez, A. Castaneda Hernandez, H.A. Encinas Acosta, L.G. Gallegos Maríñez, M. León Coello, J.A. Murillo Quijada, A. Sehrawat, L. Valencia Palomo

Centro de Investigacion y de Estudios Avanzados del IPN, Mexico City, Mexico
G. Ayala, H. Castilla-Valdez, H. Crotte Ledesma, E. De La Cruz-Burelo, I. Heredia-De La Cruz[56], R. Lopez-Fernandez, J. Mejia Guisao, C.A. Mondragon Herrera, A. Sánchez Hernández

Universidad Iberoamericana, Mexico City, Mexico
C. Oropeza Barrera, D.L. Ramirez Guadarrama, M. Ramírez García

Benemerita Universidad Autonoma de Puebla, Puebla, Mexico
I. Bautista, I. Pedraza, H.A. Salazar Ibarguen, C. Uribe Estrada

University of Montenegro, Podgorica, Montenegro
I. Bubanja, N. Raicevic

University of Canterbury, Christchurch, New Zealand
P.H. Butler

National Centre for Physics, Quaid-I-Azam University, Islamabad, Pakistan
A. Ahmad, M.I. Asghar, A. Awais, M.I.M. Awan, H.R. Hoorani, W.A. Khan

AGH University of Krakow, Krakow, Poland
V. Avati, L. Grzanka, M. Malawski

National Centre for Nuclear Research, Swierk, Poland
H. Bialkowska, M. Bluj, M. Górski, M. Kazana, M. Szleper, P. Zalewski

Institute of Experimental Physics, Faculty of Physics, University of Warsaw, Warsaw, Poland
K. Bunkowski, K. Doroba, A. Kalinowski, M. Konecki, J. Krolikowski, A. Muhammad

2024 JINST 19 P11021

Warsaw University of Technology, Warsaw, Poland
P. Fokow, K. Pozniak, W. Zabolotny

Laboratório de Instrumentação e Física Experimental de Partículas, Lisboa, Portugal
M. Araujo, D. Bastos, C. Beirão Da Cruz E Silva, A. Boletti, M. Bozzo, T. Camporesi, G. Da Molin, P. Faccioli, M. Gallinaro, J. Hollar, N. Leonardo, G.B. Marozzo, A. Petrilli, M. Pisano, J. Seixas, J. Varela, J.W. Wulff

Faculty of Physics, University of Belgrade, Belgrade, Serbia
P. Adzic, P. Milenovic

VINCA Institute of Nuclear Sciences, University of Belgrade, Belgrade, Serbia
D. Devetak, M. Dordevic, J. Milosevic, L. Nadderd, V. Rekovic

Centro de Investigaciones Energéticas Medioambientales y Tecnológicas (CIEMAT), Madrid, Spain
J. Alcaraz Maestre, Cristina F. Bedoya, J.A. Brochero Cifuentes, Oliver M. Carretero, M. Cepeda, M. Cerrada, N. Colino, B. De La Cruz, A. Delgado Peris, A. Escalante Del Valle, D. Fernández Del Val, J.P. Fernández Ramos, J. Flix, M.C. Fouz, O. Gonzalez Lopez, S. Goy Lopez, J.M. Hernandez, M.I. Josa, J. Llorente Merino, C. Martin Perez, E. Martin Viscasillas, D. Moran, C. M. Morcillo Perez, Á. Navarro Tobar, C. Perez Dengra, A. Pérez-Calero Yzquierdo, J. Puerta Pelayo, I. Redondo, S. Sánchez Navas, J. Sastre, J. Vazquez Escobar

Universidad Autónoma de Madrid, Madrid, Spain
J.F. de Trocóniz

Universidad de Oviedo, Instituto Universitario de Ciencias y Tecnologías Espaciales de Asturias (ICTEA), Oviedo, Spain
B. Alvarez Gonzalez, J. Cuevas, J. Fernandez Menendez, S. Folgueras, I. Gonzalez Caballero, P. Leguina, E. Palencia Cortezon, J. Prado Pico, C. Ramón Álvarez, V. Rodríguez Bouza, A. Soto Rodríguez, A. Trapote, C. Vico Villalba, P. Vischia

Instituto de Física de Cantabria (IFCA), CSIC-Universidad de Cantabria, Santander, Spain
S. Bhowmik, S. Blanco Fernández, I.J. Cabrillo, A. Calderon, J. Duarte Campderros, M. Fernandez, G. Gomez, C. Lasaosa García, R. Lopez Ruiz, C. Martinez Rivero, P. Martinez Ruiz del Arbol, F. Matorras, P. Matorras Cuevas, E. Navarrete Ramos, J. Piedra Gomez, L. Scodellaro, I. Vila, J.M. Vizan Garcia

University of Colombo, Colombo, Sri Lanka
B. Kailasapathy[57], D.D.C. Wickramarathna

University of Ruhuna, Department of Physics, Matara, Sri Lanka
W.G.D. Dharmaratna[58], K. Liyanage, N. Perera

2024 JINST 19 P11021

CERN, European Organization for Nuclear Research, Geneva, Switzerland
D. Abbaneo, C. Amendola, E. Auffray, G. Auzinger, J. Baechler, D. Barney, A. Bermúdez Martínez, M. Bianco, A.A. Bin Anuar, A. Bocci, L. Borgonovi, C. Botta, E. Brondolin, C. Caillol, G. Cerminara, N. Chernyavskaya, S.S. Chhibra, D. d'Enterria, A. Dabrowski, N. Daci, A. David, A. De Roeck, M.M. Defranchis, M. Deile, M. Dobson, G. Franzoni, W. Funk, S. Giani, D. Gigi, K. Gill, F. Glege, J. Hegeman, J.K. Heikkilä, B. Huber, Y. Iiyama, V. Innocente, T. James, P. Janot, O. Kaluzinska, O. Karacheban[26], S. Laurila, P. Lecoq, E. Leutgeb, C. Lourenço, L. Malgeri, M. Mannelli, M. Matthewman, A. Mehta, F. Meijers, S. Mersi, E. Meschi, V. Milosevic, F. Monti, F. Moortgat, M. Mulders, I. Neutelings, S. Orfanelli, F. Pantaleo, G. Petrucciani, A. Pfeiffer, M. Pierini, H. Qu, D. Rabady, B. Ribeiro Lopes, F. Riti, M. Rovere, H. Sakulin, R. Salvatico, S. Sanchez Cruz, S. Scarfi, C. Schwick, M. Selvaggi, A. Sharma, K. Shchelina, P. Silva, P. Sphicas[59], A.G. Stahl Leiton, A. Steen, S. Summers, D. Treille, P. Tropea, D. Walter, J. Wanczyk[60], J. Wang, K.A. Wozniak[61], S. Wuchterl, P. Zehetner, P. Zejdl, W.D. Zeuner

Paul Scherrer Institut, Villigen, Switzerland
T. Bevilacqua[62], L. Caminada[62], A. Ebrahimi, W. Erdmann, R. Horisberger, Q. Ingram, H.C. Kaestli, D. Kotlinski, C. Lange, M. Missiroli[62], L. Noehte[62], T. Rohe, A. Samalan

ETH Zurich - Institute for Particle Physics and Astrophysics (IPA), Zurich, Switzerland
T.K. Aarrestad, M. Backhaus, G. Bonomelli, A. Calandri, C. Cazzaniga, K. Datta, P. De Bryas Dexmiers D'archiac[60], A. De Cosa, G. Dissertori, M. Dittmar, M. Donegà, F. Eble, M. Galli, K. Gedia, F. Glessgen, C. Grab, N. Härringer, T.G. Harte, D. Hits, W. Lustermann, A.-M. Lyon, R.A. Manzoni, M. Marchegiani, L. Marchese, A. Mascellani[60], F. Nessi-Tedaldi, F. Pauss, V. Perovic, S. Pigazzini, B. Ristic, R. Seidita, J. Steggemann[60], A. Tarabini, D. Valsecchi, R. Wallny

Universität Zürich, Zurich, Switzerland
C. Amsler[63], P. Bärtschi, M.F. Canelli, K. Cormier, M. Huwiler, W. Jin, A. Jofrehei, B. Kilminster, S. Leontsinis, S.P. Liechti, A. Macchiolo, P. Meiring, F. Meng, J. Motta, A. Reimers, P. Robmann, M. Senger, E. Shokr, F. Stäger, R. Tramontano

National Central University, Chung-Li, Taiwan
C. Adloff[64], D. Bhowmik, C.M. Kuo, W. Lin, P.K. Rout, P.C. Tiwari[36]

National Taiwan University (NTU), Taipei, Taiwan
L. Ceard, K.F. Chen, Z.g. Chen, A. De Iorio, W.-S. Hou, T.h. Hsu, Y.w. Kao, S. Karmakar, G. Kole, Y.y. Li, R.-S. Lu, E. Paganis, X.f. Su, J. Thomas-Wilsker, L.s. Tsai, D. Tsionou, H.y. Wu, E. Yazgan

High Energy Physics Research Unit, Department of Physics, Faculty of Science, Chulalongkorn University, Bangkok, Thailand
C. Asawatangtrakuldee, N. Srimanobhas, V. Wachirapusitanand

2024 JINST 19 P11021

Çukurova University, Physics Department, Science and Art Faculty, Adana, Turkey
D. Agyel, F. Boran, F. Dolek, I. Dumanoglu[65], E. Eskut, Y. Guler[66], E. Gurpinar Guler[66], C. Isik, O. Kara, A. Kayis Topaksu, U. Kiminsu, Y. Komurcu, G. Onengut, K. Ozdemir[67], A. Polatoz, B. Tali[68], U.G. Tok, E. Uslan, I.S. Zorbakir

Middle East Technical University, Physics Department, Ankara, Turkey
G. Sokmen, M. Yalvac[69]

Bogazici University, Istanbul, Turkey
B. Akgun, I.O. Atakisi, E. Gülmez, M. Kaya[70], O. Kaya[71], S. Tekten[72]

Istanbul Technical University, Istanbul, Turkey
A. Cakir, K. Cankocak[65,73], G.G. Dincer[65], S. Sen[74]

Istanbul University, Istanbul, Turkey
O. Aydilek[75], B. Hacisahinoglu, I. Hos[76], B. Kaynak, S. Ozkorucuklu, O. Potok, H. Sert, C. Simsek, C. Zorbilmez

Yildiz Technical University, Istanbul, Turkey
S. Cerci, B. Isildak[77], D. Sunar Cerci, T. Yetkin

Institute for Scintillation Materials of National Academy of Science of Ukraine, Kharkiv, Ukraine
A. Boyaryntsev, B. Grynyov

National Science Centre, Kharkiv Institute of Physics and Technology, Kharkiv, Ukraine
L. Levchuk

University of Bristol, Bristol, United Kingdom
D. Anthony, J.J. Brooke, A. Bundock, F. Bury, E. Clement, D. Cussans, H. Flacher, M. Glowacki, J. Goldstein, H.F. Heath, M.-L. Holmberg, L. Kreczko, S. Paramesvaran, L. Robertshaw, V.J. Smith, K. Walkingshaw Pass

Rutherford Appleton Laboratory, Didcot, United Kingdom
A.H. Ball, K.W. Bell, A. Belyaev[78], C. Brew, R.M. Brown, D.J.A. Cockerill, C. Cooke, A. Elliot, K.V. Ellis, K. Harder, S. Harper, J. Linacre, K. Manolopoulos, D.M. Newbold, E. Olaiya, D. Petyt, T. Reis, A.R. Sahasransu, G. Salvi, T. Schuh, C.H. Shepherd-Themistocleous, I.R. Tomalin, K.C. Whalen, T. Williams

Imperial College, London, United Kingdom
I. Andreou, R. Bainbridge, P. Bloch, C.E. Brown, O. Buchmuller, C.A. Carrillo Montoya, G.S. Chahal[79], D. Colling, J.S. Dancu, I. Das, P. Dauncey, G. Davies, M. Della Negra, P. Dunne, S. Fayer, G. Fedi, G. Hall, A. Howard, G. Iles, C.R. Knight, P. Krueper, J. Langford, K.H. Law, J. León Holgado, L. Lyons, A.-M. Magnan, B. Maier, S. Mallios, M. Mieskolainen, J. Nash[80], M. Pesaresi, P.B. Pradeep, B.C. Radburn-Smith, A. Richards, A. Rose, K. Savva,

2024 JINST 19 P11021

C. Seez, R. Shukla, T. Strebler, A. Tapper, K. Uchida, G.P. Uttley, T. Virdee[28], M. Vojinovic, N. Wardle, D. Winterbottom

Brunel University, Uxbridge, United Kingdom

J.E. Cole, A. Khan, P. Kyberd, I.D. Reid

Baylor University, Waco, Texas, U.S.A.

S. Abdullin, A. Brinkerhoff, E. Collins, M.R. Darwish, J. Dittmann, K. Hatakeyama, V. Hegde, J. Hiltbrand, B. McMaster, J. Samudio, S. Sawant, C. Sutantawibul, J. Wilson

Catholic University of America, Washington, DC, U.S.A.

R. Bartek, A. Dominguez, A.E. Simsek, S.S. Yu

The University of Alabama, Tuscaloosa, Alabama, U.S.A.

B. Bam, A. Buchot Perraguin, R. Chudasama, S.I. Cooper, C. Crovella, S.V. Gleyzer, E. Pearson, C.U. Perez, P. Rumerio[81], E. Usai, R. Yi

Boston University, Boston, Massachusetts, U.S.A.

A. Akpinar, A. Avetisyan, C. Cosby, G. De Castro, Z. Demiragli, C. Erice, C. Fangmeier, C. Fernandez Madrazo, E. Fontanesi, D. Gastler, F. Golf, S. Jeon, J. O'cain, I. Reed, C. Richardson, J. Rohlf, K. Salyer, D. Sperka, D. Spitzbart, I. Suarez, A. Tsatsos, A.G. Zecchinelli

Brown University, Providence, Rhode Island, U.S.A.

G. Barone, G. Benelli, X. Coubez[24], D. Cutts, L. Gouskos, M. Hadley, U. Heintz, K.W. Ho, J.M. Hogan[82], T. Kwon, G. Landsberg, K.T. Lau, J. Luo, S. Mondal, T. Russell, S. Sagir[83], X. Shen, F. Simpson, M. Stamenkovic, N. Venkatasubramanian

University of California, Davis, Davis, California, U.S.A.

S. Abbott, B. Barton, C. Brainerd, R. Breedon, H. Cai, M. Calderon De La Barca Sanchez, M. Chertok, M. Citron, J. Conway, P.T. Cox, R. Erbacher, F. Jensen, O. Kukral, G. Mocellin, M. Mulhearn, S. Ostrom, W. Wei, S. Yoo, F. Zhang

University of California, Los Angeles, California, U.S.A.

K. Adamidis, M. Bachtis, D. Campos, R. Cousins, A. Datta, G. Flores Avila, J. Hauser, M. Ignatenko, M.A. Iqbal, T. Lam, Y.f. Lo, E. Manca, A. Nunez Del Prado, D. Saltzberg, V. Valuev

University of California, Riverside, Riverside, California, U.S.A.

R. Clare, J.W. Gary, G. Hanson

University of California, San Diego, La Jolla, California, U.S.A.

A. Aportela, A. Arora, J.G. Branson, S. Cittolin, S. Cooperstein, M. De Gruttola[28], D. Diaz, J. Duarte, L. Giannini, Y. Gu, J. Guiang, R. Kansal, V. Krutelyov, R. Lee, J. Letts, M. Masciovecchio, F. Mokhtar, S. Mukherjee, D. Olivito, M. Pieri, D. Primosch, M. Quinnan, M. Sani, B.V. Sathia Narayanan, V. Sharma, M. Tadel, E. Vourliotis, F. Würthwein, Y. Xiang, A. Yagil

2024 JINST 19 P11021

University of California, Santa Barbara - Department of Physics, Santa Barbara, California, U.S.A.

A. Barzdukas, L. Brennan, C. Campagnari, K. Downham, M. Franco Sevilla, C. Grieco, M.M. Hussain, J. Incandela, J. Kim, A.J. Li, P. Masterson, H. Mei, J. Richman, S.N. Santpur, U. Sarica, R. Schmitz, F. Setti, J. Sheplock, D. Stuart, T.Á. Vámi, S. Wang, X. Yan, D. Zhang

California Institute of Technology, Pasadena, California, U.S.A.

D. Anderson, S. Bhattacharya, A. Bornheim, O. Cerri, A. Latorre, J. Mao, H.B. Newman, G. Reales Gutiérrez, M. Spiropulu, J.R. Vlimant, C. Wang, S. Xie, R.Y. Zhu

Carnegie Mellon University, Pittsburgh, Pennsylvania, U.S.A.

J. Alison, S. An, P. Bryant, M. Cremonesi, V. Dutta, T. Ferguson, T.A. Gómez Espinosa, A. Harilal, A. Kallil Tharayil, C. Liu, T. Mudholkar, S. Murthy, P. Palit, K. Park, M. Paulini, A. Roberts, A. Sanchez, W. Terrill

University of Colorado Boulder, Boulder, Colorado, U.S.A.

J.P. Cumalat, W.T. Ford, A. Hart, A. Hassani, G. Karathanasis, N. Manganelli, J. Pearkes, C. Savard, N. Schonbeck, K. Stenson, K.A. Ulmer, S.R. Wagner, N. Zipper, D. Zuolo

Cornell University, Ithaca, New York, U.S.A.

J. Alexander, S. Bright-Thonney, X. Chen, D.J. Cranshaw, J. Dickinson, J. Fan, X. Fan, S. Hogan, P. Kotamnives, J. Monroy, M. Oshiro, J.R. Patterson, M. Reid, A. Ryd, J. Thom, P. Wittich, R. Zou

Fermi National Accelerator Laboratory, Batavia, Illinois, U.S.A.

M. Albrow, M. Alyari, O. Amram, G. Apollinari, A. Apresyan, L.A.T. Bauerdick, D. Berry, J. Berryhill, P.C. Bhat, K. Burkett, J.N. Butler, A. Canepa, G.B. Cerati, H.W.K. Cheung, F. Chlebana, G. Cummings, I. Dutta, V.D. Elvira, Y. Feng, J. Freeman, A. Gandrakota, Z. Gecse, L. Gray, D. Green, A. Grummer, S. Grünendahl, D. Guerrero, O. Gutsche, R.M. Harris, R. Heller, T.C. Herwig, J. Hirschauer, B. Jayatilaka, S. Jindariani, M. Johnson, U. Joshi, T. Klijnsma, B. Klima, K.H.M. Kwok, S. Lammel, C. Lee, D. Lincoln, R. Lipton, T. Liu, C. Madrid, K. Maeshima, C. Mantilla, D. Mason, P. McBride, P. Merkel, S. Mrenna, S. Nahn, J. Ngadiuba, D. Noonan, S. Norberg, V. Papadimitriou, N. Pastika, K. Pedro, C. Pena[84], F. Ravera, A. Reinsvold Hall[85], L. Ristori, M. Safdari, E. Sexton-Kennedy, N. Smith, A. Soha, L. Spiegel, S. Stoynev, J. Strait, L. Taylor, S. Tkaczyk, N.V. Tran, L. Uplegger, E.W. Vaandering, I. Zoi

University of Florida, Gainesville, Florida, U.S.A.

C. Aruta, P. Avery, D. Bourilkov, P. Chang, V. Cherepanov, R.D. Field, C. Huh, E. Koenig, M. Kolosova, J. Konigsberg, A. Korytov, K. Matchev, N. Menendez, G. Mitselmakher, K. Mohrman, A. Muthirakalayil Madhu, N. Rawal, S. Rosenzweig, Y. Takahashi, J. Wang

Florida State University, Tallahassee, Florida, U.S.A.

T. Adams, A. Al Kadhim, A. Askew, S. Bower, R. Hashmi, R.S. Kim, S. Kim, T. Kolberg, G. Martinez, H. Prosper, P.R. Prova, M. Wulansatiti, R. Yohay, J. Zhang

2024 JINST 19 P11021

Florida Institute of Technology, Melbourne, Florida, U.S.A.
B. Alsufyani, S. Butalla, S. Das, T. Elkafrawy[86], M. Hohlmann, E. Yanes

University of Illinois Chicago, Chicago, Illinois, U.S.A.
M.R. Adams, L. Apanasevich, A. Baty, C. Bennett, R. Cavanaugh, R. Escobar Franco, O. Evdokimov, C.E. Gerber, M. Hawksworth, A. Hingrajiya, D.J. Hofman, J.h. Lee, D. S. Lemos, A.H. Merrit, C. Mills, S. Nanda, G. Oh, B. Ozek, D. Pilipovic, R. Pradhan, E. Prifti, T. Roy, S. Rudrabhatla, N. Singh, M.B. Tonjes, N. Varelas, M.A. Wadud, Z. Ye, J. Yoo

The University of Iowa, Iowa City, Iowa, U.S.A.
M. Alhusseini, D. Blend, K. Dilsiz[87], L. Emediato, G. Karaman, O.K. Köseyan, J.-P. Merlo, A. Mestvirishvili[88], O. Neogi, H. Ogul[89], Y. Onel, A. Penzo, C. Snyder, E. Tiras[90]

Johns Hopkins University, Baltimore, Maryland, U.S.A.
B. Blumenfeld, L. Corcodilos, J. Davis, A.V. Gritsan, L. Kang, S. Kyriacou, P. Maksimovic, M. Roguljic, J. Roskes, S. Sekhar, M. Swartz

The University of Kansas, Lawrence, Kansas, U.S.A.
A. Abreu, L.F. Alcerro Alcerro, J. Anguiano, S. Arteaga Escatel, P. Baringer, A. Bean, Z. Flowers, D. Grove, J. King, G. Krintiras, M. Lazarovits, C. Le Mahieu, J. Marquez, M. Murray, M. Nickel, M. Pitt, S. Popescu[91], C. Rogan, C. Royon, S. Sanders, C. Smith, G. Wilson

Kansas State University, Manhattan, Kansas, U.S.A.
B. Allmond, R. Gujju Gurunadha, A. Ivanov, K. Kaadze, Y. Maravin, J. Natoli, D. Roy, G. Sorrentino

University of Maryland, College Park, Maryland, U.S.A.
A. Baden, A. Belloni, J. Bistany-riebman, Y.M. Chen, S.C. Eno, N.J. Hadley, S. Jabeen, R.G. Kellogg, T. Koeth, B. Kronheim, Y. Lai, S. Lascio, A.C. Mignerey, S. Nabili, C. Palmer, C. Papageorgakis, M.M. Paranjpe, E. Popova[92], A. Shevelev, L. Wang

Massachusetts Institute of Technology, Cambridge, Massachusetts, U.S.A.
J. Bendavid, I.A. Cali, P.c. Chou, M. D'Alfonso, J. Eysermans, C. Freer, G. Gomez-Ceballos, M. Goncharov, G. Grosso, P. Harris, D. Hoang, G.M. Innocenti, D. Kovalskyi, K. Krajczar, J. Krupa, L. Lavezzo, Y.-J. Lee, K. Long, C. Mcginn, A. Novak, M.I. Park, C. Paus, D. Rankin, C. Reissel, C. Roland, G. Roland, S. Rothman, G.S.F. Stephans, Z. Wang, B. Wyslouch, T. J. Yang

University of Minnesota, Minneapolis, Minnesota, U.S.A.
B. Crossman, B.M. Joshi, C. Kapsiak, M. Krohn, D. Mahon, J. Mans, B. Marzocchi, M. Revering, R. Rusack, R. Saradhy, N. Strobbe

University of Nebraska-Lincoln, Lincoln, Nebraska, U.S.A.
K. Bloom, D.R. Claes, G. Haza, J. Hossain, C. Joo, I. Kravchenko, A. Rohilla, J.E. Siado, W. Tabb, A. Vagnerini, A. Wightman, F. Yan, D. Yu

2024 JINST 19 P11021

State University of New York at Buffalo, Buffalo, New York, U.S.A.
H. Bandyopadhyay, L. Hay, H.w. Hsia, I. Iashvili, A. Kalogeropoulos, A. Kharchilava, M. Morris, D. Nguyen, S. Rappoccio, H. Rejeb Sfar, A. Williams, P. Young

Northeastern University, Boston, Massachusetts, U.S.A.
G. Alverson, E. Barberis, J. Bonilla, B. Bylsma, M. Campana, J. Dervan, Y. Haddad, Y. Han, I. Israr, A. Krishna, J. Li, M. Lu, G. Madigan, R. Mccarthy, D.M. Morse, V. Nguyen, T. Orimoto, A. Parker, L. Skinnari, D. Wood

Northwestern University, Evanston, Illinois, U.S.A.
J. Bueghly, S. Dittmer, K.A. Hahn, D. Li, Y. Liu, M. Mcginnis, Y. Miao, D.G. Monk, N. Odell, M.H. Schmitt, A. Taliercio, M. Trovato, M. Velasco

University of Notre Dame, Notre Dame, Indiana, U.S.A.
G. Agarwal, R. Band, R. Bucci, S. Castells, A. Das, R. Goldouzian, M. Hildreth, K. Hurtado Anampa, T. Ivanov, C. Jessop, K. Lannon, J. Lawrence, N. Loukas, L. Lutton, J. Mariano, N. Marinelli, I. Mcalister, T. McCauley, C. Mcgrady, C. Moore, Y. Musienko[15], H. Nelson, M. Osherson, A. Piccinelli, M. Planer, R. Ruchti, A. Townsend, Y. Wan, M. Wayne, H. Yockey, M. Zarucki, L. Zygala

The Ohio State University, Columbus, Ohio, U.S.A.
A. Basnet, M. Carrigan, L.S. Durkin, C. Hill, M. Joyce, M. Nunez Ornelas, K. Wei, D.A. Wenzl, B.L. Winer, B. R. Yates

Princeton University, Princeton, New Jersey, U.S.A.
H. Bouchamaoui, K. Coldham, P. Das, G. Dezoort, P. Elmer, A. Frankenthal, B. Greenberg, N. Haubrich, K. Kennedy, G. Kopp, S. Kwan, D. Lange, A. Loeliger, D. Marlow, I. Ojalvo, J. Olsen, D. Stickland, C. Tully, L.H. Vage

University of Puerto Rico, Mayaguez, Puerto Rico, U.S.A.
S. Malik, R. Sharma

Purdue University, West Lafayette, Indiana, U.S.A.
A.S. Bakshi, S. Chandra, R. Chawla, A. Gu, L. Gutay, M. Jones, A.W. Jung, A.M. Koshy, M. Liu, G. Negro, N. Neumeister, G. Paspalaki, S. Piperov, V. Scheurer, J.F. Schulte, M. Stojanovic, J. Thieman, A. K. Virdi, F. Wang, A. Wildridge, W. Xie, Y. Yao

Purdue University Northwest, Hammond, Indiana, U.S.A.
J. Dolen, N. Parashar, A. Pathak

Rice University, Houston, Texas, U.S.A.
D. Acosta, T. Carnahan, K.M. Ecklund, P.J. Fernández Manteca, S. Freed, P. Gardner, F.J.M. Geurts, I. Krommydas, W. Li, J. Lin, O. Miguel Colin, B.P. Padley, R. Redjimi, J. Rotter, E. Yigitbasi, Y. Zhang

2024 JINST 19 P11021

University of Rochester, Rochester, New York, U.S.A.

A. Bodek, P. de Barbaro, R. Demina, J.L. Dulemba, A. Garcia-Bellido, O. Hindrichs, A. Khukhunaishvili, N. Parmar, P. Parygin[92], R. Taus

Rutgers, The State University of New Jersey, Piscataway, New Jersey, U.S.A.

B. Chiarito, J.P. Chou, S.V. Clark, D. Gadkari, Y. Gershtein, E. Halkiadakis, M. Heindl, C. Houghton, D. Jaroslawski, S. Konstantinou, I. Laflotte, A. Lath, R. Montalvo, K. Nash, J. Reichert, H. Routray, P. Saha, S. Salur, S. Schnetzer, S. Somalwar, R. Stone, S.A. Thayil, S. Thomas, J. Vora, H. Wang

University of Tennessee, Knoxville, Tennessee, U.S.A.

D. Ally, A.G. Delannoy, S. Fiorendi, S. Higginbotham, T. Holmes, A.R. Kanuganti, N. Karunarathna, L. Lee, E. Nibigira, S. Spanier

Texas A&M University, College Station, Texas, U.S.A.

D. Aebi, M. Ahmad, T. Akhter, K. Androsov[60], O. Bouhali[93], R. Eusebi, J. Gilmore, T. Huang, T. Kamon[94], H. Kim, S. Luo, R. Mueller, D. Overton, D. Rathjens, A. Safonov

Texas Tech University, Lubbock, Texas, U.S.A.

N. Akchurin, J. Damgov, N. Gogate, A. Hussain, Y. Kazhykarim, K. Lamichhane, S.W. Lee, A. Mankel, T. Peltola, I. Volobouev

Vanderbilt University, Nashville, Tennessee, U.S.A.

E. Appelt, Y. Chen, S. Greene, A. Gurrola, W. Johns, R. Kunnawalkam Elayavalli, A. Melo, F. Romeo, P. Sheldon, S. Tuo, J. Velkovska, J. Viinikainen

University of Virginia, Charlottesville, Virginia, U.S.A.

B. Cardwell, H. Chung, B. Cox, J. Hakala, R. Hirosky, A. Ledovskoy, C. Neu

Wayne State University, Detroit, Michigan, U.S.A.

S. Bhattacharya, P.E. Karchin

University of Wisconsin - Madison, Madison, Wisconsin, U.S.A.

A. Aravind, S. Banerjee, K. Black, T. Bose, E. Chavez, S. Dasu, P. Everaerts, C. Galloni, H. He, M. Herndon, A. Herve, C.K. Koraka, A. Lanaro, R. Loveless, J. Madhusudanan Sreekala, A. Mallampalli, A. Mohammadi, S. Mondal, G. Parida, L. Pétré, D. Pinna, T. Ruggles, A. Savin, V. Shang, V. Sharma, W.H. Smith, D. Teague, H.F. Tsoi, W. Vetens, A. Warden

Authors affiliated with an institute or an international laboratory covered by a cooperation agreement with CERN

S. Afanasiev, V. Alexakhin, D. Budkouski, I. Golutvin[†], I. Gorbunov, V. Karjavine, V. Korenkov, A. Lanev, A. Malakhov, V. Matveev[95], V. Palichik, V. Perelygin, M. Savina, V. Shalaev, S. Shmatov, S. Shulha, V. Smirnov, O. Teryaev, N. Voytishin, B.S. Yuldashev[96], A. Zarubin, I. Zhizhin, G. Gavrilov, V. Golovtcov, Y. Ivanov, V. Kim[95], P. Levchenko[97], V. Murzin, V. Oreshkin, D. Sosnov, V. Sulimov, L. Uvarov, A. Vorobyev[†], Yu. Andreev, A. Dermenev, S. Gninenko, N. Golubev, A. Karneyeu, D. Kirpichnikov, M. Kirsanov,

2024 JINST 19 P11021

N. Krasnikov, I. Tlisova, A. Toropin, T. Aushev, K. Ivanov, V. Gavrilov, N. Lychkovskaya, A. Nikitenko[98,99], V. Popov, A. Zhokin, M. Chadeeva[95], R. Chistov[95], S. Polikarpov[95], V. Andreev, M. Azarkin, M. Kirakosyan, A. Terkulov, E. Boos, V. Bunichev, A. Demiyanov, M. Dubinin[84], L. Dudko, A. Ershov, A. Gribushin, V. Klyukhin, O. Kodolova[99], S. Obraztsov, S. Petrushanko, V. Savrin, V. Blinov[95], T. Dimova[95], A. Kozyrev[95], O. Radchenko[95], Y. Skovpen[95], V. Kachanov, D. Konstantinov, S. Slabospitskii, A. Uzunian, A. Babaev, V. Borshch, D. Druzhkin[100]

† *Deceased*
[1] *Also at Yerevan State University, Yerevan, Armenia*
[2] *Also at TU Wien, Vienna, Austria*
[3] *Also at Ghent University, Ghent, Belgium*
[4] *Also at Universidade do Estado do Rio de Janeiro, Rio de Janeiro, Brazil*
[5] *Also at FACAMP - Faculdades de Campinas, Sao Paulo, Brazil*
[6] *Also at Universidade Estadual de Campinas, Campinas, Brazil*
[7] *Also at Federal University of Rio Grande do Sul, Porto Alegre, Brazil*
[8] *Also at University of Chinese Academy of Sciences, Beijing, China*
[9] *Also at China Center of Advanced Science and Technology, Beijing, China*
[10] *Also at University of Chinese Academy of Sciences, Beijing, China*
[11] *Also at China Spallation Neutron Source, Guangdong, China*
[12] *Now at Henan Normal University, Xinxiang, China*
[13] *Also at University of Shanghai for Science and Technology, Shanghai, China*
[14] *Now at The University of Iowa, Iowa City, Iowa, U.S.A.*
[15] *Also at an institute or an international laboratory covered by a cooperation agreement with CERN*
[16] *Also at Suez University, Suez, Egypt*
[17] *Now at British University in Egypt, Cairo, Egypt*
[18] *Also at Purdue University, West Lafayette, Indiana, U.S.A.*
[19] *Also at Université de Haute Alsace, Mulhouse, France*
[20] *Also at Istinye University, Istanbul, Turkey*
[21] *Also at Ilia State University, Tbilisi, Georgia*
[22] *Also at The University of the State of Amazonas, Manaus, Brazil*
[23] *Also at University of Hamburg, Hamburg, Germany*
[24] *Also at RWTH Aachen University, III. Physikalisches Institut A, Aachen, Germany*
[25] *Also at Bergische University Wuppertal (BUW), Wuppertal, Germany*
[26] *Also at Brandenburg University of Technology, Cottbus, Germany*
[27] *Also at Forschungszentrum Jülich, Juelich, Germany*
[28] *Also at CERN, European Organization for Nuclear Research, Geneva, Switzerland*
[29] *Also at HUN-REN ATOMKI - Institute of Nuclear Research, Debrecen, Hungary*
[30] *Now at Universitatea Babes-Bolyai - Facultatea de Fizica, Cluj-Napoca, Romania*
[31] *Also at MTA-ELTE Lendület CMS Particle and Nuclear Physics Group, Eötvös Loránd University, Budapest, Hungary*
[32] *Also at HUN-REN Wigner Research Centre for Physics, Budapest, Hungary*
[33] *Also at Physics Department, Faculty of Science, Assiut University, Assiut, Egypt*
[34] *Also at Punjab Agricultural University, Ludhiana, India*
[35] *Also at University of Visva-Bharati, Santiniketan, India*
[36] *Also at Indian Institute of Science (IISc), Bangalore, India*
[37] *Also at Amity University Uttar Pradesh, Noida, India*
[38] *Also at IIT Bhubaneswar, Bhubaneswar, India*
[39] *Also at Institute of Physics, Bhubaneswar, India*
[40] *Also at University of Hyderabad, Hyderabad, India*
[41] *Also at Deutsches Elektronen-Synchrotron, Hamburg, Germany*
[42] *Also at Isfahan University of Technology, Isfahan, Iran*
[43] *Also at Sharif University of Technology, Tehran, Iran*

2024 JINST 19 P11021

[44] *Also at Department of Physics, University of Science and Technology of Mazandaran, Behshahr, Iran*
[45] *Also at Plasma Physics Research Center, Science and Research Branch, Islamic Azad University, Tehran, Iran*
[46] *Also at Department of Physics, Faculty of Science, Arak University, ARAK, Iran*
[47] *Also at Helwan University, Cairo, Egypt*
[48] *Also at Italian National Agency for New Technologies, Energy and Sustainable Economic Development, Bologna, Italy*
[49] *Also at Centro Siciliano di Fisica Nucleare e di Struttura Della Materia, Catania, Italy*
[50] *Also at Università degli Studi Guglielmo Marconi, Roma, Italy*
[51] *Also at Scuola Superiore Meridionale, Università di Napoli 'Federico II', Napoli, Italy*
[52] *Also at Fermi National Accelerator Laboratory, Batavia, Illinois, U.S.A.*
[53] *Also at Laboratori Nazionali di Legnaro dell'INFN, Legnaro, Italy*
[54] *Also at Consiglio Nazionale delle Ricerche - Istituto Officina dei Materiali, Perugia, Italy*
[55] *Also at Department of Applied Physics, Faculty of Science and Technology, Universiti Kebangsaan Malaysia, Bangi, Malaysia*
[56] *Also at Consejo Nacional de Ciencia y Tecnología, Mexico City, Mexico*
[57] *Also at Trincomalee Campus, Eastern University, Sri Lanka, Nilaveli, Sri Lanka*
[58] *Also at Saegis Campus, Nugegoda, Sri Lanka*
[59] *Also at National and Kapodistrian University of Athens, Athens, Greece*
[60] *Also at Ecole Polytechnique Fédérale Lausanne, Lausanne, Switzerland*
[61] *Also at University of Vienna, Vienna, Austria*
[62] *Also at Universität Zürich, Zurich, Switzerland*
[63] *Also at Stefan Meyer Institute for Subatomic Physics, Vienna, Austria*
[64] *Also at Laboratoire d'Annecy-le-Vieux de Physique des Particules, IN2P3-CNRS, Annecy-le-Vieux, France*
[65] *Also at Near East University, Research Center of Experimental Health Science, Mersin, Turkey*
[66] *Also at Konya Technical University, Konya, Turkey*
[67] *Also at Izmir Bakircay University, Izmir, Turkey*
[68] *Also at Adiyaman University, Adiyaman, Turkey*
[69] *Also at Bozok Universitetesi Rektörlügü, Yozgat, Turkey*
[70] *Also at Marmara University, Istanbul, Turkey*
[71] *Also at Milli Savunma University, Istanbul, Turkey*
[72] *Also at Kafkas University, Kars, Turkey*
[73] *Now at Istanbul Okan University, Istanbul, Turkey*
[74] *Also at Hacettepe University, Ankara, Turkey*
[75] *Also at Erzincan Binali Yildirim University, Erzincan, Turkey*
[76] *Also at Istanbul University - Cerrahpasa, Faculty of Engineering, Istanbul, Turkey*
[77] *Also at Yildiz Technical University, Istanbul, Turkey*
[78] *Also at School of Physics and Astronomy, University of Southampton, Southampton, United Kingdom*
[79] *Also at IPPP Durham University, Durham, United Kingdom*
[80] *Also at Monash University, Faculty of Science, Clayton, Australia*
[81] *Also at Università di Torino, Torino, Italy*
[82] *Also at Bethel University, St. Paul, Minnesota, U.S.A.*
[83] *Also at Karamanoğlu Mehmetbey University, Karaman, Turkey*
[84] *Also at California Institute of Technology, Pasadena, California, U.S.A.*
[85] *Also at United States Naval Academy, Annapolis, Maryland, U.S.A.*
[86] *Also at Ain Shams University, Cairo, Egypt*
[87] *Also at Bingol University, Bingol, Turkey*
[88] *Also at Georgian Technical University, Tbilisi, Georgia*
[89] *Also at Sinop University, Sinop, Turkey*
[90] *Also at Erciyes University, Kayseri, Turkey*
[91] *Also at Horia Hulubei National Institute of Physics and Nuclear Engineering (IFIN-HH), Bucharest, Romania*
[92] *Now at another institute or international laboratory covered by a cooperation agreement with CERN*
[93] *Also at Texas A&M University at Qatar, Doha, Qatar*
[94] *Also at Kyungpook National University, Daegu, Korea*
[95] *Also at another institute or international laboratory covered by a cooperation agreement with CERN*

2024 JINST 19 P11021

[96] *Also at Institute of Nuclear Physics of the Uzbekistan Academy of Sciences, Tashkent, Uzbekistan*
[97] *Also at Northeastern University, Boston, Massachusetts, U.S.A.*
[98] *Also at Imperial College, London, United Kingdom*
[99] *Now at Yerevan Physics Institute, Yerevan, Armenia*
[100] *Also at Universiteit Antwerpen, Antwerpen, Belgium*

2024 JINST 19 P11021